Adsorption and Chromatographic Processes: Modeling and Optimization

by

SAI GOKUL SUBRAVETI

A thesis submitted in partial fulfillment of the requirements for the degree of

Master of Science

in

CHEMICAL ENGINEERING

Department of Chemical and Materials Engineering

University of Alberta

Abstract

High pressure carbon dioxide adsorption processes are employed in applications such as CO_2 capture and supercritical fluid chromatography (SFC). CO_2 capture using adsorption has gained wide attention because of the promising materials that are developed for this application. On the other hand, supercritical fluid chromatography is one of the most prominent techniques for chiral separations in the pharmaceutical and food industry. Supercritical fluids (such as CO_2), when compared to liquid solvents, have low viscosities and high solute diffusion coefficients. This allows for operations at high flow rates with low pressure drops (hence high productivities). The thesis addresses the design and evaluation of adsorption processes for CO_2 capture and development of modeling tools to understand the SFC processes.

The first part of the thesis deals with pre-combustion CO_2 capture using pressure swing adsorption (PSA) process in an integrated gasification combined cycle (IGCC) power plant. IGCC power plants provide favorable conditions for CO_2 capture (high operating pressures $\approx$ 35 bar and high CO_2 compositions of 30-40 %). A variety of PSA cycle configurations that were earlier designed based on a modified activated carbon, are subjected to a process optimization so as to maximize the performance of the PSA process. A multi-objective optimization framework is developed using an evolutionary algorithm with objective functions as CO_2 purity-recovery, parasitic energy and productivity of the PSA process. The study presents the formulation of an extensive model for the parasitic energy and a systematic analysis to understand the effect of low pressure and CO_2 purity. The Pareto curves obtained at the end of optimizations are examined for the process feasibility.

The second part of the thesis focuses on developing a comprehensive axi-symmetric computational fluid dynamics (CFD) model in order to understand the dynamics of a plug introduced through a mixed-stream injection in supercritical fluid chromatographic columns. Two main phenomena contribute to chromatographic band distortions: the different retention behaviors of solute in the plug and in the mobile phases; and viscous fingering, a phenomenon where less

viscous mobile phase penetrates into more viscous plug. The aim of this study is to confirm the existence of viscous fingering and explain the peak distortions arising due to large-volume injections in SFC columns. The model takes into account of key phenomena that influence peak shapes in SFC, namely, the injection of fluids with different viscosities, variation of solute retention with local mobile phase composition and pressure. Finally, the simulated elution peaks of solute are compared against the experiments.

Keywords: Adsorption, Carbon dioxide capture, Supercritical fluid chromatography, Pressure swing adsorption, Pre-combustion, Optimization, Computational fluid dynamics, Viscous fingering, Porous media.

To my parents

Acknowledgements

First and foremost, I would like to express my gratitude to Prof. Arvind Rajendran for accepting me as a master student in his group. The unconditional support and guidance he gave over the years were indispensable and are tremendously appreciated. His expertise, meticulousness and eye for detail make him an exceptional researcher and a source of inspiration. The discussions during the individual and group meetings have helped me broaden my knowledge. I have thoroughly enjoyed working under his supervision. Thank you Arvind.

I am sincerely grateful to Prof. Petr Nikrityuk for his support and guidance on CFD modeling that has greatly influenced the second part of my thesis. His expertise and readiness to help were essential for the success of this work. Thank you Dr. Nikrityuk.

Special thanks to my former and current colleagues, Ali, Ashwin, Libardo, Nagesh, Nick, Parinaz, Tai and Vishal for making my life at University of Alberta enjoyable. I appreciate your support and collaboration over the last two years. Our everyday lunch discussions were super fun and I learnt a lot about different cultures. Ashwin, thanks for making my transition to Edmonton smoother and also for being a "kind" mentor.

I am thankful to Dr. Venu Vinod, who has been a great teacher, mentor and made chemical engineering interesting during my undergraduate years. Special thanks to Dr. Sunil Kumar and Dr. P.V. Suresh for their support and guidance. I am grateful to Dr. Sreenivas Jayanti for giving me an opportunity to work under his supervision at IIT Madras.

I acknowledge the funding from National Sciences and Engineering Research Council of Canada, National Energy Technology Laboratory, United States Department of Energy Office of Fossil Energy and University of Alberta. I would also like to thank Dr. Ambalavanan Jayaraman and TDA Research Inc. for the fruitful discussions we had throughout the project.

Rohit, Vamsi, Srinath, Teja, Ravi and Raginee were wonderful friends at NIT Warangal. The endless discussions with Rohit and Ravi about chemical engineering, life and movies were memorable. Thank you Vamsi for being supportive all these years.

Rahul, Sanat, Geetesh and Sumanth have been a wonderful roommates and made my stay in Edmonton enjoyable.

Bhargav and Meher have been my best friends. Dheeraj, Prashanth, Vijay, Rajesh and Rakesh have provided a great support over the years. The days we spent together in Hyderabad were the most cherished ones.

Finally, I thank my parents for all the support, encouragement and trust. None of this would be possible without their love and kindness. My brother Nikhil always gave me an unwavering support and confidence to accomplish my goals.

Sai Gokul SUBRAVETI
Edmonton 2017

Contents

List of Figures

List of Tables

List of Symbols

Roman symbols

A	Area of cross-section [m^2]
b	Adsorption equilibrium constant [Pa^{-1}]
C	Gas phase concentration [mol m^{-3}]
c	Mass fraction [-]
C_2	Inertial coefficient in porous media [m]
c_m	Methanol mass fraction [-]
C_p	Specific heat capacity [J kg^{-1} K^{-1}]
d_p	Particle diameter [m]
D	Overall solvent dispersion constant [m^2 s^{-1}]
D_L	Axial dispersion constant [m^2 s^{-1}]
D_s	Overall solute dispersion constant [m^2 s^{-1}]
E	Electrical power [kW_e]
En	Total electrical power consumption [kWh_e $tonne^{-1}$]
f	Flux
H	Henry constant of solute i [-]
h	Heat transfer coefficient [J m^{-2} K^{-1} s^{-1}]
h_g	Specific enthalpy of steam [kJ kg^{-1}]
J	Objective function
k	Adsorption equilibrium constant in Sips isotherm [Pa^{-1}]
K	Adsorption equilibrium constant in Freundlich isotherm [mol kg^{-1} $Pa^{-\frac{1}{n}}$]
K_w	Effective wall thermal conductivity [J m^{-1} K^{-1} s^{-1}]
K_z	Effective gas thermal conductivity [J m^{-1} K^{-1} s^{-1}]
$\bar{k}$	Mass transfer coefficient [s^{-1}]
$\bar{K}$	Permeability in porous media [m^2]
L	Column length [m]
m	Mass flow rate [kg s^{-1}]
N	Number of stages
n	Molar flow rate [kmol s^{-1}]
P	Absolute pressure [Pa]
p	Partial pressure [Pa]
P^0	Equilibrium gas-phase spreading pressure
Pu	Purity [%]
Pr	Productivity [mol m^{-3} s^{-1}]
Q	Volumetric flow rate [m^3]
q	Solid phase concentration [mol m^{-3}]
$\bar{q}$	Dimensionless solute solid phase concentration [-]

R	Universal gas constant [Pa m^3 mol^{-1} K^{-1}]
r	Solution smoothness
$\bar{r}$	Compression ratio [-]
Re	Recovery [%]
s	Heterogeneity parameter in Sips isotherm [-]
t	Time [s]
T	Temperature [K]
V	Volume
v	Interstitial velocity [m s^{-1}]
v_s	Superficial velocity [m s^{-1}]
v_{adj}	Adjusted velocity [m s^{-1}]
W	Work done [kJ s^{-1}]
x	Solid phase mole fraction [-]
y	Fluid phase mole fraction [-]
z	Axial coordinate [m]
r	Radius of column [m]
Q	Heat [J]

Greek symbols

α_p	Rate of pressurization or depressurization [s^{-1}]
ΔH	Heat of adsorption [J mol^{-1}]
ΔP_{exp}	Difference between outlet and inlet pressures in experiments [Pa]
ϵ_B	Bed porosity [-]
ε	Mass balance error
η	Efficiency [%]
γ	Adiabatic constant [-]
Γ	Isotropic diffusivity [kg m^{-1} s^{-1}]
λ	Latent heat [kJ kg^{-1}]
μ	Viscosity [kg m^{-1} s^{-1}]
ϕ	Flux limiter function
π	Spreading pressure
ψ	Electrical power consumption per tonne of CO_2 captured [kWhe $tonne^{-1}$]
ρ	Density [kg m^{-3}]
τ	Stress tensor [kg m^{-1} s^{-2}]

Abbreviations, subscripts and superscripts

$*$	Equilibrium state
adia	Adiabatic
adj	Adjusted
ADS	Adsorption
B	Bed
c	Critical state
CC	CO_2 compression
CoBLO	Co-current blowdown
CnBLO	Counter-current blowdown

DES	Desorption
e	Electrical
F	Feed
H	High
i	Index of species
in	Inner
inj	Injection
INT	Intermediate
L	Low
m	Methanol
mix	Mixture
o	Overall
out	Outer
P	Particle
PEQ	Pressure equalization
PUR	Purge
ref	Reference
s	Solute
sat	Saturation
SP	Steam consumption
T	Total
w	Wall

Acronyms

CCS	Carbon capture and storage
CV	Control volume
CFD	Computational fluid dynamics
CFL	Courant-Friedrichs-Lewy condition
CSS	Cyclic steady state
DV	Decision variable
ED	Equilibrium-Dispersive
FVM	Finite volume method
GA	Genetic Algorithm
HPLC	High performance liquid chromatography
IAS	Ideal adsorbed solution
IGCC	Integrated gasification combined cycle
LDF	Linear driving force
LHS	Latin Hypercube sampling
LPP	Light product pressurization
MUSCL	Monotonic Upstream-Centered Scheme for Conservation Laws
MOF	Metal organic framework
ODE	Ordinary differential equation
PDE	Partial differential equation
PE	Pressure equalization
PSA	Pressure-swing Adsorption
SFC	Supercritical fluid chromatography
SIMPLE	Semi-Implicit Method for Pressure-Linked Equations

TSA	Temperature-swing Adsorption
TTBB	Tri-tert-butylbenzene
TVD	Total variation diminishing
UDF	User-defined Function

Chapter 1

Thesis outline

1.1 Objectives and structure of the thesis

The goals of the thesis is to study the high pressure CO_2 adsorption processes for two different applications, viz., pre-combustion CO_2 capture and supercritical fluid chromatography (SFC). The thesis is structured into two parts. The primary objective of the first part of the thesis is to evaluate the different pressure swing adsorption processes using a full-scale process optimization. The second part of the thesis focuses on providing a better understanding of SFC processes through a computational fluid dynamics approach.

The key aspects followed to achieve the main objectives are:

- A rigorous and efficient model was implemented to simulate pressure swing adsorption processes.
- A detailed parasitic energy model for PSA process was developed that provides an understanding on the energy penalty imposed on pre-combustion CO_2 capture.
- Two sets of multi-objective optimization studies were performed, first to determine the optimal operating conditions that would meet CO_2 sequestration targets and second to minimize the energy consumption and maximize the productivity of the process while meeting the sequestration targets.
- A comprehensive axi-symmetric CFD model was developed, to provide a proper description of plug propagations in SFC processes, and compared with the experiments.

Chapter 2 introduces the different types of technological options available for CO_2 capture and basic concepts of adsorption processes and adsorbents. Chapter 3 presents the modeling and optimization of a PSA cycle. The empirical model describing the single and competitive adsorption equilibria is discussed. A detailed PSA model that takes into account mass, momentum and energy balances is described and validated. A solution methodology of the process optimization based on genetic algorithm, which would be the core of Chapter 4, is shown.

Chapter 4 focuses on evaluating different PSA cycle configurations using full-scale optimizations. The adsorption equilibria for CO_2 on TDA AMS-19 is fitted to the empirical model. Two sets of optimization studies are conducted, first, an unconstraint multi-objective optimization to maximize the CO_2 purity and recovery so as to obtain the optimal operating conditions that would meet sequestration targets. A detailed parasitic energy model is developed taking into account CO_2 compression and steam consumption. Parametric studies are performed to learn the effect of low pressure on the energy consumption. Second multi-objective optimization is conducted under the constraints of purity-recovery to minimize the parasitic energy and maximize the productivity of the cycles that satisfied sequestration targets.

Chapter 5 deals with the development of an axi-symmetric CFD model to confirm viscous fingering in SFC columns. The commercial CFD solver ANSYS Fluent 16.2 is employed for solving mass, momentum and transport equations. Special source terms are implemented using user-defined functions. The simulations are compared with the experimental results.

Chapter 6 provides the conclusions of this work as well as the recommendations for future studies.

Chapter A provides a supporting information on the results obtained by performing different CFD simulations to study the effect of dispersion constant on predicting viscous fingering phenomenon.

Part I

Pre-combustion CO_2 capture

Chapter 2

Introduction to Pre-combustion CO_2 capture

The purpose of this chapter is to introduce the reader to the topics of climate change mitigation, CO_2 capture and storage, to present an overview of technological options available for capture and to the basic concepts of adsorption processes and adsorbents.

2.1 General Introduction

Recently, there has been a significant rise in global CO_2 concentration levels [1]. Fig. 2.1(a) shows the increasing global CO_2 concentrations in the atmosphere for the last 57 years. Consequently, the global surface temperatures have increased (as shown in Fig. 2.1(b)). Climate change is a major challenge and mitigating it is utmost important. Anthropogenic CO_2 emissions from the energy and power sectors account for about 69% and are the largest sources of global CO_2 emissions [2]. The international commitment to limit the temperature rise to below 2 °C can be achieved by mitigating the current CO_2 emissions.

CO_2 capture and storage (CCS) is a feasible solution that is readily available to reduce the CO_2 emissions. CCS involves capturing CO_2 emitted from the combustion of fuels in power generation. The CO_2 is then transported to a storage site, where it is stored away from atmosphere for a long period of time [3]. Currently, there are 38 large-scale CCS projects around the world either in operation or under development [4]. SaskPower's Boundary Dam CCS project in Saskatchewan, Canada was the world's first operational large-scale CCS project in power sector. In this chapter, the technological options available for CO_2 capture will be discussed.

2.2 Carbon capture in coal fired power plants

Power and industry sectors are the largest sources of global CO_2 emissions [3]. Coal-fired power plants are predominantly used for generating electricity. Most of the CO_2 is emitted when the fuel (coal) is burnt. To combat global warming, it is important to avert the CO_2 emissions from

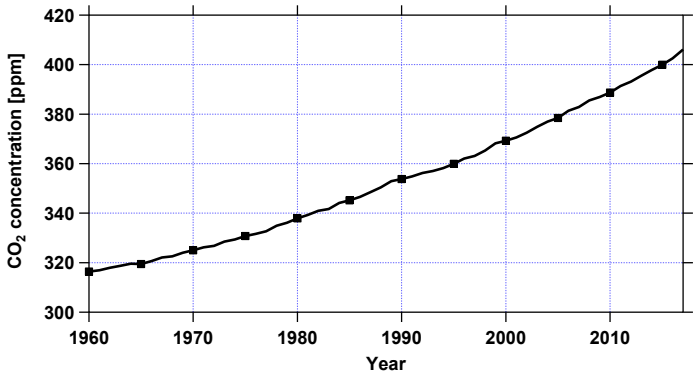

(a)

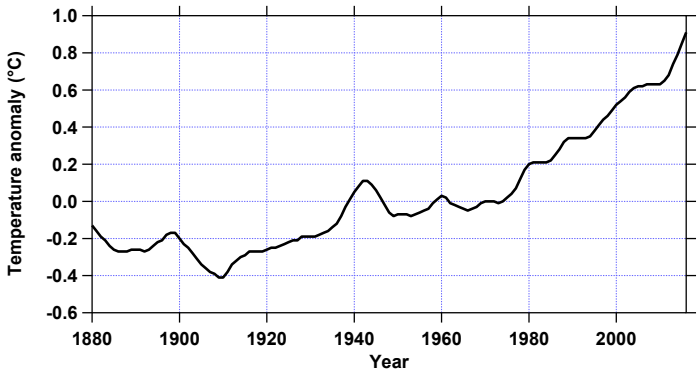

(b)

Figure 2.1: (a) Increasing global CO_2 concentrations in the atmosphere over last 57 years (b) Global surface temperature relative to 1951-1980 average temperatures. Source: NASA and National Oceanic and Atmospheric Administration [5, 6].

these coal-fired power plants. The concept of CO_2 capture is to produce a concentrated stream of CO_2 that can be transported to the CO_2 storage site and sequestered permanently. There are three technological options available for capturing CO_2 from coal-based power plants [2] [3]. The schematic of these three approaches is shown in Fig. 2.2. First technology, *Post-combustion CO_2 capture* separates CO_2 from the flue gas stream produced by combustion of coal in air. The flue gas is passed through the CO_2 capture unit after combustion, instead of directly discharged into atmosphere. For a post-combustion scenario, the CO_2 present in flue gas stream is about 12% to 15% by mole [2]. The capture occurs at atmospheric conditions. The second type of technology available is the *oxy-fuel combustion process*, which involves the separation of nitrogen from air in an air separation unit, followed by combustion of coal in pure oxygen environment. If fuel is combusted in pure oxygen, the flame temperature rises excessively and this can be controlled by recycling the part of flue gas to the combustor. The flue gas stream has a CO_2 concentrations of 70-85% [2]. In oxy-fuel process, with the flue gas mainly comprising of H_2O and CO_2, makes the capture easy. For a *pre-combustion system*, the fuel is first combusted in

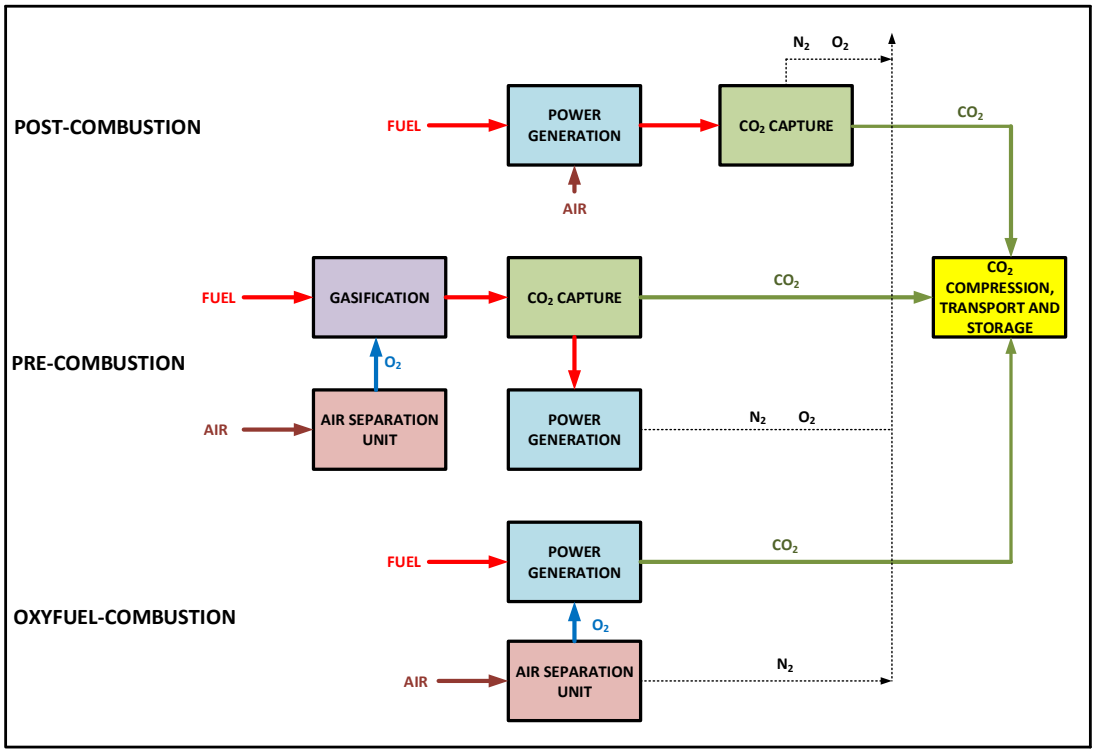

Figure 2.2: Different types of CO_2 capture technologies. Adapted from [3].

oxygen and/or steam, followed by a shift-gas reaction to produce syngas which is a mixture of H_2 and CO_2. The CO_2 in syngas is separated and then fuel H_2 stream is used to generate electricity. The composition of syngas is about 40% CO_2 and 60% H_2. Post-combustion capture is a matured technology where CO_2 is captured already on commercial scale. Oxy-fuel combustion and Pre-combustion capture technologies are still in demonstration stages in pilot plants.

There are other technologies that are being developed for CO_2 capture. One such technology is *Chemical looping combustion (CLC)*. This concept is considered as a variant of oxy-fuel combustion process. In oxy-fuel combustion, the oxygen has to be separated from air before combustion. However, in CLC the oxygen is utilized internally and eliminates the large capital and energy consumption for oxygen separation from air in oxy-fuel combustion process. CLC uses the oxygen in a metal oxide to complete combustion. The typical CLC configuration involves two interconnected fluidized bed reactors, namely, air and fuel rectors [7]. The metal oxide which is an oxygen carrier is circulated between the air and fuel reactors. In fuel reactor, the gaseous fuel is oxidized through oxygen in metal oxide, producing CO_2 and water vapor. The CO_2 can be recovered easily from water vapor by condensation. Once the metal oxide is reduced to metal after oxidization, the metal is circulated to air reactor where the metal reacts with air to form a metal oxide. This technology has the potential for capturing CO_2 with low energy requirements [7]. This concept is currently under demonstration in pilot plants [2].

One of the main separation methods that is currently in use for CO_2 capture is absorption. In absorption, the separation is achieved by contacting the CO_2 containing gas stream with a liquid solvent. The interactions between the CO_2 and liquid solvent can either be physical or chemical. In chemical absorption, the CO_2 is absorbed by forming a strong chemical bond between the solvent and CO_2. The chemical absorption is currently employed for post-combustion systems. The most commonly used chemical solvents are monoethanolamine (MEA), tertiary amine methyldiethanolamine (MDEA). While in physical absorption, a weaker interaction between CO_2 and solvent is the driving force for separation. This method is suitable for separations at high pressures where the bonding takes place at high pressures. The suitable application of this method will be the pre-combustion system because of high pressure and high concentrations of CO_2 in the feed. The physical solvents currently being used are selexol, rectisol etc. However, the cons of using chemical solvents for capture include high energy penalty for solvent regeneration, corrosion and degradation of solvent [8–10]. The physical solvents can decrease the energy for regeneration and achieve a higher solubility at high pressures [11, 12]. The issue with physical solvents is they perform better at low temperatures [13]. The other alternative separation technology that has the potential to capture CO_2 is adsorption. Adsorption based processes use solid sorbents to capture CO_2. Adsorption-based separations are primarily employed in air separation and hydrogen purification [14, 15]. The adsorption process involves two stages, an adsorption stage where the CO_2 loads onto the sorbent, while in the desorption stage, the sorbent is regenerated. There are several sorbents that are synthesized for CO_2 capture applications. The adsorption-based separation involves separating species based on the difference in their affinities towards the sorbent. The adsorption-based processes have shown potential and are currently being developed. There are other separation techniques that are being explored like membrane-based separation [16].

With the recent developments in sorbent synthesis for adsorption based CO_2 capture, a portion of this thesis is devoted to evaluate the potential of adsorption-based techniques on a process scale that would achieve CO_2 capture meeting desired requirements.

2.3 Pre-combustion CO_2 capture in an IGCC power plant

The reference power plant for pre-combustion CO_2 capture is an Integrated Gasification Combined Cycle (IGCC) power plant. In an IGCC power plant, the coal is burnt in a gasifier to produce syngas. The syngas later goes into a combined cycle to produce electricity. A CO_2 capture unit is integrated to an IGCC power plant. Fig. 2.3 shows the block diagram of an IGCC power plant with CO_2 capture unit. It is important to understand the IGCC power plant so as to integrate the capture unit.

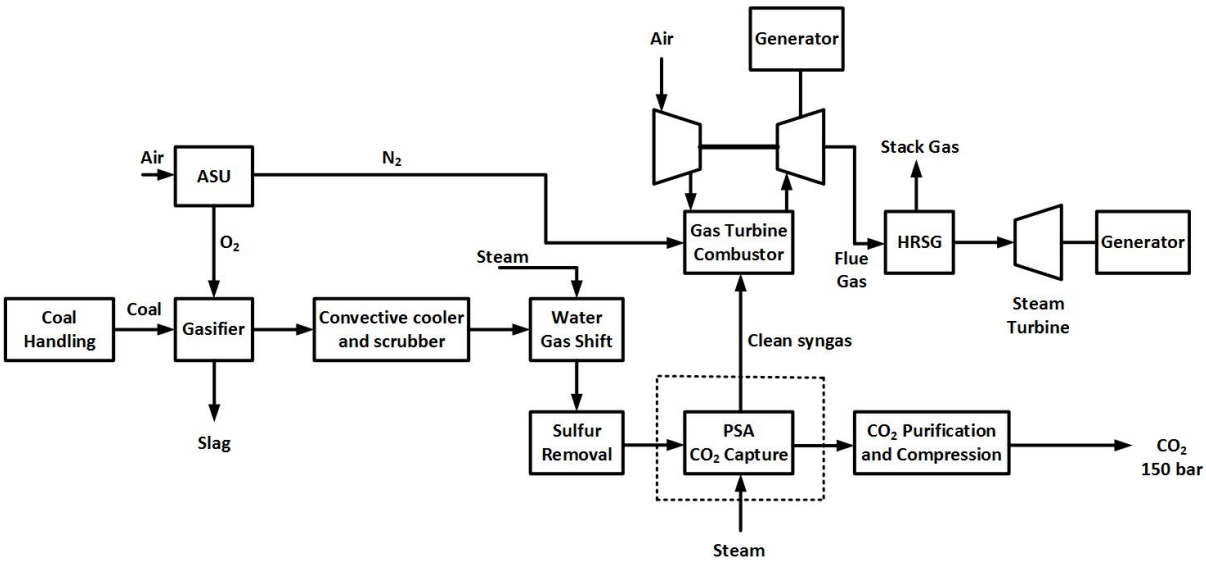

Figure 2.3: Schematic of an IGCC power plant. Dotted box represents the scope of current work in collaboration with TDA Research Inc.

Process description of an IGCC power plant

The feed to an IGCC power plant is coal (eg. bituminous coal). The coal is supplied to the gasifier where a partial oxidation occurs to produce CO and H_2O (syngas). Pure-oxygen is required for the oxidation reaction in the gasifier. Hence, an IGCC power plant incorporates an air separation unit (ASU). The operating conditions for gasifier include maintaining pressures of 20-50 bar and a temperature more than 1500°C. At such high temperatures, the ash generated in the combustion reaction converts to liquid slag and flows out of the gasifier easily [17]. The hot syngas with sensible heat is cooled down to $\approx$ 300 °C and the heat recovered will be used to produce steam that can be integrated to any system in the power plant. The syngas then undergoes a clean up where particulates are removed. The syngas comprising of species with high partial pressures and low volume flow rate ease the clean up process. A shift reaction occurs in a shift reactor where the CO is converted to CO_2 and all the heating value of CO is transferred to H_2. The flue stream from shift reactor is sent for desulfurization, after which the stream is ready for CO_2 capture.

At this point, an absorber or adsorption unit can be integrated to the power plant where CO_2 is separated from H_2. The H_2 stream is then fed to the gas turbine to produce electricity. A nitrogen stream from an air separation unit is fed to the gas turbine. The nitrogen stream serves two purposes. First, it controls the NO_x emissions in the combustion and also augments the power generation. Second, when compared to other fuels, H_2 stream fed to gas turbine has low mass flow rate and nitrogen stream added ensures the desired mass flow rate to maintain the turbine temperature. The flue gas stream exits the gas turbine at 600 °C. Hence, an additional heat recovery system is used to generate steam. The steam produced in the heat recovery steam

generator (HRSG) is fed to a steam turbine to produce additional electricity. The CO_2 captured in the power plant is compressed to supercritical conditions so as to inject it into storage site.

2.4 Adsorption-based capture

Adsorption is considered as the potential separation technique for CO_2 capture [18]. Adsorption based separations involve two processes: adsorption and desorption. In adsorption, gas molecules (adsorbate) adsorb onto the solid surface (adsorbent). A desorption is a regeneration process where adsorbate molecules are removed from the surface of adsorbent. The component gases in a gaseous mixture have different affinities towards the adsorbent. The component is said to be strongly adsorbing if it has high affinity (strong van der Waal's forces) towards adsorbent when compared to other components. Most of the materials considered for CO_2 capture applications have strong affinities towards CO_2. For any cost-effective separation process, low equipment sizing and high separation efficiency is desired. For an adsorption-based separation, the size of adsorption vessels is determined by the amount of adsorbent required for separation. The working capacity (Δq) dictates the amount of adsorbent needed for separation. Δq is defined as the difference in the solid phase loadings on an adsorption equilibria isotherm at adsorption and desorption conditions respectively. High working capacity reduces the adsorbent quantity and process equipment size [18]. In order to achieve high separation efficiencies, the adsorbent is desired to have high selectivity towards CO_2. A selectivity is defined as the ratio of the CO_2 capacity to that of other component (N_2 or H_2). High selectivity for CO_2 has a direct impact on the purity of CO_2 captured.

CO_2 separation using adsorbents is done either through pressure swing adsorption process (PSA) or temperature swing process (TSA). Fig. 2.4 describes the concept involved in the pressure and temperature swing processes using an adsorption equilibria isotherm. In a PSA based process, the strongly adsorbed component CO_2 is adsorbed at a high pressure P_{ADS} because the adsorbent has a high capacity at high pressures, as shown in Fig. 2.4. Since the weakly adsorbed component (N_2 or H_2) has weak affinity towards the adsorbent, it is removed from the column. In order to regenerate the column, a desorption is performed by utilizing a pressure swing. Since the adsorbent has low capacity for CO_2 at low pressure P_{DES}, the pressure in the column is reduced to P_{DES} to let the CO_2 out and regenerate the column. In a TSA based process, a difference in capacities at different temperatures is utilized to perform adsorption and desorption stages. The CO_2 is captured at low temperature T_{ADS} since the adsorbent has high capacity for CO_2 at low temperatures. The column is regenerated by performing desorption at a high temperature T_{DES}.

The adsorption phenomenon is based on the affinity of adsorbate molecules to an adsorbent surface. The interactions between adsorbate and adsorbent are due to van der Waal's forces which consist of molecular forces such as permanent dipole, induced dipole and quadrupole electrostatic interactions [14]. The adsorbate-adsorbent interactions depend on the type of adsorbate

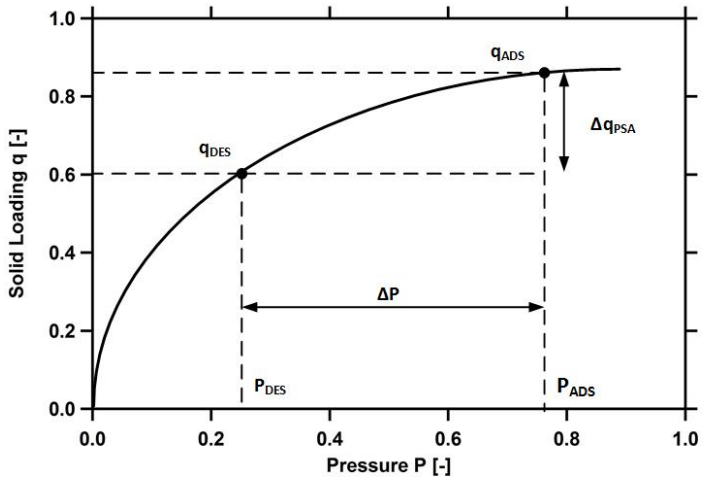

(a) Pressure Swing Adsorption

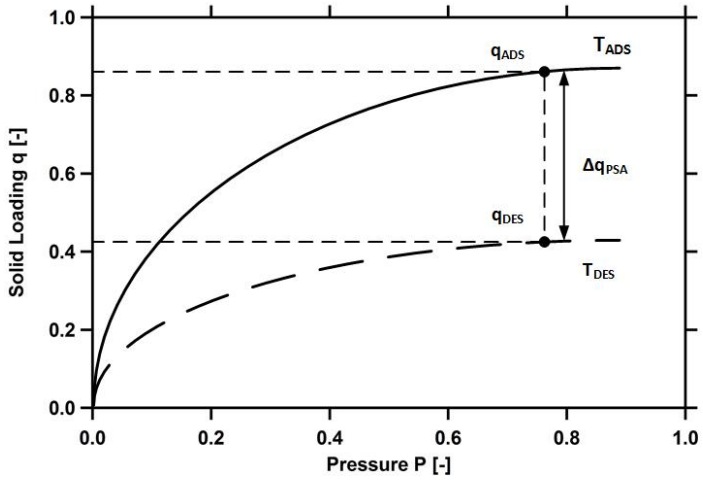

(b) Temperature Swing Adsorption

Figure 2.4: Concept of (a) Pressure Swing Adsorption (b) Temperature Swing Adsorption.

molecules and adsorbent surface selected. When the separation is driven by the difference in these interactions, thermodynamics is rate controlling for mass transfer operation. In some cases, the separations can be due to difference in adsorption rates (kinetic selectivity). When there exists a significant difference in the adsorption/desorption rates for different components, kinetics is rate controlling.

The key advantage of a PSA process over TSA process is that the PSA process involves rapid change of pressures, resulting in shorter cycle-times and high productivities, while the TSA process has slow change in temperatures, resulting in longer cycle times and low productivities. In this work, the PSA process is evaluated for pre-combustion capture technology.

2.5 Adsorbents

The selection of adsorbent is important for an adsorption based CO_2 separation. Based on the type of capture, i.e. post-combustion or pre-combustion, material selection is done. The adsorbents have to be economical and operational for CO_2 capture [18]. The criteria while selecting the adsorbent involve high adsorption capacity for CO_2 , high CO_2 selectivity, fast adsorption kinetics, mechanical strength and stability [19, 20]. There are various materials that have been developed for CO_2 capture applications [21]. These materials include classical zeolites, activated carbons, metal-organic frameworks, metal-oxide based materials etc. In this section, an overview of these materials is presented.

2.5.1 Zeolites

Zeolites are porous crystalline aluminosilicates comprising of SiO_4 and AlO_2 units joined together. These are microporous materials with uniform pore sizes. Zeolites are extensively studied because of their ability to separate CO_2 based on molecular sieving effect and also the strong dipole-quadrupole interactions between CO_2 and alkali-metal cations [22]. Among the different types of zeolites that are studied for CO_2 capture, Zeolite 13X, has shown better performance than any other zeolites [23] for post-combustion CO_2 capture. The performance of zeolites is greatly influenced by the temperature and pressure [18, 24]. The presence of moisture showed a reduction of adsorption capacity of Zeolite 13X, therefore requiring very high regeneration temperatures [25]. These disadvantages limit the use of Zeolite 13X for wet stream flue gas separations.

2.5.2 Metal-organic frameworks

Metal-organic frameworks (MOF's) are a new class of microporous crystalline solids which consists of a network of metal ions and organic ligands. These type of materials can be synthesized using enormous combinations of different metals and different organic ligands. MOF's are used in many applications owing to their unique structural properties; thermal and chemical stabilities and high internal surface areas [21]. There is an active research going on in developing MOFs for CO_2 capture applications. Yaghi et al. synthesized MOF-210 which has very high CO_2 uptake [26]. Although MOFs have very high capacities at high pressures, their capacities were found lower than other adsorbents at atmospheric conditions. MOFs suffer from durability and mechanical strength problems when CO_2 capture occurs in the presence of moisture [24].

2.5.3 Activated carbons

Activated carbons are widely employed for gas purification, water treatment etc. because of low cost and wide availability [14]. In activated carbons, the pore size distribution varies from micropore to macropore. Studies showed that the heat of adsorption of activated carbon is lower than zeolites because of its weaker interactions with CO_2, thereby requiring lower regeneration

energies [27]. Activated carbons allow fast adsorption kinetics and are hydrophobic in nature. Activated carbons suffer from low selectivities because of their wide range of pore distribution. The equilibrium measurements at low pressures showed low CO_2 uptakes, while at high pressures, the CO_2 adsorption capacities are higher than zeolites. Hence, these are attractive for pre-combustion CO_2 capture.

Since the activated carbons showed very high CO_2 adsorption capacities at high pressures and can be operated over a wide range of pressures, an adsorption based pre-combustion CO_2 capture process is studied in this work using a novel adsorbent, TDA AMS-19, a surface modified activated carbon, which was developed by TDA Research Inc.

Chapter 3

Modeling and process optimization of a pressure swing adsorption (PSA) cycle

3.1 Introduction

Process design of a pressure swing adsorption (PSA) cycle involves two stages: First, a detailed modeling using numerical techniques, so as to predict the dynamics of a PSA process. Second, a rigorous optimization, to maximize the performance. The numerical methods are required to be robust to solve the coupled pressure, mass and energy transport equations and also to tackle the complexities involved while solving shock and wave propagation associated with the PSA process. An optimization framework is developed to increase the performance of a PSA process. In this chapter, the mathematical description of adsorption equilibria, detailed PSA model and optimization framework are discussed.

3.2 Modeling of adsorption equilibria for a PSA process

The description of adsorption equilibria is a key aspect in the design of a PSA process. A comprehensive knowledge of adsorption equilibrium over a range of pressures and temperatures helps in understanding the dynamics of component gases that are to be separated. Modeling of adsorption equilibria involves fitting an isotherm model to experimental measurements. A typical PSA process involves more than one component gas. In this section, single component and competitive adsorption isotherm models are presented.

3.2.1 Adsorption isotherm model

Single component adsorption equilibria

There are several isotherm models available in literature [14, 28]. Although, Langmuir isotherm model [29] is a standard model that describes type 1 isotherms, it has shortcomings while predicting the mixture equilibria and accounts for no heterogeneity [14].

The Langmuir isotherm is written as

$$q_{\mathrm{i}}^{*} = \frac{q_{\mathrm{sat,i}} b_{\mathrm{i}} p_{\mathrm{i}}}{1 + b_{\mathrm{i}} p_{\mathrm{i}}} \tag{3.1}$$

where q_{i}^{*} is the equilibrium solid phase loading at a given temperature and pressure. $q_{\mathrm{sat,i}}$ is the saturation solid phase loading and b_{i} is the adsorption equilibrium constant for component i. b_{i} is the temperature dependent constant and is described by Arrhenius type temperature dependence.

$$b_{\mathrm{i}} = b_0 e^{-\frac{\Delta H_{\mathrm{i}}}{RT}} \tag{3.2}$$

where ΔH_{i} is the heat of adsorption.

After Langmuir isotherm, Freundlich isotherm model is most commonly used [28]. Fruendlich isotherm, an empirical equation, accounts for heterogeneity on the adsorbent surface. The model assumes that the sites with same adsorption energy form a patch; different patches form a surface. There is no interaction between different patches. It also assumes that on each patch, adsorbate molecule adsorbs onto only one adsorption site. Hence, local adsorption equilibria on each patch can be described using Langmuir model. The Freundlich isotherm takes the form

$$q_{\mathrm{i}}^{*} = K p^{\frac{1}{n}} \tag{3.3}$$

where K and n are temperature dependent parameters. The isotherm equation reduces to a linear isotherm when n=1. As the parameter n is increased, the isotherm becomes more non-linear, thus n defines the isotherm sharpness. For most of the practical systems the parameter n is greater than 1 [28].

From the definition of Freundlich isotherm, the equilibrium loading q_{i}^{*} increases with increase in pressure. This means the solid has infinite capacity. However, at higher physical pressures, the solid loading reaches a saturation. This drawback of Freundlich isotherm led to developing the Sips isotherm [30]. Sips proposed an equation that is similar to Fruendlich equation but reaches a saturation in equilibrium solid loading at high pressures. The modified equation is known as Sips isotherm or Langmiur-Freundlich isotherm. The Sips isotherm is represented as

$$q_{\mathrm{i}}^{*} = \frac{q_{\mathrm{sat,i}} \left(k_{\mathrm{i}} p_{\mathrm{i}}\right)^{s_{\mathrm{i}}}}{1 + \left(k_{\mathrm{i}} p_{\mathrm{i}}\right)^{s_{\mathrm{i}}}} \tag{3.4}$$

$$q_{\mathrm{sat,i}} = \omega_{\mathrm{i}} e^{-\frac{\psi_{\mathrm{i}}}{RT}} \tag{3.5}$$

$$k_{\mathrm{i}} = \theta_{\mathrm{i}} e^{-\frac{\phi_{\mathrm{i}}}{RT}} \tag{3.6}$$

$$s_{\mathrm{i}} = s_{1,\mathrm{i}} \arctan(s_{2,\mathrm{i}}(T - T_{\mathrm{ref}})) + s_{\mathrm{ref,i}} \tag{3.7}$$

q_{i} is the temperature dependent saturation solid phase concentration; k_{i} is the adsorption equilibrium constant; s_{i} is a parameter describing the homogeneity of the surface; s_{i} takes the values between 0 and 1. As s_{i} approaches unity, Sips isotherm becomes simple Langmuir isotherm model.

Competitive adsorption equilibria

Understanding the competition among the component gases is important while designing the PSA process. The competition can either be determined experimentally using the multicomponent mixtures or by using ideal adsorbed solution theory or extending isotherm models [31–33].

Ideal Adsorbed Solution Theory

The ideal adsorbed solution (IAS) theory is based on solution thermodynamics to describe the solid-liquid equilibria [31]. IAS theory is equivalent to Raoult's law for vapor-liquid equilibrium. The main assumptions of IAS theory are:

- Adsorbate molecules have identical saturation capacities
- The adsorbent surface is homogeneous
- Adsorbed phase is ideal

For an n component mixture, the IAS theory is given by

$$Py_{\mathrm{i}} = P_{\mathrm{i}}^{0}(\pi)x_{\mathrm{i}} \ [n \text{ equations}] \tag{3.8}$$

Py_{i} is the partial pressure of component i
P_{i}^{0} is the equivalent of a vapor pressure. It is the pressure at which the pure component is at the same spreading pressure and temperature as that of the mixture
π_{i} is the spreading pressure
x_{i} is the mole fraction of component i

The mole fraction of component i is given by,

$$x_{\mathrm{i}} = \frac{q_{\mathrm{i}}^{*}}{\sum_{i=1}^{n_{\mathrm{comp}}} q_{\mathrm{i}}^{*}} \tag{3.9}$$

The spreading pressure π_{i} is defined as,

$$\frac{\pi_{\mathrm{i}} A}{RT} = \int_{0}^{P_{\mathrm{i}}^{0}} \frac{q_{\mathrm{i}}^{*,0}}{P} dP \tag{3.10}$$

$q_{\mathrm{i}}^{*,0}$ is the pure component equilibrium adsorption capacity, A is the area of solid

At equilibrium, the spreading pressures are the same for n components,

$$\pi_1 = \pi_2 = ... = \pi_n \tag{3.11}$$

The total amount adsorbed is calculated using

$$\frac{1}{n_{\mathrm{Tot}}} = \sum_{i=1}^{n} \frac{x_{\mathrm{i}}}{q_{\mathrm{i}}^{*,0}} \tag{3.12}$$

$$\sum_{i=1}^{n} x_{\mathrm{i}} = 1 \tag{3.13}$$

The competition among the component gases can be estimated by solving equations 3.8 to 3.13 simultaneously. These equations account for $2n+1$ independent equations and $2n+1$ variables ($P^0_{\mathrm{i=1,...N}}$, $x_{\mathrm{i=1,..N}}$ and n_{Tot}). These equations cannot be solved analytically for the most of the pure component isotherm models, therefore, iterative methods are to be employed. The determination of competition using IAS theory is not straightforward and hence, very often extended isotherm model equations are used.

Extended isotherm models

Extended isotherm models describe the multicomponent adsorption by adding an extra term in the denominator of pure component isotherm models. The extra term decreases the solid phase concentration due to the competition among n components in the system. Though extended model does not capture the competition accurately, it is less intensive to model. In this work, the multicomponent adsorption is described by extending the single component isotherm model. The extended Sips isotherm model can be written as

$$q_{\mathrm{i}}^{*} = \frac{q_{\mathrm{sat,i}} \left(k_{\mathrm{i}} p_{\mathrm{i}}\right)^{s_{\mathrm{i}}}}{1 + \sum\limits_{i=1}^{n_{\mathrm{comp}}} \left(k_{\mathrm{i}} p_{\mathrm{i}}\right)^{s_{\mathrm{i}}}} \tag{3.14}$$

3.3 PSA model

3.3.1 Model equations

In order to develop the model equations for the process, packed bed column of length L, filled with a solid adsorbent is considered. The adsorption dynamics is described using a one-dimensional model. The model assumptions are listed below:

- An axially dispersed plug model is employed to describe the gas flow through the packed bed column

- The gas phase follows ideal gas behavior
- The mass transfer resistance is mainly due to macropore diffusion and described by the linear driving force (LDF) model
- There are no concentration, temperature and pressure gradients in the radial direction
- Darcy's law is used to represent the pressure drop along the column in the axial direction
- Heat transfer through the column wall is permitted
- The adsorbent properties and bed voidage remains uniform along the column
- The gas and solid phases reach thermal equilibrium instantaneously

Based on the above assumptions, total mass balance, (n_{comp}-1) component balances, energy balance within the column and across the column wall and pressure drop along the column are to be solved. The detailed equations are given below:

Solid phase linear driving force model

$$\frac{\partial q_{\text{i}}}{\partial t} = \alpha_{\text{i}}(q_{\text{i}}^{*} - q_{\text{i}}) \tag{3.15}$$

Fluid phase total mass balance

$$\frac{1}{P}\frac{\partial P}{\partial t} - \frac{1}{T}\frac{\partial T}{\partial t} = -\frac{T}{P}\frac{\partial}{\partial z}\left(\frac{P}{T}v\right) - \frac{RT}{P}\frac{1-\epsilon_{\text{B}}}{\epsilon_{\text{B}}}\sum_{i=1}^{n_{\text{comp}}}\frac{\partial q_{\text{i}}}{\partial t} \tag{3.16}$$

Fluid phase component mass balance

$$\frac{\partial y_{\text{i}}}{\partial t} + \frac{y_{\text{i}}}{T}\frac{\partial P}{\partial t} - \frac{y_{\text{i}}}{P}\frac{\partial T}{\partial t} = \frac{T}{P}D_{\text{L}}\frac{\partial}{\partial z}\left(\frac{P}{T}\frac{\partial y_{\text{i}}}{\partial z}\right) - \frac{T}{P}\frac{\partial}{\partial z}\left(\frac{y_{\text{i}}P}{T}v\right) - \frac{RT}{P}\frac{1-\epsilon_{\text{B}}}{\epsilon_{\text{B}}}\frac{\partial q_{\text{i}}}{\partial t} \tag{3.17}$$

Column energy balance

$$\begin{aligned}\left[\frac{1-\epsilon_{\text{B}}}{\epsilon_{\text{B}}}\left(\rho_{\text{s}}C_{\text{p,s}} + C_{\text{p,a}}\sum_{i=1}^{n_{\text{comp}}}q_{\text{i}}\right)\right]\frac{\partial T}{\partial t} &= \frac{K_{\text{z}}}{\epsilon_{\text{B}}}\frac{\partial^2 T}{\partial z^2} - \frac{C_{\text{p,g}}}{R}\frac{\partial P}{\partial t} - \frac{C_{\text{p,g}}}{R}\frac{\partial}{\partial z}(vP) \\ -\frac{1-\epsilon_{\text{B}}}{\epsilon_{\text{B}}}C_{\text{p,a}}T\sum_{i=1}^{n_{\text{comp}}}\frac{\partial q_{\text{i}}}{\partial t} + \frac{1-\epsilon_{\text{B}}}{\epsilon_{\text{B}}}\sum_{i=1}^{n_{\text{comp}}}&\left(\left(-\Delta H\right)\frac{\partial q_{\text{i}}}{\partial t}\right) - \frac{2h_{\text{in}}}{\epsilon_{\text{B}}r_{\text{in}}}(T - T_{\text{w}})\end{aligned} \tag{3.18}$$

Column wall energy balance

$$\rho_{\text{w}}C_{\text{p,w}}\frac{\partial T_{\text{w}}}{\partial t} = K_{\text{w}}\frac{\partial^2 T_{\text{w}}}{\partial z^2} + \frac{2r_{\text{in}}h_{\text{in}}}{r_{\text{out}}^2 - r_{\text{in}}^2}(T - T_{\text{w}}) - \frac{2r_{\text{out}}h_{\text{out}}}{r_{\text{out}}^2 - r_{\text{in}}^2}(T_{\text{w}} - T_{\text{a}}) \tag{3.19}$$

Pressure drop (Darcy equation)

$$v = \frac{4}{150\mu}\left(\frac{\epsilon_{\text{B}}}{1-\epsilon_{\text{B}}}\right)^2 r_{\text{p}}^2\left(-\frac{\partial P}{\partial z}\right) \tag{3.20}$$

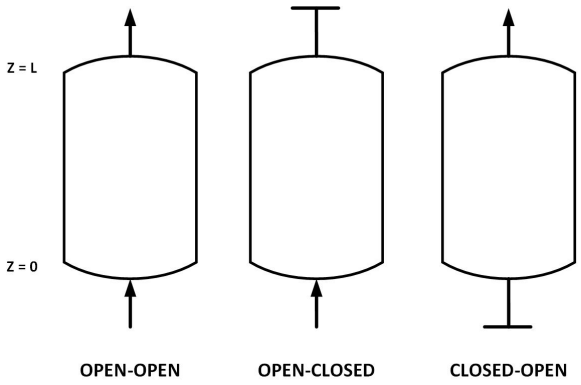

Figure 3.1: Three types of configurations in a PSA cycle that describe the flow direction.

3.3.2 Initial and boundary conditions

Eq.'s 3.15 - 3.20 require appropriate initial and boundary conditions to be solved.

Initial condition

It is always assumed in the simulations that the bed is initially saturated with a weak adsorbing component at a given feed temperature and pressure. For full PSA cycle simulations, the final condition for each step becomes the initial condition for the following step.

Boundary conditions

The boundary conditions for key steps in a PSA cycle can be categorized into three possible configurations, as , Open-Open, Open-Closed and Closed-Open as shown in Fig. 3.1.

Open-Open: The component mass balance follows Danckwert's boundary conditions for a dispersed plug flow system.

$$D_{\mathrm{L}} \frac{\partial y_{\mathrm{i}}}{\partial z} \bigg|_{z=0} = -v \mid_{z=0} \left(y_{\mathrm{i,feed}} - y_{\mathrm{i}} \mid_{z=0} \right) \tag{3.21}$$

$$\frac{\partial y_{\mathrm{i}}}{\partial z} \bigg|_{z=L} = 0 \tag{3.22}$$

The boundary conditions for column energy balance (Eq. 3.18) can be written using the analogy between mass and heat transfer.

$$\frac{\partial T}{\partial z} \bigg|_{z=0} = -\epsilon_{\mathrm{B}} \rho_{\mathrm{g}} C_{\mathrm{p,g}} v \mid_{z=0} \left(T_{\mathrm{feed}} - T \mid_{z=0} \right) \tag{3.23}$$

$$\frac{\partial T}{\partial z} \bigg|_{z=L} = 0 \tag{3.24}$$

Eq. 3.19 has the following boundary conditions:

$$T_{\mathrm{w}}\,\big|_{z=0} = T_{\mathrm{w}}\,\big|_{z=L} = T_{\mathrm{a}} \tag{3.25}$$

Since the total mass balance equation is second order in pressure, two boundary conditions are required. As the velocity at inlet is known, the pressure at inlet is calculated using Darcy's law. The pressure at exit is held constant.

$$v\,\big|_{z=0} = v_{\mathrm{feed}} \tag{3.26}$$

$$P\,\big|_{z=L} = P_{\mathrm{H}} \tag{3.27}$$

Open-Closed: In this type, the column inlet is open and column exit is closed. The boundary conditions for Eq.'s 3.17, 3.18 and 3.19 remain same as Open-Open (i.e. no change in Eq.'s 3.21-3.25). The pressure boundary conditions will change as follows:

The pressure at inlet will be an exponential function, written as,

$$P\,\big|_{z=0} = P_{\mathrm{L}} + (P_{\mathrm{H}} - P_{\mathrm{L}})e^{-\alpha_{\mathrm{p}}t} \tag{3.28}$$

α_{p} is the rate of pressurization or depressurization and is set to 0.5 s^{-1} for all simulations, so as to match experimental pressure profile [34].

The velocity at exit, $v\,\big|_{z=L}$=0, results in pressure boundary condition (from Eq. 3.20)

$$\left.\frac{\partial P}{\partial z}\right|_{z=L} = 0 \tag{3.29}$$

Closed-Open: Here, the column inlet is closed and column exit is open. Therefore, $v\,\big|_{z=0}$=0. Eq.'s 3.22, 3.24 and 3.25 are not affected. Eq.'s 3.21, 3.23 reduce to

$$\left.\frac{\partial y_{\mathrm{i}}}{\partial z}\right|_{z=0} = 0 \tag{3.30}$$

$$\left.\frac{\partial T}{\partial z}\right|_{z=0} = 0 \tag{3.31}$$

$v\,\big|_{z=0}$=0 leads to

$$\left.\frac{\partial P}{\partial z}\right|_{z=0} = 0 \tag{3.32}$$

The pressure at exit will again be an exponential function and is written as,

$$P\,\big|_{z=L} = P_{\mathrm{H}} + (P_{\mathrm{L}} - P_{\mathrm{H}})e^{-\alpha_{\mathrm{p}}t} \tag{3.33}$$

α_{p} is the rate of depressurization and is set to 0.5 s^{-1} for all simulations, so as to match experimental pressure profile.

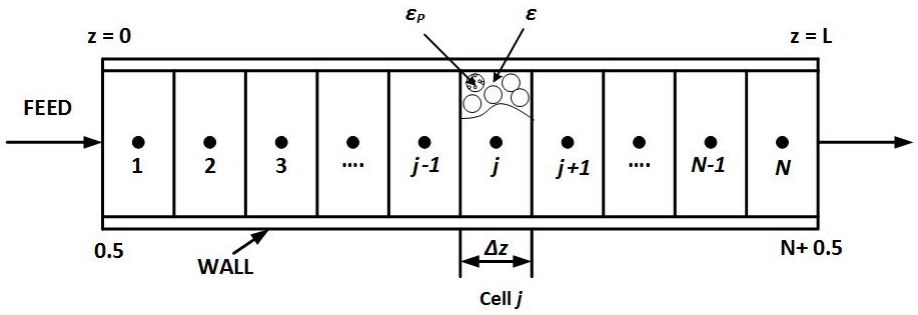

Figure 3.2: Schematic of an adsorption column with spatial discretization using finite volume methodology. Adapted from [42].

3.3.3 Finite volume methodology

The partial differential equations describing the PSA process cannot be solved analytically. Therefore, a suitable numerical method has to be employed to find the approximate solution. It is necessary to accurately make approximations to limit the discontinuities that lead to computational difficulties. Several numerical schemes were employed for simulating adsorption processes, such as, finite difference [35], orthogonal collocation [36], finite element [37] and finite volume method [38–40]. The partial differential equations solved in this work are hyperbolic in nature with sharp discontinuities. Among the methods available, finite volume method offered the stability and robustness and was found that it is computationally less intensive, providing much accurate solution to PSA model [41,42]. In finite volume methods, the integral form of conserved quantity f is solved. This ensures better closure of the quantity f. The formulation of finite volume method used for PSA simulations in this work is described below.

Formulation of the finite volume scheme

In finite volume method (FVM), the domain is divided into a finite number of control volumes (CV's). The integral form of the conservation equation is discretized, which automatically guarantees the property of conservation of equations over each control volume [43]. The advantage of using finite volume method is the flux within a control volume is always conserved. With the implementation of appropriate boundary conditions, the flux over the entire domain is conserved. The finite volume method, in its integral form holds good for control volume that has discontinuities.

For the given system, the one-dimensional spatial domain is discretized using a finite volume scheme as shown in Fig. 3.2. In this approach, the spatial derivatives are converted to algebraic expressions by integrating over each control volume.

$$f_{\mathrm{j}}(t) = \frac{1}{\Delta V} \int_{V_{\mathrm{j}}} f(t) dV \tag{3.34}$$

Eq. (3.34) represents any conserved quantity f approximated using the integral average over control volume V_{j} with boundaries $j - 0.5$ and $j + 0.5$. The quantity f_{j} represents the value at the center of control volume j.

Numerical flux-limiters for the finite volume scheme

For many hyperbolic problems, the waves propagate with different speeds, perhaps in different directions. Therefore, to obtain an accurate and non-oscillatory solution, the flux-limiters are to be defined appropriately [44]. Upwind difference scheme (UDS) is one such flux-limiter where the information on the flux entering the edge $j + 0.5$ is entirely determined by the information on the flux at the preceding control volume, j.

$$f_{\mathrm{j+0.5}} = f_{\mathrm{j}} \tag{3.35}$$

The upwind scheme is a first-order approximation. The advantage with upwind scheme is it keeps the solution monotonically varying in the regions where the solution is monotone [44]. Though it produces a non-oscillatory solution, it brings numerical dispersion into the system due to first order approximation leading to low accuracies [44].

In order to reduce the numerical dispersion and increase the accuracy, while producing a non-oscillatory solution, a total variation diminishing (TVD) based flux limiter is employed. In TVD scheme, the oscillation in the solution is measured using

$$TV = |f_{\mathrm{j}} - f_{\mathrm{j-1}}| \tag{3.36}$$

where TV is the total variation, f_{j} and $f_{\mathrm{j-1}}$ are the fluxes in the control volumes j and$j - 1$.

The TVD methods reduce the nonphysical oscillations around discontinuities, while ensuring the smoothness of the solution [44]. The smoothness of a solution $r_{\mathrm{j+0.5}}$ can be defined using a successive slope ratio, given below,

$$r_{\mathrm{j+0.5}} = \frac{f_{\mathrm{j}} - f_{\mathrm{j-1}} + \delta}{f_{\mathrm{j+1}} - f_{\mathrm{j}} + \delta} \tag{3.37}$$

The right hand side represents the ratio of successive gradients on a finite volume stencil. δ is a very small number, in the order of 10^{-10}. When the solution is smooth, $r_{\mathrm{j+0.5}} \simeq 1$ and when there is a discontinuity, $r_{\mathrm{j+0.5}}$ is far away from 1. The flux entering the edge of control volume $j + 0.5$ using TVD scheme is given as

$$f_{\mathrm{j+0.5}} = f_{\mathrm{j}} + \frac{1}{2}\phi(r_{\mathrm{j+0.5}})(f_{\mathrm{j+1}} - f_{\mathrm{j}}) \tag{3.38}$$

ϕ is the flux limiter function, whose value depends on the smoothness. Although several flux limiters are defined [44], in this work, van Leer flux limiter function, a high resolution limiter is employed as it performed better than other flux limiter functions in terms of convergence and computational time [42]. The van Leer flux limiter is defined as

$$\phi(r_{\mathrm{j+0.5}}) = \frac{r_{\mathrm{j+0.5}} + |r_{\mathrm{j+0.5}}|}{1 + |r_{\mathrm{j+0.5}}|} \tag{3.39}$$

The calculation of the flux at the control volume edge $j + 0.5$ requires the values at $j - 1$ and $j + 1$. The boundary conditions are implemented at the edges $j = 0.5$ and $j = N + 0.5$. For $j = 2, ...N$, the calculation is straightforward since all the values are available. In order to calculate the values for control volume $j = 1$, the values in the control volumes j=0, 1 and 2 are required. While the values at j=1 and 2 are known, values at $j = 0$ are unknown. To overcome this, a half-control volume approximation is made for $j = 0$ and it is assumed that the change in the variable from $j = 0.5$ to $j = 1$ is same the change in the variable from $j = 0$ to $j = 0.5$.

$$f_1 - f_0 = 2(f_1 - f_{0.5}) \tag{3.40}$$

In this work, the PSA cycles are simulated using the finite volume methodology, discussed above, for spatial discretization. The space domain was divided into 30 control volumes. The partial differential equations in space and time transform to ordinary differential equation (ODE) in time after spatial discretization. For solving ODE, ode23s, an inbuilt stiff ODE solver in MATLAB was employed to obtain the solution for PSA process.

3.3.4 Basic 4-step PSA cycle

A variety of PSA cycles have been developed for different separation processes and reported in the literature [15]. A simple PSA cycle consisting of adsorption, blowdown, evacuation and feed pressurization steps is considered to determine the model competency. Fig. 3.3 shows the schematic of a basic 4-step cycle. The unique feature of each step is discussed below.

Adsorption

In adsorption (ADS) step, the feed is sent into the column at z=0 at pressure P_{H} and temperature T_{feed}. The strongly adsorbing component gas prefentially adsorbs on solid adsorbent when compared to the weakly adsorbing component gas. The end z=L, is kept open and the weakly adsorbing component is collected. This step falls into the open-open category as discussed earlier in this chapter.

Co-current Blowdown

The feed end of the column z=0 is closed for this step and the other end z=L is kept open, so that the pressure in the column reduces from a pressure P_{H} to P_{INT}. In this step, the residual weakly adsorbing component is removed both from gas and solid phases, thereby leaving the

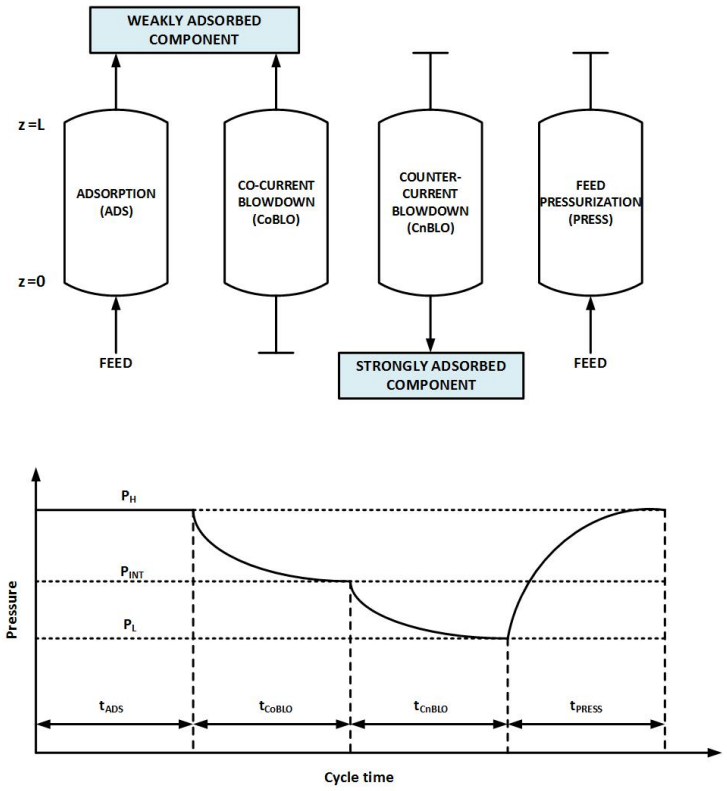

Figure 3.3: Basic 4-step PSA cycle with adsorption (ADS), co-current blowdown (CoBLO), counter-current blowdown (CnBLO) and feed pressurization (PRESS).

column predominantly with strongly adsorbing component gas. Closed-open boundary condition is applied to this step.

Counter-current Blowdown

The feed end of the column z=0 is opened while keeping the end z=L closed to extract all the strongly adsorbing component gas present in the column. In this step, the pressure is further reduced from P_{INT} to P_{L}. The bed is regenerated after this step. The boundary condition used in this step is a closed-open condition.

Feed Pressurization

In this step, the column is pressurized from P_{L} to P_{H}. The pressurization is done using feed from the end z=0, while keeping the end z=L closed. Open-closed boundary condition is implemented. This step completes the cycle by attaining the pressure P_{H}, after which adsorption step can be performed. The pressurization and depressurization are performed using a pre-defined exponential pressure profile.

3.3.5 Model validation

Pressure swing adsorption is a dynamic process, unlike distillation which is a static steady state process. So, the PSA cycle has to reach a cyclic steady state (CSS), defined as, the state when the concentration, temperature and pressure profiles do not change with increasing number of cycles and when the mass balance for the cycle is closed. The PSA process attains CSS after completing multiple cycles. As the number of cycles increase, the mass balance error ($\varepsilon_{\mathrm{MB}}$) for the process decreases. The mass balance error ($\varepsilon_{\mathrm{MB}}$) is defined as,

$$\varepsilon_{\mathrm{MB}} = \frac{|\text{moles in} - \text{moles out}|}{\text{moles in}} \times 100 \tag{3.41}$$

Considering the adsorption step, a general mass balance of the column will be of the form:

$$\text{moles in} - \text{moles out} = \text{moles accumulated} \tag{3.42}$$

$$\text{moles in} = A\epsilon \int_0^{t_{\mathrm{step}}} \left[\frac{P_{\mathrm{in}}(t) y_{\mathrm{in}}(t)}{RT_{\mathrm{in}}(t)} v_{\mathrm{in}}(t) \right] dt \tag{3.43}$$

$$\text{moles out} = A\epsilon \int_0^{t_{\mathrm{step}}} \left[\frac{P_{\mathrm{out}}(t) y_{\mathrm{out}}(t)}{RT_{\mathrm{out}}(t)} v_{\mathrm{out}}(t) \right] dt \tag{3.44}$$

$$\text{moles accumulated} = \text{moles accumulated in gas phase} + \text{moles accumulated in solid phase} \tag{3.45}$$

$$\text{moles accumulated (gas phase)} = A\epsilon \int_{z=0}^{z=L} \left[\frac{P(z)y(z)}{RT(z)} \Big|_{final} - \frac{P(z)y(z)}{RT(z)} \Big|_{initial} \right] dz \tag{3.46}$$

$$\text{moles accumulated (solid phase)} = A(1-\epsilon) \int_{z=0}^{z=L} [q(z) \mid_{final} - q(z) \mid_{initial}] dz \tag{3.47}$$

where A, ϵ, L and q are the cross-sectional area, bed voidage, length of the column and solid phase concentration respectively.

The system is said to attain CSS when the mass balance error ($\varepsilon_{\mathrm{MB}}$) is less than 0.5% for five consecutive cycles and there are no changes in column state variables. The criteria for stopping the simulation is attaining the CSS. The performance indicators for the PSA process viz. Purity, Recovery, Energy and Productivity are calculated after CSS. The simulation assumes a single column undergoing the four steps sequentially. The initial state for each step will be the final state of the previous step. A simulation is carried out for the PSA cycle discussed in the previous section, based on the process variables given in Table 3.1. Fig. 3.4 shows the mass balance error as a function of the number of cycles. The mass balance error ($\varepsilon_{\mathrm{MB}}$) decreases as the number of

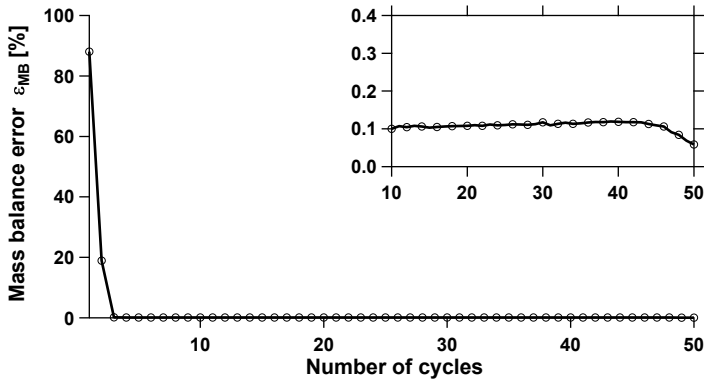

Figure 3.4: Decrease in mass balance error ($\varepsilon_{\mathrm{MB}}$) with number of cycles. The inset shows the zoomed portion.

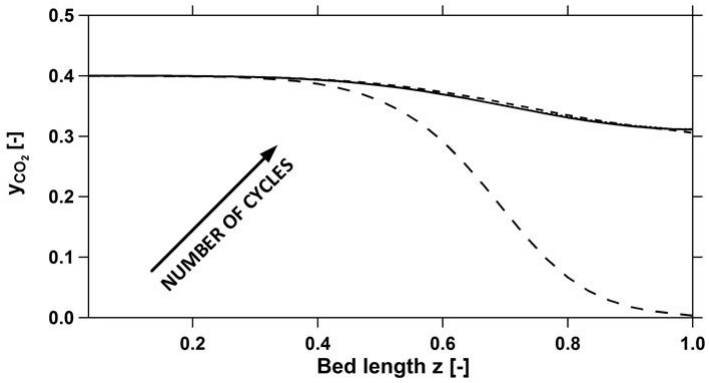

Figure 3.5: Gas phase concentration profiles of CO_2 (y_{CO_2}) in adsorption step with number of cycles.

cycles increase. The simulation was carried out till the mass balance error in the system is less than 0.1%.

Table 3.1: Process variables for model validation.

$\mathbf{y_{feed,\ CO_2}}$ [-]	$\mathbf{t_{ADS}}$ [s]	$\mathbf{t_{CoBLO}}$ [s]	$\mathbf{t_{CnBLO}}$ [s]	$\mathbf{P_H}$ [bar]	$\mathbf{P_{INT}}$ [bar]	$\mathbf{P_L}$ [bar]	$\mathbf{v_{feed}}$ [m/s]
0.4	40	45	95	34.5	12	10	0.1

Fig. 3.5 shows the gas phase concentration profile of CO_2 along the axial direction in the adsorption step. As the number of cycles are increased, the profiles converge as they satisfy mass balance constraints. The system has reached cyclic steady state as there is no change in concentration profile and also mass balance constraint is satisfied. The validated model is used for various simulations carried out at different conditions in the subsequent chapter.

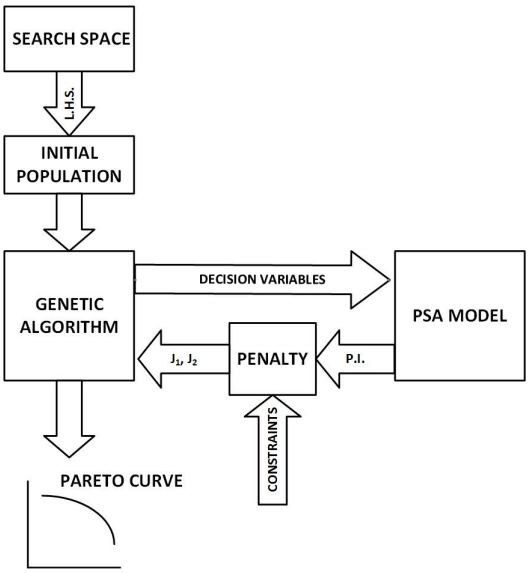

Figure 3.6: Typical genetic algorithm (GA) flowchart. Note: L.H.S is Latin Hypercube Sampling. P.I. are the performance indicators. J_1, J_2 are the objective functions obtained after the cycle attains CSS.

3.4 Optimization framework

Regulatory bodies like US Department of Energy (DOE) have set process performance requirements for CO_2 capture technologies [45]. Therefore, the PSA cycles designed, are to be optimized to meet DOE requirements of CO_2 purity of 95% and CO_2 recovery of 90% respectively. To accomplish this, a rigorous unconstraint optimization has to be performed to identify the operating conditions that would meet both the purity and recovery requirements simultaneously. The energy consumption and productivity of a CO_2 capture process are indirect measure of the operating costs. Therefore, minimizing energy consumption and maximizing productivity of a capture process is important. A second process optimization problem has to be solved to identify the operating conditions of a PSA process that minimize the energy consumption and maximize the productivity of a PSA process under the constraints of CO_2 purity and CO_2 recovery.

To solve these multi-objective optimization problems, a non-dominated sorting genetic algorithm (NSGA-2) which is available in MATLAB global optimization toolbox is employed [46]. Genetic algorithm (GA) solves optimization problems by mimicking the evolution of biological species. It avoids getting trapped into local minima and ensures population diversity. These desirable characteristics make GA solve multi-objective optimizations very efficiently to obtain global minima.

3.4.1 Solution Methodology

Fig. 3.6 shows the typical flowchart of genetic algorithm (GA). GA randomly chooses an initial population from the combination of different decision variables. It then evaluates fitness rank for each member of an initial population and sorts its members based on lower fitness rank. The optimizer creates a parent population by using binary selection of the sorted population. An offspring population is generated from parent population, either by crossover between the members of parent population or by mutation, where changes are made to a single parent. In every generation, an offspring population replaces parent population and advance towards the optimal solution. The optimizer continues to generate offsprings from parent population till a stopping criteria is set. The stopping criteria can be either number of generations or tolerances for objective functions. GA is stochastic in nature and is parallelizable in MATLAB which can speed-up the optimization.

3.4.2 Optimizer with PSA model

The optimizer is coupled with the detailed PSA model to optimize the different PSA cycle configurations. The decision variables for the optimization problem are PSA process operating conditions, viz. step times, operating pressures, feed velocity etc.. The bounded values for all decision variables generate a multi-dimensional searching space for the optimizer. From this space, the optimizer randomly uses an initial population based on Latin-Hypercube sampling (LHS), a sampling technique based on probability distribution.

Two objective functions are formulated in the PSA model depending on the optimization problem. The objective functions are usually the performance indicators, namely, CO_2 purity, CO_2 recovery, energy or productivity, which are calculated after the PSA model reaches CSS. The optimizer runs till the stopping criteria is met. In the constrained optimization problem, the objective function is penalized if the desired constraints are not met and has to re-evaluate the fitness for each member of the population. Once the stopping criteria is met, the optimizer generates a Pareto curve. Each point in the Pareto curve represents the performance indicators evaluated at CSS for corresponding set of decision variables. The Pareto curve indicates the set of optimal solutions obtained from the best tradeoff between the two conflicting objective functions. Any point below the Pareto curve is considered to be sub-optimal and any point above the Pareto curve is considered to be infeasible. The points on the Pareto curve correspond to the best process configuration of a PSA cycle under given constraints.

The results discussed in this work correspond to the optimized solutions obtained after running the optimizations for a maximum of 25 generations. Initial population for the optimizer is generated by using LHS. The initial population is created in MATLAB using a built-in function for LHS and is coupled with the optimizer. A population size of 144 is chosen to perform the multi-objective optimizations. Larger the population size, larger would be the computational

times. The lower and upper bounds are chosen for the decision variables depending on the information from pilot plant studies [41].

The optimizations are performed using 16 cores Intel Xeon (R) 3.1 GHz machine with 128GB RAM. A typical purity-recovery optimization needed 8-16 hours for generating a Pareto curve, while the constraint energy-productivity optimization took 4-10 days for obtaining Pareto curve.

3.5 Conclusions

In this chapter, an adsorption isotherm model is discussed which will be used in the subsequent chapter to describe the adsorption behavior between adsorbate and adsorbent. A complete and robust PSA model is presented with appropriate boundary conditions. The model takes into account the dynamics of a pressure swing adsorption process. Finite volume method with van Leer scheme is used to discretize the set of partial differential equations in space. The methodology employed is found to be robust, accurate and efficient requiring just 30 control volumes so as to capture the dynamics. The simulation performed proved the capability of the model satisfying mass balance constraints to reach a cycle steady state. A multi-objective optimization is framed using genetic algorithm. The genetic algorithm toolbox in MATLAB is parallelizable and coupled with the PSA model to increase the performance of different PSA processes, discussed in the subsequent chapter.

Chapter 4

Process optimization for different PSA cycle configurations

4.1 Introduction

In this chapter, pre-combustion CO_2 capture is studied using four different PSA cycle configurations. TDA AMS-19 material is used as an adsorbent for proposed PSA cycle configurations. A basic 4-step PSA cycle presented in Chapter 3 is modified to different configurations so as to explore the potential of an adsorption-based separation for pre-combustion CO_2 capture. The parasitic energy due to CO_2 capture and storage is important and is one of the factors to decide the practicality of any separation process. Hence, a detailed energy model is formulated to predict the parasitic energy due to PSA process when integrated to an IGCC power plant. A rigorous multi-objective optimization framework is set up to maximize the performance of PSA cycles. The PSA cycles which met the regulatory requirements are considered for a second multi-objective optimization under the constraints. The Pareto curves obtained from the optimizations are presented.

4.2 Adsorption equilibria

The adsorption equilibria is an important input to the design of a PSA process. The adsorption isotherm for CO_2 on TDA AMS-19 were experimentally measured at three different temperatures (viz. 180 °C, 240 °C, 300 °C) over a wide range of pressures at TDA Research Inc.. The isotherms were obtained through breakthrough experiments [34]. The breakthrough experiments involve an adsorption and a desorption experiment. In adsorption experiment, a known molar flow rate Q_{in} and concentration C_{in} of the gas is fed into the column, while in the desorption experiment, the outlet molar flow rate Q_{out} and concentration C_{out} are monitored. The equilibrium solid phase loading in the column at the experimental temperature and pressure is calculated using a mass balance. The moles accumulated after correcting for dead volumes, is calculated as

$$n_{\text{CO}_2,\text{ADS}} = \int_{t=0}^{t=t_{\text{ADS}}} (Q_{\text{in}} C_{\text{in}} - Q_{\text{out}} C_{\text{out}}) dt \tag{4.1a}$$

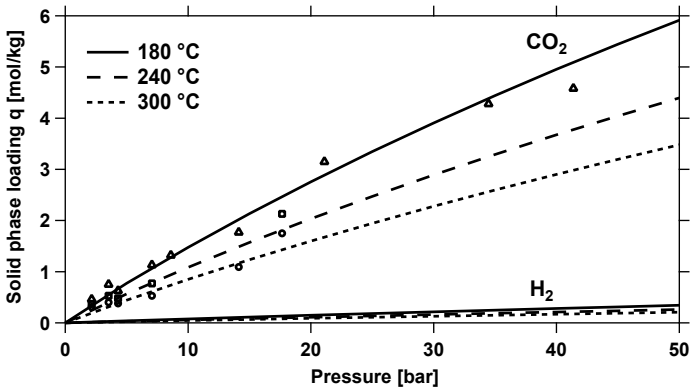

Figure 4.1: Single component isotherms for CO_2 (fitted to TDA experimental equilibria data) and H_2 (obtained from literature for activated carbon) at different temperatures. Lines represent the fitted Sips isotherm and symbols represent the experiments for different temperatures 180°C (triangles), 240 °C (squares) and 300 °C (circles).

$$n_{\mathrm{CO_2,DES}} = \int_{t=0}^{\infty} Q_{\mathrm{out}} C_{\mathrm{out}} dt \tag{4.1b}$$

The equilibrium solid phase loading for given pressure and temperature is obtained from Eq.'s 4.1a and 4.1b. The heat of adsorption ($\Delta H_{ads} \approx$ 20.5 kJ/mol) for CO_2 on TDA AMS-19 was measured and provided by TDA Research Inc [34]. Heat of adsorption represents the strength of interactions between the adsorbate and adsorbent. It is a measure to determine the energy required for adsorbent regeneration and provides an estimate of temperature change in the adsorption column during adsorption and desorption steps.

The adsorption behavior of CO_2 on TDA AMS-19 was fitted using a Sips isotherm model because it provided a better fit at low pressures [34]. The hydrogen isotherm was not available on TDA-AMS-19, hence the Sips isotherm parameters for H_2 on activated carbon were obtained from the literature [47].

The Sips isotherm model [Eq. 3.4] consists of eight parameters (ω_i, ψ_i, θ_i, ϕ_i, $s_{1,i}$, $s_{2,i}$, T_{ref}, $s_{ref,i}$). The experimental data available at different temperatures and over a range of pressures, is fitted to the isotherm model by performing a nonlinear regression. The hydrogen data from literature is fitted to isotherm model. The fitted isotherm parameters for both the components CO_2 and H_2 are listed in Table 4.1. Fig. 4.1 shows the single component isotherms for CO_2 and H_2 at three different temperatures 180 °C, 240 °C and 300 °C . The competition between the components has been accounted using an extended Sips isotherm model discussed in Chapter 3.

4.3 PSA cycle configurations

A variety of PSA cycles were designed for pre-combustion CO_2 capture on TDA AMS-19 material [34]. The basic 4-step PSA cycle discussed in Chapter 3 was considered as a base case. Later,

Table 4.1: Single component Sips isotherm parameters.

	ω_{i} [mol kg^{-1}]	ψ_{i} [kJ mol^{-1}]	θ_{i} [Pa^{-1}]	ϕ_{i} [kJ mol^{-1}]	$s_{1,\mathrm{i}}$ [-]	$s_{2,\mathrm{i}}$ [-]	s_{ref} [-]	T_{ref} [K]
CO_2	3.74	-7.87	26.9×10^{-9}	-2.05	0.136	0.110	0.760	281
H_2	6.66	0	0.7×10^{-9}	-9.83	0	0	0.956	273

modifications were done to the basic 4-step PSA cycle so as to explore the potential of PSA process for pre-combustion CO_2 capture. Purity and recovery are considered as the performance indicators to evaluate the performance of each cycle configuration.

$$Purity, Pu_{\mathrm{CO_2}}[\%] = \frac{\text{Total moles of } CO_2 \text{ in extract product in one cycle}}{\text{Total moles of gas in extract product in one cycle}} \times 100 \tag{4.2}$$

$$Recovery, Re_{\mathrm{CO_2}}[\%] = \frac{\text{Total moles of } CO_2 \text{ in extract product in one cycle}}{\text{Total moles of } CO_2 \text{ fed into the column in one cycle}} \times 100 \tag{4.3}$$

$$Purity, Pu_{\mathrm{H_2}}[\%] = \frac{\text{Total moles of } H_2 \text{ in raffinate product in one cycle}}{\text{Total moles of gas in raffinate product in one cycle}} \times 100 \tag{4.4}$$

$$Recovery, Re_{\mathrm{H_2}}[\%] = \frac{\text{Total moles of } H_2 \text{ in raffinate product in one cycle}}{\text{Total moles of } H_2 \text{ fed into the column in one cycle}} \times 100 \tag{4.5}$$

4.3.1 Configuration A: Basic 4-step PSA cycle

This cycle configuration consists of feed pressurization, adsorption, co-current blowdown and counter-current blowdown steps as shown in Fig. 4.2(a). The key features of each step was earlier discussed in Chapter 3. The feed with molar composition of 40% CO_2 and 60% H_2 enters the column at feed end (z=0) in the adsorption step. At the light product end (z=L), weakly adsorbing component H_2 is collected, while the strongly adsorbed CO_2 remains in the column. The adsorption step is followed by a co-current blowdown where residual H_2 present in the column is further removed at the light product end. Subsequently CO_2 is extracted in the counter-current blowdown step to regenerate the column, followed by feed pressurization.

4.3.2 Configuration B: 6-step PSA cycle with counter-current blowdown, purge, pressure equalization and light product pressurization

The basic 4-step PSA cycle is modified to 6-step PSA cycle by introducing the purge, pressure equalization steps and replacing the feed pressurization with light product pressurization step. The schematic of configuration B is shown in Fig. 4.2(b).

Light product pressurization: The feed pressurization step is replaced by light product

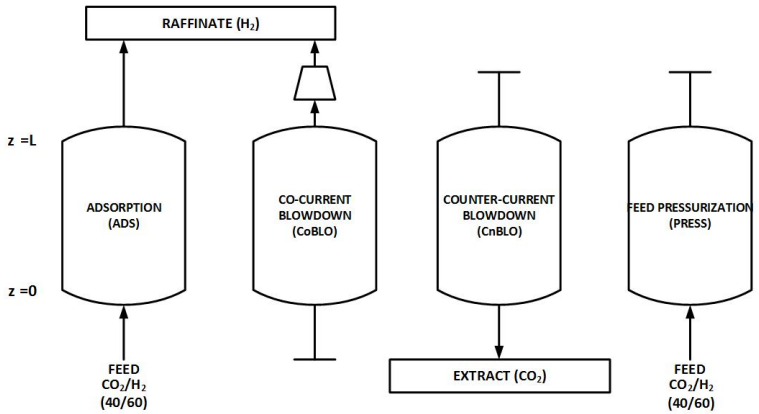

(a) Basic 4-step PSA cycle

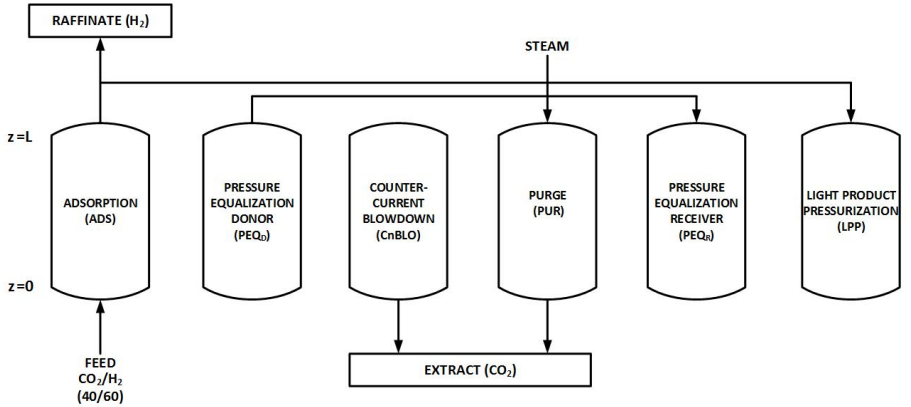

(b) 6-step PSA cycle with counter-current blowdown, purge, pressure equalization and light product pressurization

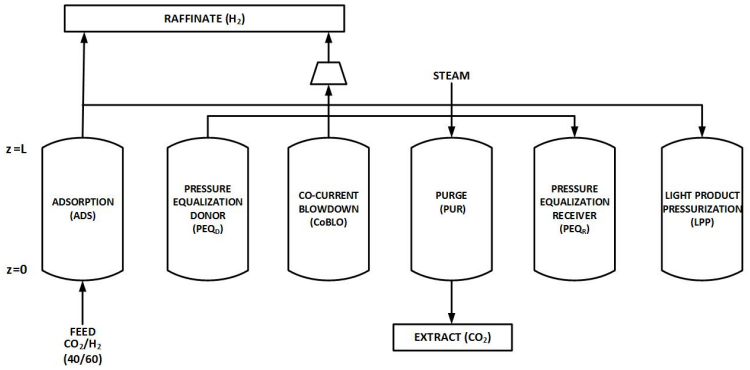

(c) 6-step PSA cycle with co-current blowdown, purge, pressure equalization and light product pressurization

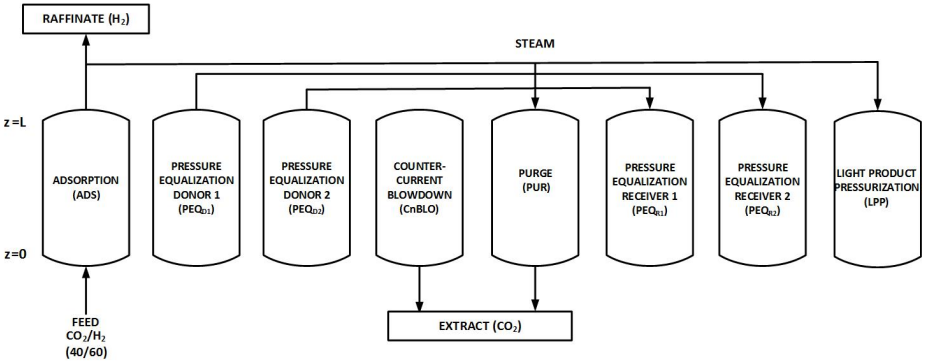

(d) 8-step PSA cycle with counter-current blowdown, purge, two pressure equalizations and light product pressurization

Figure 4.2: Different PSA cycle configurations considered in this study.

pressurization (LPP). In LPP step, a part of raffinate product from adsorption step is sent back to column for pressurization. This will help in improving the CO_2 recovery, as the CO_2 slipping out in the light product stream in adsorption step is sent back to the column. However, by doing this, H_2 recovery reduces as the part of H_2 will also be fed back into the column. The feed conditions to LPP step are the outlet conditions of the adsorption step. This was modeled using a data buffer where the profiles at the exit of the adsorption step are stored. A feed pressurization step is added to LPP, if the desired pressure is not achieved by LPP alone. The advantage of LPP step is that it flattens the CO_2 front from the previous step, thereby preventing the CO_2 loss in the adsorption and increasing the CO_2 recovery.

Purge step: A purge step is introduced to flush the column in order to remove any residual CO_2 remaining in the column. Steam at pressure P_{L} is chosen to clean the column since the steam is inert on TDA AMS-19 and does not contaminate the column. A purge step further extracts the CO_2 from the column after counter-current blowdown step, thereby increasing the recovery for CO_2. The outlet stream of purge step will be a wet stream. The performance indicators purity and recovery reported in this work are on dry basis.

Pressure equalization: A pressure equalization (PE) consists of a donor and a receiver columns. In donor step, depressurization from P_{H} to P_{INT} occurs, similar to co-current blowdown step. However, the exit stream of donor step is sent back to a receiver column which is used for pressurizing the receiver column. Thus, CO_2 lost in donor column is recovered in the receiver step, increasing the CO_2 recovery. Another advantage of replacing the co-current blowdown step with pressure equalization (PE) is that the light product H_2 is collected only at pressure P_{H} in adsorption step, when compared to a co-current blowdown step delivering H_2 at a lesser pressure P_{INT}, thereby avoiding additional compression of H_2. The intermediate pressure P_{INT} cannot be arbitrarily fixed and depends on pressure levels P_{H} and P_{L}. The P_{INT} is estimated using an empirical correlation that was obtained by running a local optimization to minimize the difference between the moles going out of donor step and moles going in the receiver column [34]. Since there is no flexibility of changing the intermediate pressure P_{INT}, H_2 recovery can be affected by choice of P_{H} and P_{L}.

4.3.3 Configuration C: 6-step PSA cycle with co-current blowdown, purge, pressure equalization and light product pressurization

Configuration B is modified by replacing the counter-current blowdown step to a co-current blowdown step (show in Fig. 4.2(c)). The co-current blowdown step will remove the H_2 gas present in the column after the pressure equalization donor step. The co-current blowdown is done by depressurizing the column from P_{INT} to P_{L}. Since the H_2 gas is pulled out from the raffinate product end ($z = L$), the residual H_2 present in the column, during the co-current blowdown step, moves towards the raffinate product end. Therefore, in the subsequent purge

using steam, pure CO_2 is extracted out of the column. Therefore, this type of configuration increases the purity of CO_2. The H_2 gas collected in the co-current blowdown step will be at a lower pressure than the H_2 gas obtained in the adsorption step. Therefore, the H_2 from the raffinate product end of co-current blowdown has to be compressed to pressure P_{H}.

4.3.4 Configuration D:8-step PSA cycle with counter-current blowdown, purge, two pressure equalizations and light product pressurization

In this type of configuration, an additional pressure equalization step is added to configuration B. The extra pressure equalization will increase the CO_2 purity. The first donor column is depressurized from P_{H} to P_{INT1}, while the second donor column is depressurized from P_{INT1} to P_{INT2}. The receiver columns gets pressurized from P_{L} to P_{INT1} and P_{INT1} to P_{INT2} using the desorbed moles of gas from the donor steps. The intermediate pressures for pressure equalization steps are determined using an empirical correlations [34]. A local optimization was performed to minimize the difference between the moles of gas leaving the donor step and moles of gas entering the receiver step for two pressure equalization steps. The intermediate pressures were obtained based on this optimization.

4.4 Modeling of energy consumption for CO_2 capture and storage

The addition of a PSA unit to an IGCC power plant introduces auxiliary power consumption. The process design of PSA unit involves designing an energy efficient process. The energy consumption indirectly reflects the operating costs. Hence, minimizing the energy consumption for CO_2 capture and storage is utmost important. In this section, a net energy consumption for CO_2 capture and storage is formulated. The schematic with downstream of PSA unit in IGCC plant is shown in Fig. 4.3. As it is seen in Fig. 4.3, heat is recovered in the system, but it is not accounted while modeling the power consumption because there is no conversion factor available to represent the heat recovered in terms of electricity at this stage. The energy model is formulated for the total electrical power required for operating PSA process.

4.4.1 CO_2 compression

The CO_2 captured from PSA process has to be compressed and delivered for storage at 150 bar. The low pressures in the PSA process vary between 1 bar and 34.5 bar, depending on the design of the process. Therefore, compressing the CO_2 from such low pressures to 150 bar requires a multi-stage compression unit with inter-stage cooling. As the critical pressure of CO_2 is at ≈ 72 bar, the CO_2 stream is compressed from pressure P_{L} to 72 bar using a multi-stage compressors with intercoolers. Beyond 72 bar, the CO_2 is delivered to 150 bar using a pump.

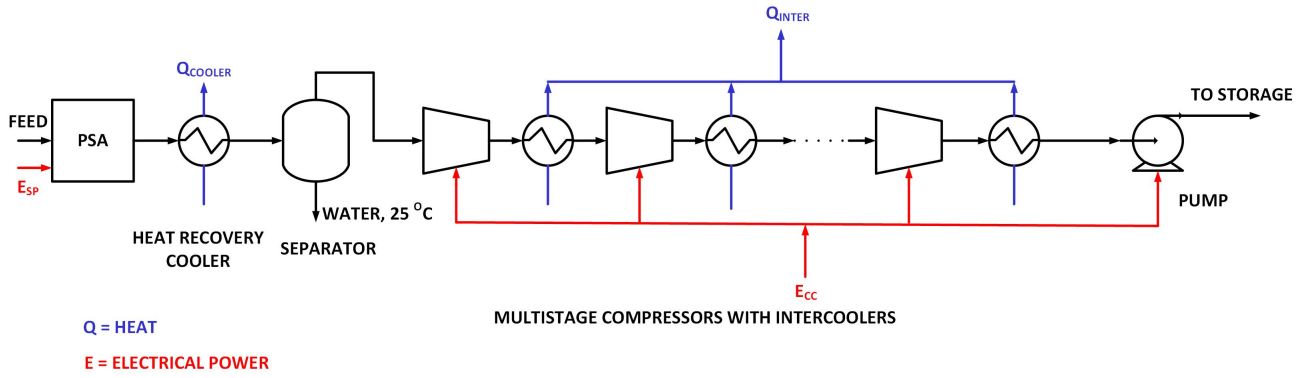

Figure 4.3: Schematic showing the PSA process and CO_2 compression unit. Red lines represents the power consumption while blue lines represents the heat recovery.

Modeling multi-stage compressors

The CO_2 stream enters the multi-stage compression unit at a pressure P_{L}, which depends on the design of a PSA unit. The maximum pressure that can be achieved from multi-stage compression is set to 72 bar. It is assumed that in each stage compression, a maximum pressure ratio of 3 is attained [48].

The number of stages for compression is calculated using,

$$N = \frac{\ln \bar{r}_{\mathrm{o}}}{\ln \bar{r}_{\mathrm{p}}} \tag{4.6}$$

where N is the number of stages, $\bar{r}_{\mathrm{p}}$ is the compression ratio per stage.

$\bar{r}_{\mathrm{o}}$ is the overall compression ratio i.e.

$$\bar{r}_{\mathrm{o}} = \frac{72}{P_{\mathrm{L}}} \tag{4.7}$$

The number of stages, N is rounded off to the next-highest integer and pressure ratio for each compression stage is re-calculated using

$$\bar{r}'_{\mathrm{p}} = \bar{r}_{\mathrm{o}}^{\frac{1}{N}} \tag{4.8}$$

The work done by multi-stage compression is given by,

$$W_{\mathrm{comp}}\left[\frac{\mathrm{kJ}}{\mathrm{s}}\right] = N\frac{1}{\eta_{\mathrm{adia}}} n_{\mathrm{extract}} R T_{\mathrm{in}} \frac{\gamma}{\gamma - 1}\left[(\bar{r}'_{\mathrm{p}})^{\frac{\gamma-1}{\gamma}} - 1\right] \tag{4.9}$$

where,
η_{adia}=80% is the adiabatic efficiency [48];
n_{extract} is the molar flow rate of CO_2 product stream [kmol s^{-1}];
R is the universal gas constant;

T_{in} is the temperature at which the CO_2 product stream enters the compressor. It is assumed that the stream to the compressor is cooled to 25°C using interstaged coolers. i.e. T_{in}=298.15 K;
γ is the specific heat ratio.

Assuming 100% driver efficiency, the electrical power consumption, E_{comp}, for multi-stage compression is as follows:

$$E_{\text{comp}}[kW_{\text{e}}] = W_{\text{comp}} \tag{4.10}$$

Modeling pump power consumption

After CO_2 product stream attains a supercritical state, the stream is delivered to 150 bar using a pump. While calculating the pump energy, the following assumptions are made:

- Straight (horizontal) pipes are connected to the pump
- Cross-sectional area of the pipe remains constant
- Negligible frictional losses

The work done by the pump can be calculated from Bernouli's equation. With the assumptions made, the Bernouli's equation reduces to

$$W_{\text{pump}}\left[\frac{\text{kJ}}{\text{s}}\right] = \left[\frac{P_{150}}{\rho_{150}} - \frac{P_{72}}{\rho_{72}}\right]\frac{m_{\text{extract}}}{\eta_{\text{pump}}} \tag{4.11}$$

where,
m_{extract} is the mass flow rate of the CO_2 product stream [kg s^{-1}];
η_{pump}=75% is the overall pump efficiency [49];
ρ_{72} and ρ_{150} are the densities of CO_2 product stream at 72 bar and 150 bar respectively and at a temperature of 298.15 K.

Assuming 100% driver efficiency for the pump, the electrical power consumption, E_{pump} is given as,

$$E_{\text{pump}}[kW_{\text{e}}] = W_{\text{pump}} \tag{4.12}$$

Power consumption for CO_2 compression

The total power consumption for CO_2 compression (E_{CC}) is given by,

$$E_{\text{CC}}[kW_{\text{e}}] = E_{\text{comp}} + E_{\text{pump}} \tag{4.13}$$

Power consumption for CO_2 compression per tonne of CO_2 captured is represented as

$$\psi_{\text{CC}}\left[\frac{\text{kWh}_{\text{e}}}{\text{tonne CO}_2\text{ captured}}\right] = \frac{E_{\text{comp}} + E_{\text{pump}}}{m_{\text{extract}} Pu_{\text{CO}_2}} \tag{4.14}$$

ψ_{CC} is defined as the total power consumption for compression per tonne of CO_2 captured. Pu_{CO_2} is the dry purity of CO_2 product stream.

4.4.2 Steam consumption in PSA unit

The PSA process requires steam to purge out the column for regeneration. In this thesis, it is assumed that the steam consumption required in the PSA process is independent of the steam used or generated in an IGCC power plant. The purge step is carried out at low pressure P_L. A methodology is formulated to calculate the electrical power consumption due to steam in the PSA process for any low pressure P_L. The electrical power consumption is obtained by multiplying the thermal energy of steam with a suitable conversion factor. The thermal energy is the enthalpy content of steam at pressure P_L and temperature T_{steam}.

The enthalpy of steam is calculated using the empirical equations available in the literature [50] [51]. The saturated temperature of the steam based on the pressure P_L [50] can be calculated as,

$$\frac{T_{sat}}{T_c} = \frac{\left\{ \sum_{i=0}^{2} a_i \left[\ln \frac{P_L}{P_c} \right]^i \right\}}{\left\{ \sum_{j=0}^{5} A_j \left[\ln \frac{P_L}{P_c} \right]^j \right\}} \tag{4.15}$$

where T_c=647.096 K and P_c=220.64 bar are the steam critical temperature and pressure respectively. The coefficients used in Eq. 4.15 are given in Table 4.2.

The temperature of the column (T_{col}) after the counter-current blowdown (CnBLO) step in a PSA process determines the temperature at which the steam has to be sent into the column. The steam temperature (T_{steam}) is calculated based on:
If $T_{col} > T_{sat}$ + 15°C,

$$T_{steam} = T_{col} + 15°C \tag{4.16a}$$

else

$$T_{steam} = T_{sat} \tag{4.16b}$$

The steam purge in a PSA process desorbs the CO_2 from adsorbent. Since the desorption process is endothermic, the temperature of steam decreases as it travels along the column. Eq.'s 4.16a and 4.33b ensures no steam condensation in the column by super-heating the steam to 30°C above the saturation conditions.

The specific enthalpy of saturated steam (h_g) is calculated using an empirical equation [51].

Table 4.2: Coefficients used for calculating saturated temperature of the steam.

Coefficient	Value
a_0	1.00
a_1	-3.34
a_2	1.43
A_0	1
A_1	-3.47
A_2	1.88
A_3	-2.12 $\times$ 10^{-1}
A_4	-3.58 $\times$ 10^{-3}
A_5	-9.09 $\times$ 10^{-5}

Table 4.3: Coefficients used for calculating specific enthalpy of the saturated steam.

χ_1	χ_2	χ_3	χ_4	χ_5
64.88	11.76	-11.94	6.29	-0.99

$$\ln h_{\mathrm{g}} = \sqrt{\chi_1 + \chi_2 \Big[\ln \frac{1}{T_{\mathrm{r}}}\Big]^{0.35} + \chi_3 \frac{1}{T_{\mathrm{r}}^2} + \chi_4 \frac{1}{T_{\mathrm{r}}^3} + \chi_5 \frac{1}{T_{\mathrm{r}}^4}} \tag{4.17}$$

where reduced temperature, T_{r}= $\frac{T_{\mathrm{sat}}}{T_{\mathrm{c}}}$. The coefficients are given in Table 4.3. Based on steam temperature (T_{steam}), specific sensible heat (Δh_{g}) is added to h_{g}

$$\Delta h_{\mathrm{g}} = C_{\mathrm{p,steam}}(T_{\mathrm{steam}} - T_{\mathrm{sat}}) \tag{4.18}$$

The specific enthalpy (H_{g}) of steam used in the PSA process is given by Eq. 4.19.

$$H_{\mathrm{g}} = h_{\mathrm{g}} + \Delta h_{\mathrm{g}} \tag{4.19}$$

The electrical power consumption (E_{SP}) is represented as follows:

$$E_{\mathrm{SP}}[kW_{\mathrm{e}}] = \eta_{\mathrm{e}} m_{\mathrm{steam}} H_{\mathrm{g}} \tag{4.20}$$

where m_{steam} is the mass flow rate of steam fed to the PSA unit. η_{e}=0.8 is the conversion factor for converting thermal energy of steam to electricity [52].

$$\psi_{\mathrm{SP}} \left[\frac{\mathrm{kWh_e}}{\text{tonne } \mathrm{CO_2} \text{ captured}}\right] = \frac{E_{\mathrm{SP}}}{m_{\mathrm{extract}} P u_{\mathrm{CO_2}}} \tag{4.21}$$

where ψ_{SP} is defined as the total power consumption for compression per tonne of CO_2 captured, m_{extract} is the mass flow rate of CO_2 product stream.

4.4.3 Separation of steam from CO_2 product

The steam in the CO_2 product stream has to be knocked out before the stream is fed to the compressors. For this, the CO_2 product stream is cooled to 25°C (T_{ref}) and condensed water is

knocked out in the separator as shown in schematic Fig. 4.3. The heat that can be recovered while cooling to 25°C is Q_{cooler}.

$$Q_{\text{cooler}} = m_{\text{p}} C_{\text{p,p}} (T_{\text{p}} - T_{\text{ref}}) + (m_{\text{extract}} - m_{\text{p}})(\lambda_{\text{steam}} + C_{\text{p,steam}}(T_{\text{sat}} - T_{\text{ref}})) \tag{4.22}$$

m_{p} is the mass flow rate of CO_2 product on dry basis;
$C_{\text{p,p}}$ is the specific heat of dry CO_2 gas stream;
T_{p} is the temperature of the gas leaving the column in purge step;
λ_{steam} is the latent heat of steam.

4.4.4 Intercoolers in multi-stage compression

As mentioned earlier in this section, the CO_2 product stream undergoes a multi-stage compression with inter-staged cooling. During compression, the temperature of the gas increases. The hot compressed gas is cooled down to 25 °C using coolers. The heat recovered in the coolers can be integrated to any system in an IGCC power plant. The temperature of the gas is calculated using,

$$T_{\text{comp}} = (\bar{r}'_{\text{p}})^{\frac{\gamma-1}{\gamma}} T_{\text{ref}} \tag{4.23}$$

where, T_{comp} is the final temperature of the gas during single-staged compression.
The heat that can be recovered from N staged coolers, is given by,

$$Q_{\text{inter}} = N m_{\text{p}} C_{\text{p}} (T_{\text{comp}} - T_{\text{ref}}) \tag{4.24}$$

4.4.5 Relation between kg steam required per kg CO_2 captured

In this section, a relation between kg of steam consumed in the PSA process and kg of CO_2 captured is established, which will later be used for a quick analysis of steam consumption.
The main assumptions for deriving this relation are:

- State variables in the column during purge step are uniform along the axial direction
- Steam is fed to the column until all the CO_2 is removed
- CO_2 concentration is uniform along the column

The duration for which the steam has to be supplied is calculated based on the retention time ($t_{\text{R,CO}_2}$) of CO_2 in the column. The retention time can be calculated as,

$$t_{\text{R,CO}_2} = \frac{L}{v_{\text{PUR}}} \left[1 + \frac{1-\epsilon}{\epsilon} H_{\text{CO}_2} \right] \tag{4.25}$$

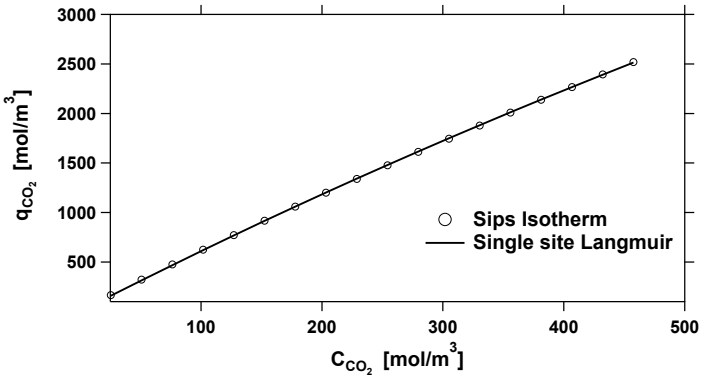

Figure 4.4: Single component isotherm for CO_2 on TDA AMS-19. Circles represent the discretized Sips isotherm points and line represent the fitted single site Langmuir isotherm.

where L is the length of the column; v_{PUR} is the velocity at which CO_2 is purged through the column; ϵ is the bed voidage; and H_{CO_2} is the Henry constant for CO_2.

To determine the Henry constant, the Sips isotherm (Eq. 3.4) is converted to a single-site Langmuir isotherm. The isotherm parameters were estimated by fitting the single-site Langmuir to discretized points of Sips isotherm model (as shown in Fig. 4.4). q_{CO_2} is the solid concentration [mol m^{-3}], while C_{CO_2} is the fluid concentration [mol m^{-3}]. The Henry constant is found out using,

$$H_{CO_2} = q_s b \tag{4.26}$$

q_s and b are single-site Langmuir fitted parameters.

The moles of steam that has to be fed into the column is written as,

$$\text{Moles, steam} = \frac{P_L A \epsilon v_{\mathrm{PUR}} t_R}{R T_{\mathrm{steam}}} \tag{4.27}$$

where A is the cross-sectional area of the column.

The moles of CO_2 that comes out of the column is given by,

$$\text{Moles, } CO_2 = \text{Moles in gas phase} + \text{Moles in solid phase} \tag{4.28a}$$

$$\text{Moles in gas phase} = \frac{P_L P u_{CO_2} A \epsilon L}{R T_{\mathrm{col}}} \tag{4.28b}$$

$$\text{Moles in solid phase} = q_{CO_2} A L (1 - \epsilon) \tag{4.28c}$$

kg steam- kg CO_2 relation is obtained using

$$\frac{\text{kg steam}}{\text{kg } CO_2} = \frac{(\text{Moles, steam}) MW_{\mathrm{steam}}}{(\text{Moles, } CO_2) MW_{CO_2}} \tag{4.29}$$

MW_{steam} and MW_{CO_2} are molecular weights of steam and CO_2, respectively.

4.5 Optimization framework

Genetic algorithm toolbox in MATLAB is employed to run optimizations that maximize the performance of PSA cycles. The process optimization is approached as two sets of problem. The first optimization problem, involves the maximization of purity and recovery, so as to evaluate the performance of a PSA cycle. The optimizer chooses the optimized value with no constraints. The second optimization problem deals with the minimization of electrical power consumption for CO_2 capture and the maximization of productivity of CO_2 captured under the constraints of CO_2 purity and recovery. Although heat is recovered in the system, it is not accounted for while minimizing the power consumption. The objective functions for the first optimization problem are defined as follows:

$$\min\ J_1 = \frac{1}{Pu_{\mathrm{CO_2}}} \tag{4.30a}$$

$$\min\ J_2 = \frac{1}{Re_{\mathrm{CO_2}}} \tag{4.30b}$$

The goal of first optimization is to maximize the performance indicators $Pu_{\mathrm{CO_2}}$ and $Re_{\mathrm{CO_2}}$, hence, the objective functions are defined as the inverse of the performance indicators because genetic algorithm searches for global minima in the given search space.

For the second optimization problem, the performance indicators, Energy (En), which is the total electrical power consumption for PSA and productivity (Pr) are defined as,

$$Energy, En\left[\frac{\mathrm{kWh_e}}{\text{tonne } \mathrm{CO_2} \text{ captured}}\right] = \frac{E_{\mathrm{CC}} + E_{\mathrm{SP}}}{\text{Mass of } \mathrm{CO_2} \text{ in the extract product}} \tag{4.31}$$

$$Productivity, Pr\left[\frac{\text{mol. } \mathrm{CO_2}}{m^3 \text{ adsorbent. s}}\right] = \frac{\text{Total moles of } \mathrm{CO_2} \text{ in the extract product}}{(\text{Total volume of adsorbent})(\text{Total cycle time})} \tag{4.32}$$

Now, the objective functions for second optimization problem are defined as,

$$\min\ J_3 = \psi_1 En + \lambda_1[\max\ (0, Pu_{\mathrm{target}} - Pu_{\mathrm{CO_2}})]^2 + \lambda_2[\max\ (0, Re_{\mathrm{target}} - Re_{\mathrm{CO_2}})]^2 \tag{4.33a}$$

$$\min\ J_4 = \frac{\psi_2}{Pr} + \lambda_1[\max\ (0, Pu_{\mathrm{target}} - Pu_{\mathrm{CO_2}})]^2 + \lambda_2[\max\ (0, Re_{\mathrm{target}} - Re_{\mathrm{CO_2}})]^2 \tag{4.33b}$$

where, ψ_1, ψ_2, λ_1 and λ_2 are penalty factors.

A search space is defined for the optimizer based on the decision variables, which are step times; low pressure, intermediate pressure and feed velocity. The bounds for these decision variables (DV) are a range of operating conditions that were determined using pilot plant studies [41]. The bounds for decision variables are given in Table 4.4 while the PSA simulation parameters are listed out in Table 5.1

Table 4.4: Operating range for decision variables provided to the optimizer.

Configuration	t_{ADS}	t_{CoBLO}	t_{PEQ1}	t_{PEQ2}	t_{CnBLO}	t_{PUR}	P_{INT}	P_L	v_F	v_{PUR}
A	20-100	20-200	-	-	20-200	-	17.3-34.5	1-17.3	0.08-0.5	-
B	20-100	-	20-200	-	20-200	10-80	-	1-17.3	0.08-0.5	0.1-1
C	20-100	20-200	20-200	-	-	10-80	-	1-17.3	0.08-0.5	0.1-1
D	20-100	-	20-200	20-200	20-200	10-80	-	1-17.3	0.08-0.5	0.1-1

The GA optimizer is coupled with detailed PSA model and is parallelized to speed-up the optimization. MATLAB GA global optimization toolbox along with MATLAB parallel computing toolbox is used in this work. The computations are performed in 16 cores Intel Xeon (R) 3.1 GHz machine with 128GB RAM. The stopping criteria set for the optimizations is 25 generations. The population size of 144 is chosen, i.e. 24 times the decision variables for basic 4-step cycle. Larger population sizes lead to longer computational times but allowed the optimizer to search the search space without getting trapped into a local minima.

4.6 Results and discussion

4.6.1 Maximization of Purity-Recovery

A detailed multi-objective optimization is performed to maximize the CO_2 purity and CO_2 recovery simultaneously. The four cycle configurations discussed earlier in this chapter are considered for this optimization. The typical feed mole composition to PSA process is 40% CO_2 and 60% H_2. The regulatory bodies like U.S. Department of Energy has imposed CO_2 purity and recovery requirements of 95% and 90% respectively for sequestration. The PSA cycles considered are subjected to maximization of CO_2 purity-recovery in order to identify the process operating conditions that will satisfy the targets. The framing of optimization problem with a defined search space is presented in the previous section. The optimizer generates a Pareto curve, which is the best trade off between the CO_2 purity-recovery for a given cycle configuration. The Pareto points represent the set of process conditions that can give the optimal CO_2 purity-recovery. The region above Pareto curve is considered to be infeasible to achieve for that cycle configuration.

Fig. 4.5 shows the Pareto curves for all the four PSA cycle configurations considered for this study. The purities and recoveries reported are on dry basis. The basic 4-step cycle (configuration A) had an optimum purity-recovery points less than 90%. Hence, the cycle configuration is not suitable for use. The CO_2 recoveries are much less than other cycle configurations. The loss of CO_2 can either come from adsorption step or co-current blowdown step. Configuration B, has a Pareto front which is far top-right than basic 4-step cycle. The maximum purities that can be achieved using this configuration are limited to 92%. The introduction of pressure equalization step significantly improved the CO_2 recoveries, as the exit stream of pressure equalization step is fed back to the column. The addition of a purge step also contributes to the increase in

Table 4.5: PSA simulation parameters.

Parameter	Value	Source
Column Properties		
Length, L [m]	0.83	Measured
Outer radius, $r_o[m]$	5.715×10^{-2}	Measured
Inner radius, $r_i[m]$	5.118×10^{-2}	Measured
Particle radius, r_p [m]	3×10^{-4}	Measured
Bed voidage, ϵ [-]	0.4	Measured
Particle voidage, ϵ_p [-]	0.57	Measured
Physical Properties		
Adsorbent density, ρ_s [kg m^{-3}]	1361.00	Measured
Specific heat capacity of adsorbent, $C_{p,s}$ [J kg^{-1} K^{-1}]	1877.20	Assumed
Specific heat capacity of gas phase, $C_{p,s}$ [J kg^{-1} K^{-1}]	1010.60	Assumed
Molecular diffusivity, D_m [m^2 s^{-1}]	4.81×10^{-8}	Assumed
Fluid viscosity, μ [kg m^{-1} s^{-1}]	2.15×10^{-5}	Assumed
Effective gas thermal conductivity, K_z [J m^{-1} K^{-1} s^{-1}]	0.09	Assumed
Inside heat transfer coefficient, h_{in} [J m^{-2} K^{-1} s^{-1}]	0	Assumed
Universal gas constant, R [m^3 Pa mol^{-1} K^{-1}]	8.314	Standard value
Operating Parameters		
Syngas feed pressure P_{feed} [bar]	34.5	IGCC conditions
High pressure P_H [bar]	34.5	IGCC conditions
Feed composition (CO_2/H_2), y_{feed} [-]	0.4/0.6	IGCC conditions
Feed temperature, T_{feed} [°C]	240	IGCC conditions

CO_2 recoveries because the CO_2 retained in the column after counter-current blowdown step is pushed out of the column during the purge step. Reversing the counter-current blowdown to a co-current blowdown step in configuration C improved the CO_2 purities significantly. This is because most of the H_2 is removed from the column in the co-current blowdown step and when the column is purged, pure CO_2 is obtained. Configuration C satisfies the regulatory requirements of CO_2 purity-recovery for sequestration. In configuration D, addition of a pressure equalization improved the CO_2 purities. Since the H_2 is removed from the raffinate end of the column at two intermediate pressures, the exit stream in the counter-current blowdown and purge steps are enriched with CO_2, thereby, increasing the CO_2 purities.

It is worth noting that recovering the light product H_2 is important since it is later used as a fuel in the combined cycle of an IGCC power plant. The H_2 purity and recovery for configurations B, C and D are shown in Fig. 4.6. The points correspond to the same operating conditions that represent the CO_2 Pareto curves in Fig. 4.5. The H_2 purity-recovery is not shown for the basic 4-step cycle as the configuration is found to be not suited for use. While designing the PSA process, although the primary objective is maximize the CO_2 purities and CO_2 recoveries, H_2

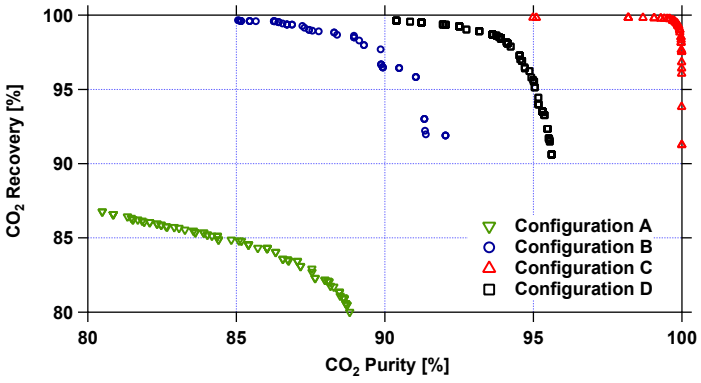

Figure 4.5: CO_2 Purity-Recovery Pareto fronts for four different PSA cycles.

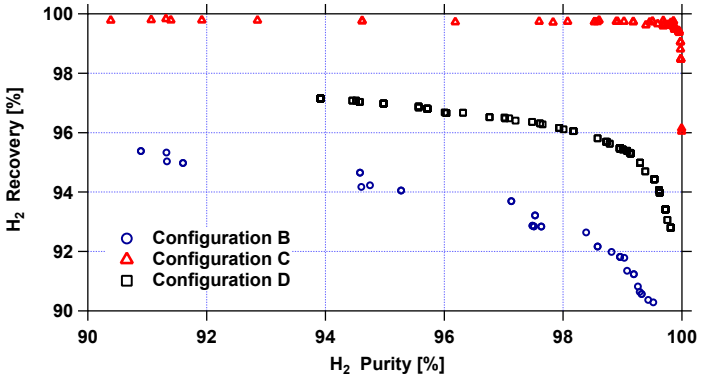

Figure 4.6: H_2 Purity-Recovery points for configurations B, C, and D.

recovery is also considered by evaluating the performance. As shown in Fig. 4.6, H_2 recovery is low for configuration B when compared to configurations C and D. The CO_2 purities for configuration were limited to 92% and it is reflected in H_2 recoveries as the H_2 corresponding to the remaining 8% is slipped through the CO_2 extract stream. Configuration C showed to recover more H_2 than configuration D because the co-current blowdown step in configuration C recovers the residual H_2 in the column.

The low pressures to which the PSA process reaches while obtaining the desired CO_2 purity-recovery has a significant impact while considering the CO_2 for sequestration. In order to understand the pressure swing the cycle undergoes to obtain Pareto points, low pressure P_L is plotted against the CO_2 purity for configurations B, C and D (as shown in Fig. 4.7). For configuration B, the low pressure P_L hits the lowest bound 1 bar. The highest low pressure for which the desired CO_2 purity-recovery are met is 4.3 bar. The low pressures for configuration C and D are mostly crowded between 3 bar and 4 bar, suggesting that CO_2 purity-recovery targets can be met when the low pressure is in that range.

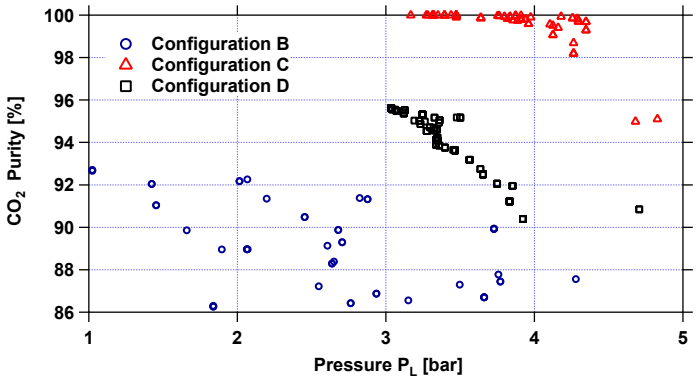

Figure 4.7: CO_2 purities from Pareto fronts for configurations B, C and D plotted against corresponding low pressures P_L.

4.6.2 Analysis of electrical power consumption for PSA

In this section, an individual analysis for CO_2 compression and steam consumption is made in order to understand the influence of each component on the objective function (Eq. 4.33a) before performing a full-scale optimization. For the energy-productivity optimization problem, low pressure P_L has a direct impact on the magnitude of CO_2 compression, while P_L along with other decision variables influence the steam consumption.

CO_2 compression

The CO_2 compression is a common energy consumption for a CO_2 capture unit. This is because the CO_2 capture plants employing any separation techniques have to meet the requirements to deliver the captured CO_2 at supercritical conditions for storage. Hence, it is important to validate the CO_2 compression model discussed in section 4.4.1. The CO_2 compression can be best compared to other cases if its reported in terms of standard units of kWh_e per tonne of CO_2 captured. ψ_{CC} from Eq. 4.14 is used for comparing the different compression energies. The parameters used for calculating ψ_{CC} are shown in Table 4.6. The densities are obtained from NIST Refprop v9 [53]. As long as the compression power is compared in terms of ψ_{CC}, an arbitrary number n_p can be chosen for CO_2 product stream molar flow rate. Two different cases are considered are described below.

Case 1

Case 1 corresponds to an E-gas^{TM} IGCC power plant with dual selexol process [54]. The case considered involves compression of CO_2 product stream from 10 bar to 150 bar using a multi-stage compression with intercoolers. The CO_2 purity in the product stream is 99%. Based on this information, ψ_{CC} is calculated.

Table 4.6: Parameters used for CO_2 compression analysis.

Parameter	Value
n_{p}, [kmol s^{-1}]	2.00
R, [J mol^{-1} K^{-1}]	8.314
T_{ref}, [K]	298.15
γ, [-]	1.28
η_{adia}, [-]	0.8
η_{e}, [-]	0.8
r_{p} [-]	3
ρ_{150} [kg m^{-3}]	855.14
ρ_{72}, [s]	705.44
η_{pump}, [-]	0.75

Table 4.7: Comparison of energy model with different cases.

Case	CO_2 Purity [%]	Energy model [kWh_e $tonne^{-1}$]	E-gas™ IGCC process [kWh_e $tonne^{-1}$]	Riboldi et al. [kWh_e $tonne^{-1}$]
1	99	70.71	68.62	-
2	82	124.49	-	136.13

Case 2

In Case 2, the compression system represents the one reported in Riboldi et al. [55]. For this case, the CO_2 is collected at 1 bar with purity $\approx 82\%$ based on PSA separation. Riboldi et al. further purified the CO_2 stream in the compression unit using double flash separators [55]. The final stream for transportation has a purity of 99% and at pressure 110 bar. The energy model presented in this chapter does not account for purification during compression. Hence, the ψ_{CC} is calculated at 82% and compared with their final purity of 99%.

Table 4.7 shows the comparison of compression power obtained from energy model with E-gas™ IGCC process and Riboldi et al. for CO_2 compression. The energy model predicts ψ_{CC} well when compared to E-gas™ IGCC case, while it predicts 8% lower value than Riboldi et al. One possible reason could be Riboldi et al. uses an extra compressor during the purification process in CO_2 compression unit.

Effect of pressure P_{L} on ψ_{CC}

A parametric study is performed to evaluate the effect of pressure P_{L} on ψ_{CC}. The pressure P_{L} is varied over the operating bounds from 1 bar to 17.3 bar. ψ_{CC} is calculated using Eq. 4.14. Fig. 4.8 shows the effect of pressure P_{L} on ψ_{CC} at different compositions of CO_2 product stream. As expected, the ψ_{CC} decreases with increase in pressure as the work done by the compressor decreases. For a constant pressure P_{L}, ψ_{CC} decreases with increase in purity of CO_2 in the product stream because the stream has more CO_2 in it.

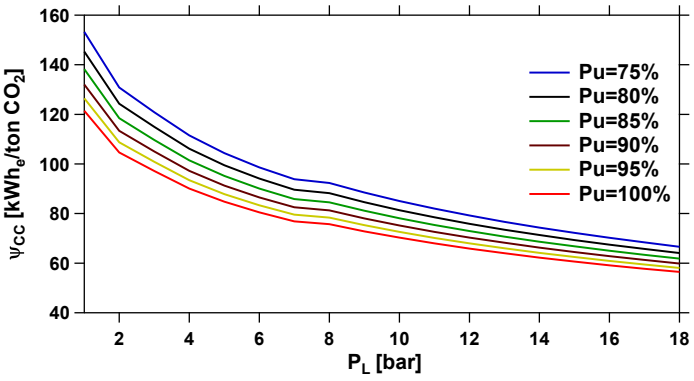

Figure 4.8: Variation of pressure P_{L} and purity $Pu_{\mathrm{CO_2}}$ on ψ_{CC}.

Table 4.8: Arbitrary parameters chosen for obtaining a relation between kg steam consumed per kg CO_2 captured.

Parameter	Value
A, [m^2]	1.00
ϵ, [-]	0.4
v_{PUR}, [m s^{-1}]	1
L, [m]	1
T_{col}, [K]	473.15
T_{steam}, [K]	503.15
q_{s}, [mol m^{-3}]	-19950.57
b, [m^3 mol^{-1}]	3.15×10^{-4}
H, [-]	6.28
t_{R}, [s]	10.43

Steam consumption

The steam consumption estimation is rather a complex calculation. The steam required in the PSA process depends on the operating conditions of a PSA process. However, to understand the effect of only P_{L}, a quick analysis is made using the assumptions from section 4.4.5. Based on Eq. 4.29 and arbitrary parameters in Table 4.8, Fig. 4.9 is developed. It can be seen that the steam consumption increases with increase in P_{L}. This can be attributed to two reasons. Firstly, at higher pressures, more CO_2 has to be extracted from purge which requires more steam. Secondly, at high pressures, steam has high density which increases the mass flow rate of the steam required for purge process.

4.6.3 Minimization of energy and maximization of productivity

The purity-recovery Pareto fronts provide information on the ability of the cycles meeting the regulatory requirements. However, they do not supplement any information regarding the operating costs for the process. The energy consumption and productivity are commonly used to

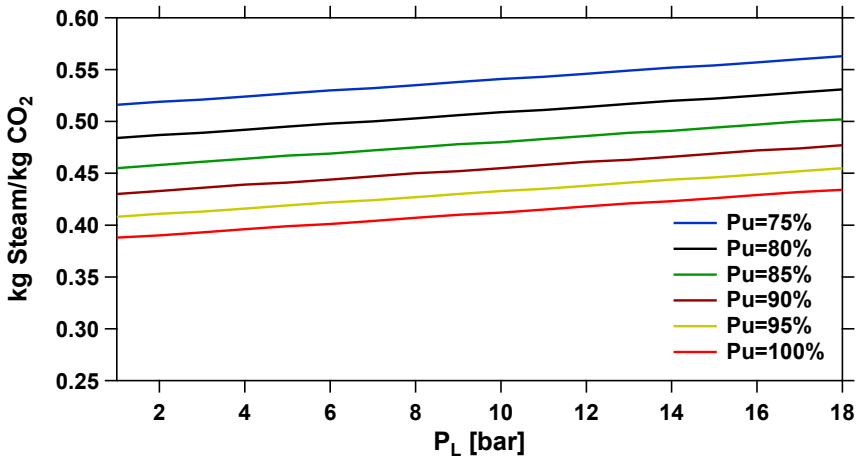

Figure 4.9: Variation of pressure P_{L} and purity $Pu_{\mathrm{CO_2}}$ on $\frac{\text{kg steam}}{\text{kg CO}_2}$.

indirectly represent the operating expenses. The conversion of energy consumption and productivity in terms of cost is rather complex and beyond the scope of this work. For any separation process, it is desired to have least energy consumption and maximum productivity for a given constraints. Hence, the cycles that has met the regulatory requirements for purity-recovery are considered for energy-productivity optimizations. Although, both configurations C and D has met the sequestration targets, configuration C is not considered for this optimization because configuration C involves a co-current blowdown step which removes H_2 from the column at a pressure P_{L}. The H_2 needs to be compressed to pressure P_{H} which requires an additional compressor, thereby increasing the energy penalty. Hence, for this optimization study only 8-step PSA cycle (configuration D) is considered.

A multi-objective optimization was performed under the constraints of CO_2 purity of 95% and CO_2 recovery of 90% respectively, minimizing the objective functions J_3 and J_4 (given by Eq. 4.31 and 4.32). The bounds used for this optimization were kept same as the bounds for purity-recovery optimizations.

The energy-productivity Pareto front obtained from the optimization is shown in Fig. 4.10. All the points in the Pareto curve correspond to the different sets of operating conditions that has met the purity-recovery constraints. It can be seen that the parasitic energy varies from $\approx$ 110 [$\mathrm{kWh_e\ tonne^{-1}}$] for a productivity of $\approx$ 6.1 [$\mathrm{mol\ m^{-3}\ s^{-1}}$] to a maximum of $\approx$ 249 [$\mathrm{kWh_e\ tonne^{-1}}$] for a productivity of $\approx$ 6.74 [$\mathrm{mol\ m^{-3}\ s^{-1}}$]. In order to increase the productivity by $\approx$ 10%, the additional energy penalty will be $\approx$ 140 %. Table 4.9 shows the individual contributions of CO_2 compression and steam consumption to the optimized total power consumption (En). The energy-productivity Pareto front does not represent the best point, but a set of optimal points as it is difficult to reflect the energy-productivity in terms of costs.

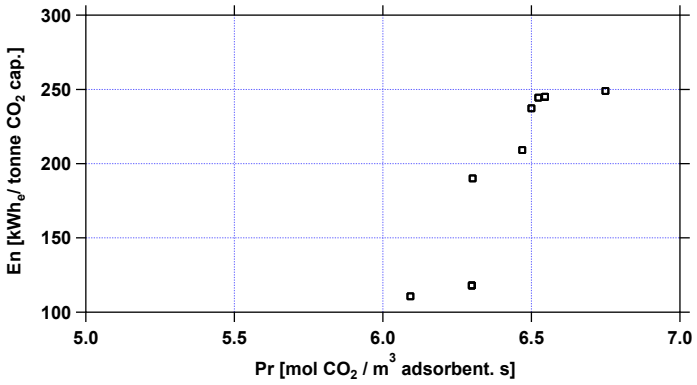

Figure 4.10: Energy-Productivity Pareto front for 8-step PSA cycle.

Table 4.9: CO_2 compression and steam consumption for Pareto points.

Pr [mol.m^{-3}s^{-1}]	**En** [kWh$_e$tonne^{-1}]	ψ_{CC} [kWh$_e$tonne^{-1}]	ψ_{SP} [kWh$_e$tonne^{-1}]
6.34	189.49	83.63	105.86
6.50	208.72	81.02	127.70
6.78	248.31	84.03	164.28
6.53	236.52	84.69	151.83
6.12	110.52	80.01	30.51
6.55	243.84	84.75	159.09
6.33	117.81	84.50	33.32
6.58	244.34	84.48	159.86

4.7 Conclusion

The primary focus of this work was to perform a process optimization for different PSA cycle configurations so as to evaluate their potential for pre-combustion CO_2 capture using TDA AMS-19. The adsorption equilibria for CO_2 on TDA AMS-19 was experimentally measured and fitted to a SIPS isotherm model [34]. H_2 isotherm parameters on activated carbon was obtained from the literature [47]. Four different PSA cycle configurations were considered for this study. A detailed one-dimensional PSA model, modeled using finite volume method, was employed to describe the dynamics of PSA cycles. The full-scale PSA simulations involved solving mass, momentum and energy balances so as to obtain the pressure, temperature and concentration profiles for gases. The performance indicators, namely, purity and recovery for CO_2 were calculated after the process reached the cyclic steady state. An unconstraint multi-objective optimization is performed to maximize the CO_2 purity and recovery for four PSA cycle configurations in order to meet the regulatory requirements of CO_2 purity and recovery of 95% and 90% respectively. Genetic algorithm toolbox in MATLAB is coupled with detailed PSA model. A pre-defined search space is provided to the optimizer to identify the best operating conditions that meet the CO_2 purity-recovery targets. The first PSA cycle configuration studied was basic 4-step cycle.

The PSA cycle did not meet the CO_2 requirements and was found to be infeasible. Addition of pressure equalization and purge step in configuration B improved the CO_2 recoveries, however, the CO_2 purities were limited to 92%. Next, configuration C achieved the targets when the current-counter blowdown in configuration B is reversed. Additional H_2 in co-current blowdown enriched the CO_2 purities. An extra pressure equalization step to configuration B improved the CO_2 purities. Configuration D also met regulatory requirements for CO_2 capture. To determine the parasitic energy for capture unit, a detailed energy modeling is done. CO_2 compression and steam consumption in PSA process found to be majorly contributing to energy consumption. The heat recovered in the system is not accounted for parasitic energy as there is no conversion factor available to represent the heat recovered in terms of electricity. The equivalent electrical power consumption is calculated and compared with different cases. A relationship between the kg steam to be supplied per kg of CO_2 is established and a parametric study is performed on CO_2 compression and steam consumption by changing the low pressure P_L and CO_2 purity. The 8-step PSA cycle was considered for the energy-productivity optimization. The optimal power consumption varied from ≈ 110 to ≈ 249 [kWh_e $tonne^{-1}$].

Part II

Supercritical fluid chromatography

Chapter 5

Computational fluid dynamics study of viscous fingering in supercritical fluid chromatography

5.1 Introduction

Chromatographic techniques are widely employed in the pharmaceutical industry for enantiomer separations [56–58]. Although, traditional high performance liquid chromatography (HPLC) has been in use, supercritical fluid chromatography (SFC) has recently gained attention because of its many advantages [57–59]. In SFC, liquid solvents are replaced with supercritical fluids. The low viscosity and high solute diffusion coefficients of supercritical fluids allow for high operating flow rates with low pressure drops when compared to HPLC [57]. Hence, higher productivities are achieved at the preparative scale. In most SFC applications, supercritical CO_2 is used as the mobile phase solvent. Owing to its low solvation power for polar solutes, often an organic modifier is added to supercritical CO_2 to increase its solvation strength. Modifiers are usually alcohols, such as methanol. The physical properties of mobile phase are altered after addition of modifier. Modifiers competing for adsorption sites has been documented in the literature [60, 61]. The mobile phase with a high content of CO_2 being non-toxic, makes SFC environmentally friendly [57, 59, 62]. After usage, CO_2 can be easily removed by depressurizing the supercritical phase, leaving the modifier behind.

The sample injection plays a vital role in determining the efficiency of the separation. In SFC, the injection of a solute into the mixture of high pressure CO_2 and modifier is difficult. Most practical situations involve the dissolution of solute in the modifier and this solution is injected into the column. There are three different techniques in SFC to inject a sample: mixed-stream injection, modifier-stream injection and extract (X)-injection [63, 64]. The schematic of the two most common types is represented in Fig. 5.1. Mixed-stream injection is the most standard configuration in analytical SFC [65]. In this technique, CO_2 and modifier are mixed upstream of the injection valve. The sample plug (solute + modifier) is injected into the mixed-stream

CO_2 and modifier. Solute precipitation can occur in the column leading to peak distortions [63]. Injection times are shorter in this injection technique because the entire mobile phase passes through the injection valve. The second type of injection is the modifier-stream injection, which is a patented technique [63]. In this type of injection, the mobile phase is mixed downstream of the injection valve i.e. the solute sample is injected in the modifier stream and later, is mixed with the high pressure CO_2. The solute enters the column in same phase as that of mobile phase. The injection times are larger since only modifier stream passes through the injection valve. The injection times, however, depend on the composition of modifier in the mobile phase. This technique is common in preparative SFC. No solute precipitation occurs here [63]. Apart from the mentioned injection techniques, there is a third type, known as Extract (X)-Injection technique [64]. Here, the high pressure CO_2 and modifier is mixed upstream of the injection valve similar to mixed-stream injection. The solute, dissolved in the mobile phase, is injected into the column. In this mode, the solute propagation across the column is in single phase.

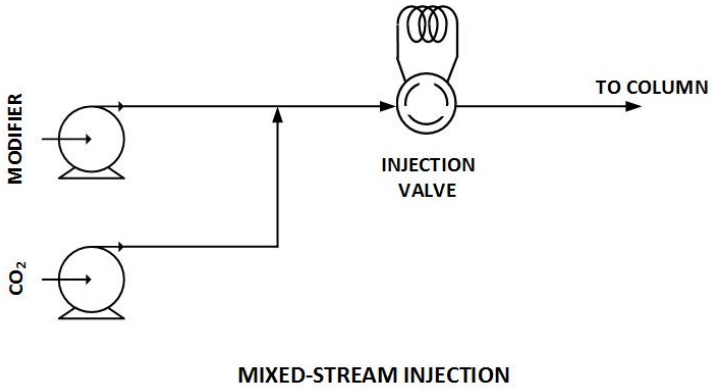

(a)

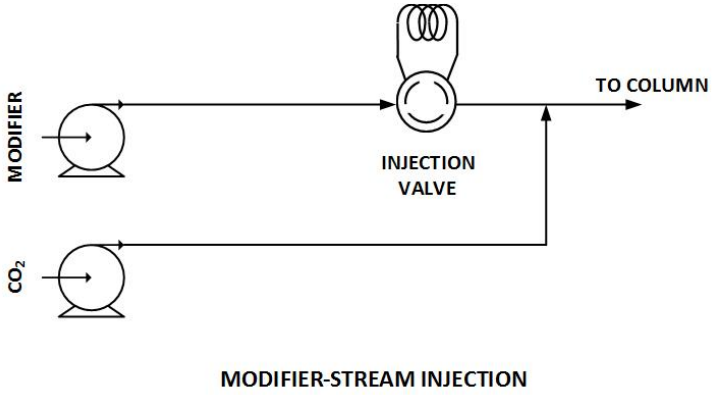

(b)

Figure 5.1: Different types of injection techniques in supercritical fluid chromatography. Adapted from [65].

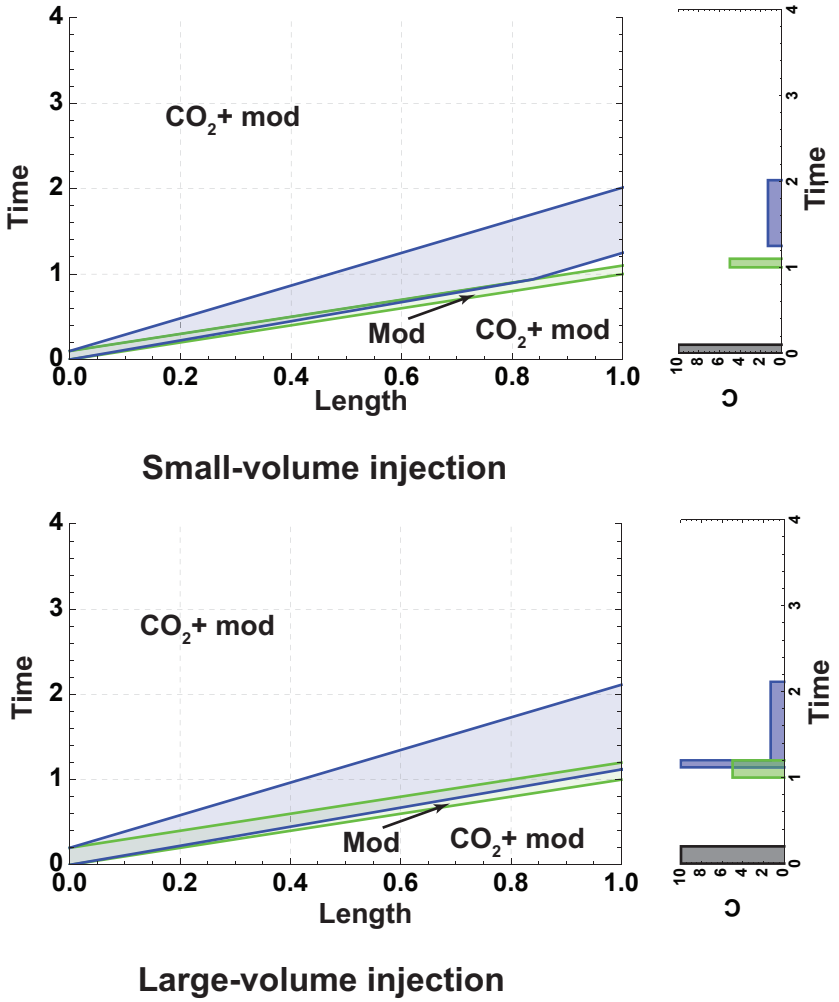

Figure 5.2: Movement of the solute and the modifier band on a physical plane involving mixed stream injection. The green and blue colors indicate the modifier, solute bands respectively and black band indicates the injection. Source: [65].

The retention of solute is influenced by the injection technique. The propagation of chromatographic bands show an interesting behavior, in case of mixed-stream injection. To elaborate this, a scenario is considered where a solute is injected into a mixed-stream environment. For simplicity, CO_2 and modifier do not adsorb. The modifier and the mobile phase traverse through the column unretained. Fig. 5.2 shows the characteristics of solute for a mixed-stream injection. The solute characteristics are developed using the equilibrium theory [66]. While constructing this diagram, no dispersion or mass transfer effects are considered and the solute is always under local equilibrium. The case considered is such that the retention of solute in modifier is less than the retention of solute in the mobile phase. Under these conditions, the solute propagation is under the influence of two different phases. If a large-volume injection is made, then the leading edge of the solute band always propagates and elutes in the modifier plug. The trailing edge under the influence of the mobile phase, traverses slowly due to its high retention behavior in the mobile phase. Because of this, the solute band is broadened, resulting in a long plateau in elution peaks. On the other hand, if a small-volume injection is made, then the leading edge of the solute band comes out of the modifier plug as it traverses across the column, while the trailing edge propagates slowly under the influence of mobile phase. The solute peak disengages itself from the modifier peak. The band broadening behaviors have been reported in the literature [65, 67].

5.1.1 Viscous fingering

In the mixed-stream injection, the mobile phase (CO_2 + modifier) pushes the sample plug (solute + modifier) into the column. Since this type of injection involves the displacement of fluids with viscosity contrasts, it could result in viscous fingering. The magnitude of the viscosity contrast between the sample plug and mobile phase depends on the composition of modifier in the mobile phase. Viscous fingering is a phenomenon arising due to the instabilities at the interface of two fluids of different viscosities percolating through the porous media [68–72]. Due to this phenomenon, low viscous fluid penetrates into high viscous fluid, giving rise to viscous fingers as shown in Fig. 5.3. These fingers are developed either on rear or frontal interface of the sample plug depending on whether the mobile phase displacing the sample plug has low viscosity or high viscosity. The interface where the high viscous fluid displaces the low viscous fluid will remain stable. In most of SFC applications, mobile phase has a low viscosity when compared to the sample plug, leading to development of fingers on rear interface of the sample plug. Viscous fingering is detrimental to chromatographic separations because they distort the band [73–75]. While viscous fingering has been extensively studied in liquid chromatography, its impact on SFC is not well understood. Many modeling efforts have also been reported for a variety of conditions [71]. Experiments performed in the literature report the peak distortions in elution profiles because of viscous fingering [65, 69].

Figure 5.3: Displacement of two miscible fluids with different viscosities in porous media when rear interface is affected by viscous fingering. MeOH (methanol) is the high viscosity plug and CO_2 + MeOH represents the low viscosity mobile phase.

5.1.2 Objective

The objective of this work is to study the dynamics of pulse propagation in supercritical fluid chromatographic columns using an axi-symmetric CFD model implemented into the commercial CFD solver Fluent 16.2 [76]. Two scenarios are considered. The first part describes the dynamics of an unretained plug (no adsorption), while the second part represents the retained plug propagation (with adsorption). In both scenarios, the simulation case replicate experiments from Dai et al. [65]. The experimental system is described in detail in [65, 77].

5.1.3 Background of experimental studies

It is worth recounting the experiments. Two syringe pumps were employed to deliver CO_2 and modifier. A motorized 6-port valve and a UV-Vis detector were used to inject the sample and monitor the elution profiles, respectively. The experiments were carried out with CO_2 flow rate of 1 mL/min. The CO_2 pump head was kept at 4 °C while the oven temperature was maintained at 30 °C for all experiments. Pressure measurements were made at the pump heads and the pressure at the column outlet was held constant at 135 bar using a back-pressure regulator. A long tubing was provided upstream of the injection valve to make sure that the mobile phase reaches the experimental temperature. The experimental conditions were chosen such that the mobile phase was always a single phase fluid. Although, the experiments were carried out for different modifier (methanol) compositions in the mobile phase, for this study, we have only considered a mobile phase with c_{m}= 0.13, where c_{m}, is the methanol mass fraction in the mobile phase.

5.2 Modeling

An axi-symmetric CFD model is developed to describe the dynamics of the pulse propagation in a chromatographic column with following assumptions:

1. Temperature effects are ignored because the experiments were carried out at isothermal conditions.

2. CO_2 and methanol do not adsorb and are completely miscible.

3. Solute does not affect mobile phase bulk properties since the injected concentrations of solute in methanol plug were very negligible [65].

4. Effects arising from the gravity force are assumed to be negligible.

5. The mobile phase, which is a mixture of CO_2 and methanol, is assumed to be an incompressible single-phase fluid.

6. Axi-symmetry.

Before proceeding any further, it is important to discuss the validity of these assumptions. Assumption 1 deals with isothermality and is well satisfied in the experiments. All experiments considered in this study were carried out under conditions where the density drop across the column was small enough that temperature changes due to fluid expansion was minimal. Assumption 2 is reasonable as the extent of CO_2 and methanol, although finite, is negligible compared to those of the solutes. Assumption 3 is also reasonable as the solute was injected in dilute conditions and does not affect the bulk phase properties. Assumption 4 is acceptable since the influence of gravity is small. Assumption 5 which assumes that the fluid is incompressible is perhaps the one that is difficult to satisfy. For the operating conditions considered (both pure CO_2 and mixtures), the range of compressibility factor is 0.257 to 0.334 [53]. The CFD models used in this study are suited for incompressible fluids while the models that account for compressibility effects are available, they are computationally expensive for the phenomena we are interested in describing. The primary goal of this work is to explain many effects that have been observed in SFC. The inclusion of compressibility effects, while important, is outside the scope of this work. Assumption 6 deals with the issue of symmetry. The phenomenon of viscous fingering is known to be asymmetric in nature. However, modeling the column in all the three dimensions was computationally challenging using the resources that were available.

The simulation is carried out using a commercial computational fluid dynamics (CFD) software, ANSYS Fluent 16.2 [76]. The mathematical equations in fluent are solved using a porous media model [78]. The special source terms for species equations are implemented using a user-defined function (UDF). An axi-symmetric geometry with dimensions length 250 mm and radius 2.3 mm is created and a structured fine mesh is chosen such that the space domain is uniformly divided into $2 \cdot 10^5$ quadrilateral control volumes (CV).

5.2.1 Materials & Porous zone properties

Fluid properties

The fluid phase materials used in the simulation are CO_2 and methanol. Supercritical CO_2 properties are loaded in Fluent from NIST Refprop v9.1 database using a user-defined material, while the methanol properties are imported from Fluent database. The densities of both CO_2

and methanol correspond to the densities reported in [65].

The mixture properties like density (ρ_{mix}) and viscosity (μ_{mix}) are calculated as volume-weighted average and mass-weighted average of the species (CO_2 and methanol) respectively [78]. The equations are given below.

$$\rho_{\text{mix}} = \left[\frac{c_{\text{CO}_2}}{\rho_{\text{CO}_2}} + \frac{c_{\text{methanol}}}{\rho_{\text{methanol}}} \right]^{-1} \tag{5.1}$$

where c_{i} and ρ_{i} are the mass fraction and the density for species i=CO_2, methanol, respectively.

$$\mu_{\text{mix}} = c_{\text{CO}_2}\mu_{\text{CO}_2} + c_{\text{methanol}}\mu_{\text{methanol}} \tag{5.2}$$

where μ_{CO_2} and μ_{methanol} are the viscosities of CO_2 and methanol, respectively.

Porous zone properties

The porous matrix is filled with adsorbent particles of diameter d_{p}=5 μm. The bed porosity ϵ_{B}=0.39 is estimated using Darcy's equation for pressure drop Eq. (5.3), based on the pressure measurements from the experiments [65].

$$-\frac{\Delta P_{\text{exp}}}{L} = \frac{150\mu(1-\epsilon_{\text{B}})^2 \vec{v_{\text{s}}}}{\epsilon_{\text{B}}^3 d_{\text{p}}^2} \tag{5.3}$$

L represents the length of the column; ΔP_{exp} is the experimentally measured pressure difference between outlet and inlet of the column, $\vec{v_{\text{s}}}$ is the superficial velocity.

The permeability ($\bar{K}$) of homogenous porous media is calculated using the Carman-Kozeny equation [79].

$$\bar{K} = \frac{\epsilon_{\text{B}}^3 d_{\text{P}}^2}{150(1-\epsilon_{\text{B}})^2} \tag{5.4}$$

The intra-particle porosity (ϵ_{P}) is estimated from the experimentally measured total porosity (ϵ_{T}) using the following expression

$$\epsilon_{\text{T}} = \epsilon_{\text{B}} + (1-\epsilon_{\text{B}})\epsilon_{\text{P}} \tag{5.5}$$

5.2.2 Governing equations

Continuity & Momentum equations

The mass and momentum conservation equations in porous media as given in the Fluent user guide were used [78].

$$\frac{\partial(\epsilon_{\text{B}}\rho)}{\partial t} + \nabla \cdot (\epsilon_{\text{B}}\rho\vec{v}) = 0 \tag{5.6}$$

$$\frac{\partial\left(\epsilon_{\mathrm{B}}\rho\vec{v}\right)}{\partial t}+\nabla\cdot\left(\epsilon_{\mathrm{B}}\rho\vec{v}\vec{v}\right)=-\epsilon_{\mathrm{B}}\nabla P+\nabla\cdot\left(\epsilon_{\mathrm{B}}\vec{\tau}\right)+\epsilon_{\mathrm{B}}\rho\vec{g}+\vec{F} \tag{5.7}$$

The last term (F) in the momentum conservation (Eq. 5.7) represents the viscous and inertial losses in porous media.

$$\vec{F}=-\left(\frac{\epsilon_{\mathrm{B}}^{2}\mu}{\bar{K}}+\frac{\epsilon_{\mathrm{B}}^{3}C_{2}\rho\vec{v}}{2}\right)\vec{v} \tag{5.8}$$

As the flow is laminar, C_2=0.

Transport equations

$$\frac{\partial\left(\epsilon_{\mathrm{B}}\rho c_{\mathrm{i}}\right)}{\partial t}+\nabla\cdot\left(\epsilon_{\mathrm{B}}\rho\vec{v}c_{\mathrm{i}}\right)=\nabla\cdot\left(\epsilon_{\mathrm{B}}\Gamma\nabla c_{\mathrm{i}}\right)+\epsilon_{\mathrm{B}}S_{\mathrm{i}} \tag{5.9}$$

$$\frac{\partial\left(\epsilon_{\mathrm{B}}\rho c_{\mathrm{s,i}}\right)}{\partial t}+\nabla\cdot\left(\epsilon_{\mathrm{B}}\rho\vec{v}c_{\mathrm{s,i}}\right)=\nabla\cdot\left(\epsilon_{\mathrm{B}}\Gamma_{\mathrm{s}}\nabla c_{\mathrm{s,i}}\right)-\left(1-\epsilon_{\mathrm{B}}\right)\frac{\partial\left(\rho\bar{q}_{\mathrm{s,i}}\right)}{\partial t} \tag{5.10}$$

where c_{i}, $c_{\mathrm{s,i}}$ represents the fluid phase mass fractions of solvent and solute species while $\bar{q}_{\mathrm{s,i}}$ is the dimensionless solid phase concentration of the solute species i. Γ, Γ_{s} are the isotropic diffusivities for the solvent and solute, respectively and are given by,

$$\Gamma=\rho D \tag{5.11}$$

$$\Gamma_{\mathrm{s}}=\rho D_{\mathrm{s}} \tag{5.12}$$

D, D_{s} are the dispersion constants ($\mathrm{m}^{-2}\ \mathrm{s}^{-1}$) of the solvent and solute, respectively.

Solvent transport equations are solved using standard species transport model, while the solute fluid phase transport equations are solved by loading user-defined scalar equations into Fluent.

A source term S_{i} is added to solvent transport equation (Eq. 5.9) to account for accumulation of solvent on the solid.

$$S_{\mathrm{i}}=-\frac{\left(1-\epsilon_{\mathrm{B}}\right)\epsilon_{\mathrm{P}}}{\epsilon_{\mathrm{B}}}\frac{\partial c_{\mathrm{i}}}{\partial t} \tag{5.13}$$

where ϵ_P is the particle porosity.

Linear driving force model

Although, the influence of mass transfer is negligible because of the size of particles used in this system (5μm), in addition to, high diffusion coefficients of supercritical fluids, a linear driving force model is employed to describe the mass transfer effects.

$$\frac{\partial\bar{q}_{\mathrm{s,i}}}{\partial t}=\bar{k}(\bar{q}_{\mathrm{s,i}}^{*}-\bar{q}_{\mathrm{s,i}}) \tag{5.14}$$

where $\bar{q}^*_{\mathrm{s,i}}$ is the equilibrium dimensionless solid phase concentration of the solute component i. A sufficiently high value of $\bar{k}$=10 s^{-1} was chosen.

Retention Characteristics

The retention mechanism for the solute flurbiprofen was experimentally determined in an earlier publication [65]. The experiments involved injection of 2 μL of a dilute solution of racemic flurbiprofen at different modifier compositions and corresponding measurements of retention time. The adsorption behavior of racemic flurbiprofen was quantified in terms of an Henry constant. The Henry constant H_{i} of component i defined as

$$\bar{q}^*_{\mathrm{s,i}} = H_{\mathrm{i}} c_{\mathrm{s,i}} \tag{5.15}$$

where $q^*_{\mathrm{s,i}}$ and $c_{\mathrm{s,i}}$ are equilibrium solid phase and fluid phase concentrations of the solute component i. From the measured retention times ($t_{\mathrm{R,i}}$), Henry constant is calculated using the following equation

$$t_{\mathrm{R,i}} = \frac{L}{v}\left(1 + \frac{1-\epsilon_{\mathrm{B}}}{\epsilon_{\mathrm{B}}} H_{\mathrm{i}}\right) \tag{5.16}$$

where L and v are the length of the column and interstitial fluid velocity, respectively.

It is worth noting that in SFC, the retention of the solute is dependent on the density of the fluid phase [77]. There are literature studies which show the effects of both the density of the mobile phase and modifier composition on the Henry constant [80]. For the given system, experimental observations showed a rise in pressure at the inlet during the injection of solute [65]. The density of mobile phase entering the column, after the pulse injection of solute, increases due to the increase in pressure at the inlet. Therefore, the effect of mobile phase density on retention of solute has to be considered. A new correlation is formulated to account for the dependence of Henry constant on the mobile phase density and modifier composition. Effect of mobile phase density is quantified in terms of pressure as it can be incorporated into the simulations in a rather straightforward manner. The experimental retention times were measured at an average pressure of 143 bar [65]. Another set of experimental retention times of solute were obtained from a previous study corresponding to an average pressure of 180 bar [77]. Suitable dead volume corrections are made in determining the Henry constants for the enantiomers. Based on the retention information at these pressures, the following equations describe the dependence.

$$H_{\mathrm{R}} = 0.888 c_{\mathrm{m}}^{0.0014P-0.743} \tag{5.17}$$

$$H_{\mathrm{S}} = 1.083 c_{\mathrm{m}}^{0.0013P-0.948} \tag{5.18}$$

where c_{m} is the methanol mass fraction [-] and P is the pressure in the column [bar]. Fig. 5.4 shows the dependence of Henry constant on the modifier composition and pressure. The Henry

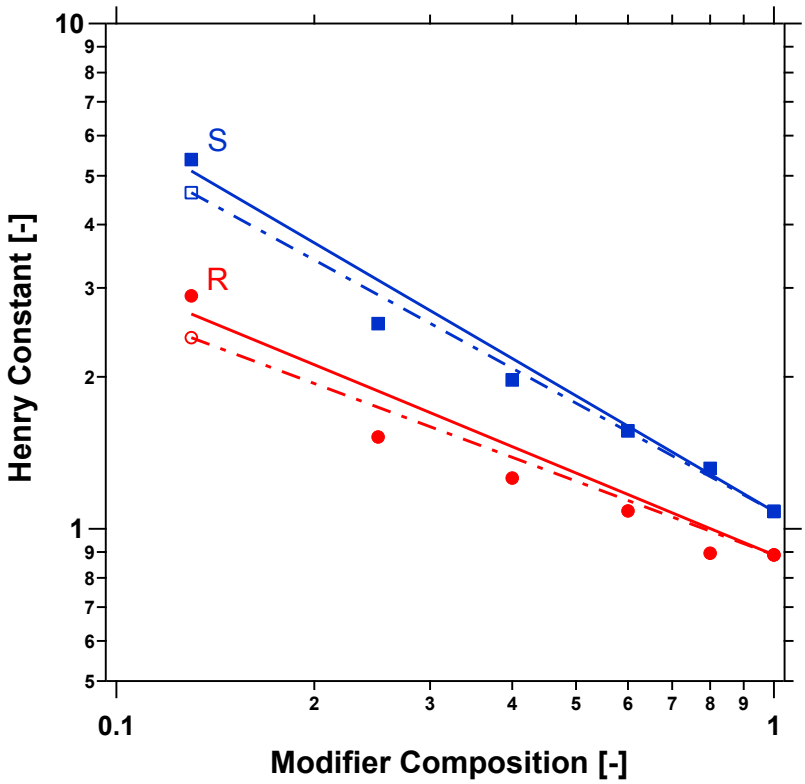

Figure 5.4: Experimentally measured (symbols) and calculated (lines) Henry constants of R- and S-Flurbiprofen. Solid symbols represent experimental data at 143 bar and open symbols correspond to 180 bar. Solid lines represent fitted Henry constants at 143 bar and dashed lines represent Henry constants at 180 bar.

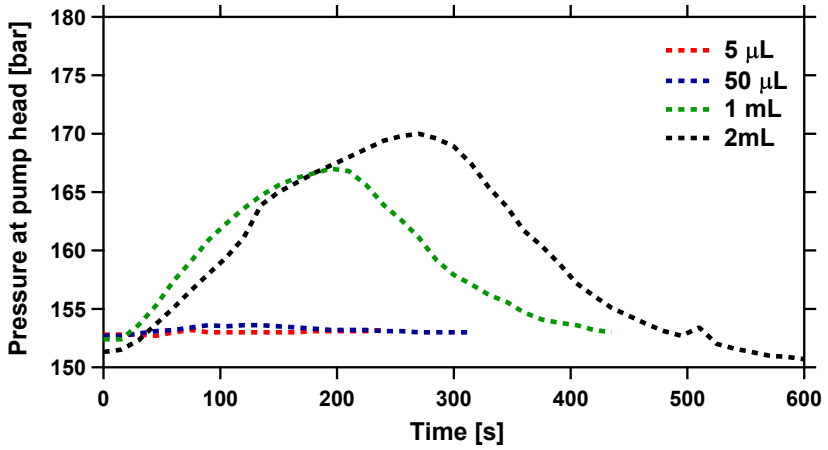

Figure 5.5: Experimentally measured pressures at the CO_2 pump head for different volume injections.

constant decreases with increase in both the modifier composition and pressure. Eq. (5.17) and (5.18) are formulated such that the calculated Henry constant passes through the experimental point at a modifier concentration c_m =1. This is done because it is assumed that the methanol is incompressible and Henry constant of solute in methanol has to be same at different pressures. It is to be noted that the system under study deals with pressures varying from 135 bar to 180 bar. The correlation extrapolates for pressures 135 bar to 143 bar to describe the retention of the solute.

5.2.3 Initial & boundary conditions

For all the simulations, the column is initially filled with a mobile phase (c_m=0.13). A pulse injection of tracer or solute in a stream of methanol (c_m=1) is made at time t=0.

The boundary conditions used for this simulation are velocity inlet and pressure outlet. The experiments were performed such that the pressure at the outlet was maintained at 135 bar using a pressure regulator. Hence, pressure at outlet is maintained at 135 bar for all simulations. No slip condition is used for the wall.

Pressure-adjusted velocity boundary condition

The large-volume injections (1 mL and 2 mL) from the experiments showed a rise in the pressure at the inlet because of injection of a high viscosity plug into the column (shown in Fig. 5.5). The high inlet pressures will introduce compressibility into the system and the assumption of incompressible fluid will no longer be valid. To negate the effect of compressibility, an adjusted injection velocity is implemented instead of experimental injection velocity during the pulse injection. This calculation is performed based on Darcy's law:

$$\frac{\Delta P_{\text{initial}}}{\Delta P_{\text{LV}}} = \frac{\vec{v}_{\text{adj}}}{\vec{v_{\text{s}}}} \tag{5.19}$$

where ΔP_{LV} is the difference between outlet pressure and integral averaged pressure at the inlet during injection; $\Delta P_{\text{initial}}$ is the difference between outlet pressure and inlet pressure at time t=0. $\vec{v}_{\text{adj}}$, $\vec{v_{\text{s}}}$ are the adjusted and experimental superficial injection velocities. ΔP_{LV} & $\Delta P_{\text{initial}}$ are obtained by running a simulation with experimental injection velocity $\vec{v_{\text{s}}}$. Implementation of an adjusted injection velocity explains the delay in elution times for large-volume injections. Dai et al. used a similar approach to explain the delay in elution times for large-volume injections. In case of small-volume injections, since there is negligible pressure increase at the inlet, no pressure corrected adjusted velocity is implemented.

5.2.4 Numerical scheme

In this study, axi-symmetric Navier-Stokes equations coupled with species conservation equations are solved using control-volume methods available in ANSYS Fluent 16.2. The pressure-based solver is used since the system involves low velocity incompressible flows. In this solver type, the governing equations are solved sequentially. The solver solves momentum and continuity equations first and then solves for transport and user-defined scalar equations. A SIMPLE (Semi-Implicit Method for Pressure-Linked Equations) algorithm is used for pressure-velocity coupling to ensure mass conservation [43]. For spatial discretization, a 3rd order MUSCL scheme is used. Using this scheme is required to minimize the numerical diffusion and skip the numerical instabilities which could affect the spatial accuracy in simulations [76]. Time derivatives are discretized using first order implicit scheme. The advantage of using implicit method is it is unconditionally stable with respect to time. The time step used for all simulations is 0.02 s, leading to the Courant-Friedrichs-Lewy (CFL) number less than unity. The iterations are stopped when the scaled residuals for continuity and momentum equations are less than 1×10^{-5}, while transport and used-defined scalar equations are stopped when scaled residuals are less than 1×10^{-10}. The simulations are performed using 16 cores Intel Xeon (R) 3.1 GHz machine.

5.3 Results & Discussion

5.3.1 Dynamics of an unretained plug

The first set of simulations represent the tracer experiments reported earlier [65]. The experiments involved injection of different volumes of a very dilute solution of tri-tert-butylbenzene (TTBB) tracer into the mobile phase. Assuming TTBB is non-adsorbed, the dynamics of TTBB can be treated as an indication of the propagation of the methanol plug. Fig. 5.6 shows the dynamics of methanol plug at different times in case of small-volume injections, 5μL and 50 μL. The propagation is from left to right. The propagation of methanol is predicted using its local fluid phase composition $c_{\text{i}}(x, y, t)$ from Eq. (5.10). For 50 μL volume injection (as shown in Fig. 5.6(b)), the mobile phase, being a low viscous fluid, penetrates into the high viscous methanol

Table 5.1: Physical properties & simulation parameters.

Parameter	Value
Column Properties	
Length, L [cm]	25
Diameter, d [cm]	0.46
Bed voidage, ϵ_B [-]	0.39
Particle size, d_p [μm]	5
Particle voidage, ϵ_p [-]	0.615
Physical Properties	
Density of supercritical CO_2, ρ_{CO_2} [kg m^{-3}]	900.56
Density of methanol, ρ_{MeOH} [kg m^{-3}]	790.53
Viscosity of supercritical CO_2, μ_{CO_2} [cP]	0.08
Viscosity of methanol, μ_{MeOH} [cP]	0.55
Overall dispersion coefficient for solvent species, D [m^2 s^{-1}]	4.5×10^{-9}
Overall dispersion coefficient for solute, D_s [m^2 s^{-1}]	5×10^{-9}
Mass transfer coefficient, $\bar{k}$ [s^{-1}]	10
Operating Parameters	
Superficial velocity, v_s [cm s^{-1}]	0.128
Outlet pressure, P_{out} [bar]	135
Temperature, T [°C]	30

plug due to the hydrodynamic instabilities at the rear interface. The frontal interface of the methanol plug remains stable. Since, the width of injection is small in this case, the fingers propagate till the frontal interface of the methanol plug. The entire methanol plug under the influence of viscous fingering, dilutes in the mobile phase over time and propagates as a dispersed pattern. The dispersion due to viscous fingering, drags the width of methanol plug along the column, leading to band broadening of methanol as it traverses along the column. For a 5 μL injection, since the width of injection is very small, the effect of viscous fingering is observed early in the column and the fingers mix with the mobile phase and propagate as a dispersed plug.

Fig. 5.7 shows the dynamics of methanol plug at different times for large-volume injections, namely, 1 mL and 2 mL. As mentioned in the modeling section, an adjusted injection velocity boundary condition is implemented to account for pressure increase at the inlet. For a 1 mL injection, the adjusted velocity is calculated to be 0.63 times that of experimental injection velocity, while for a 2 mL injection, the same is found out to be 0.44 times that of experimental injection velocity. The simulation is performed such that an adjusted injection velocity is switched to experimental injection velocity, after time of injection. As expected, the rear interface of methanol plug is affected by viscous fingering while the frontal interface remains stable as it traverses along the column. It can be observed that the methanol plug propagates in two regions. One, the region where the methanol plug is unaffected by viscous fingering phenomenon

(a) 5 μL volume injection

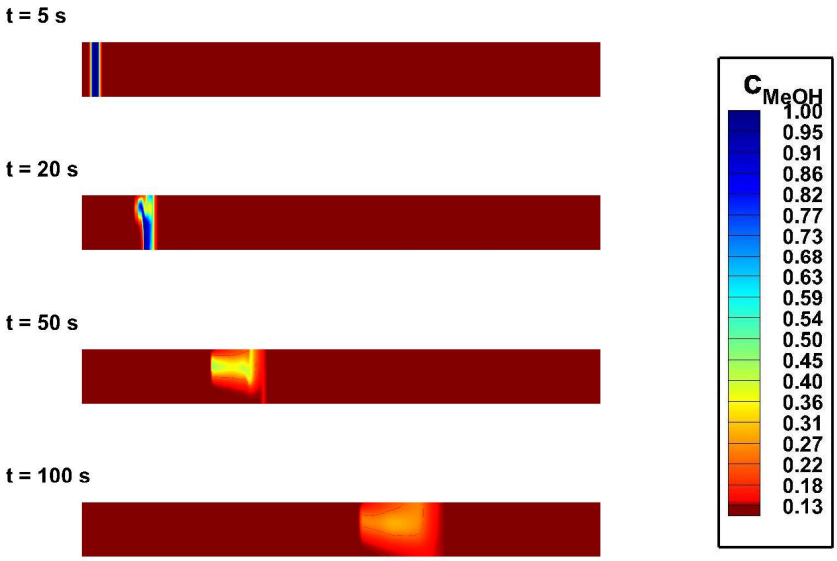

(b) 50 μL volume injection

Figure 5.6: Evolution of local methanol concentration $c(x, y, t)$ at different times for cases (a) 5 μL injection (b) 50 μL injection. The propagation is from left to right.

and the other, is the region under the influence of the fingers. The leading edge of the methanol plug elutes as viscous fingers propagate through the rear portion of the plug. Band broadening

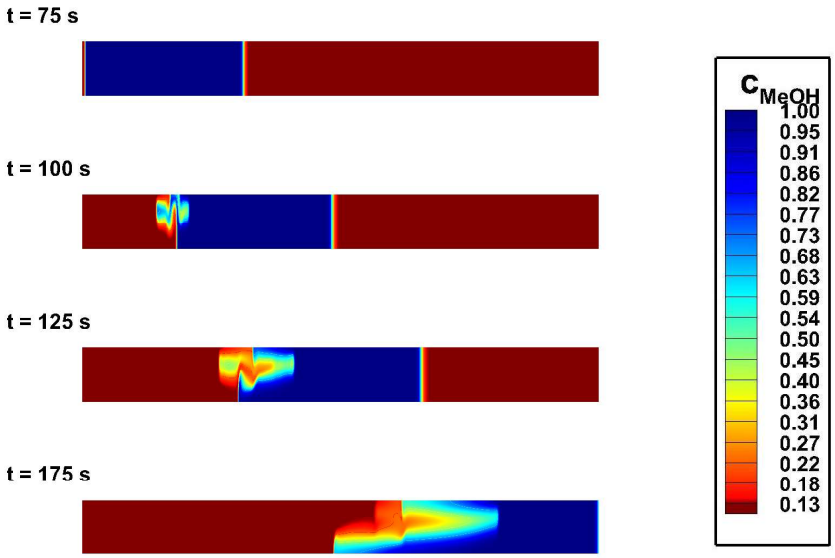

(a) 1 mL volume injection

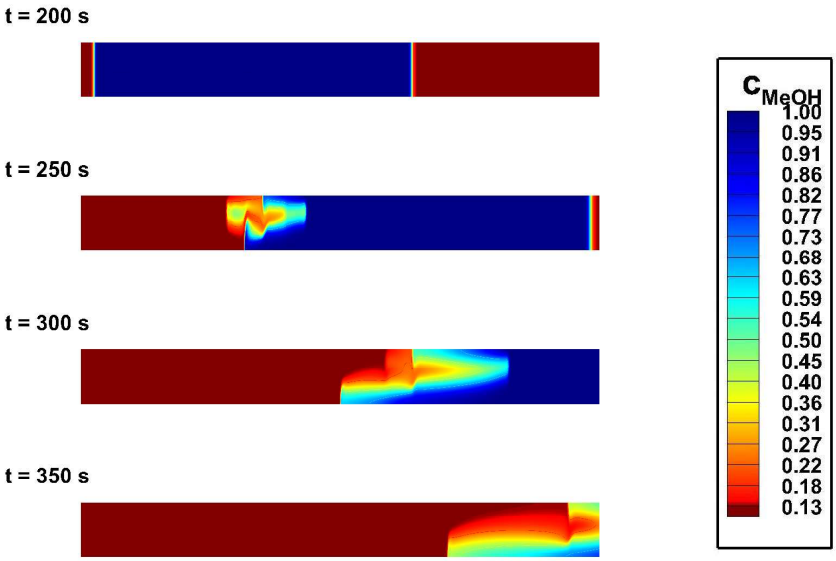

(b) 2 mL volume injection

Figure 5.7: Evolution of local methanol concentration $c(x, y, t)$ at different times for cases (a) 1 mL injection (b) 2 mL injection. The propagation is from left to right.

occurs due to dispersion of the rear portion of methanol plug under the influence of viscous fingering.

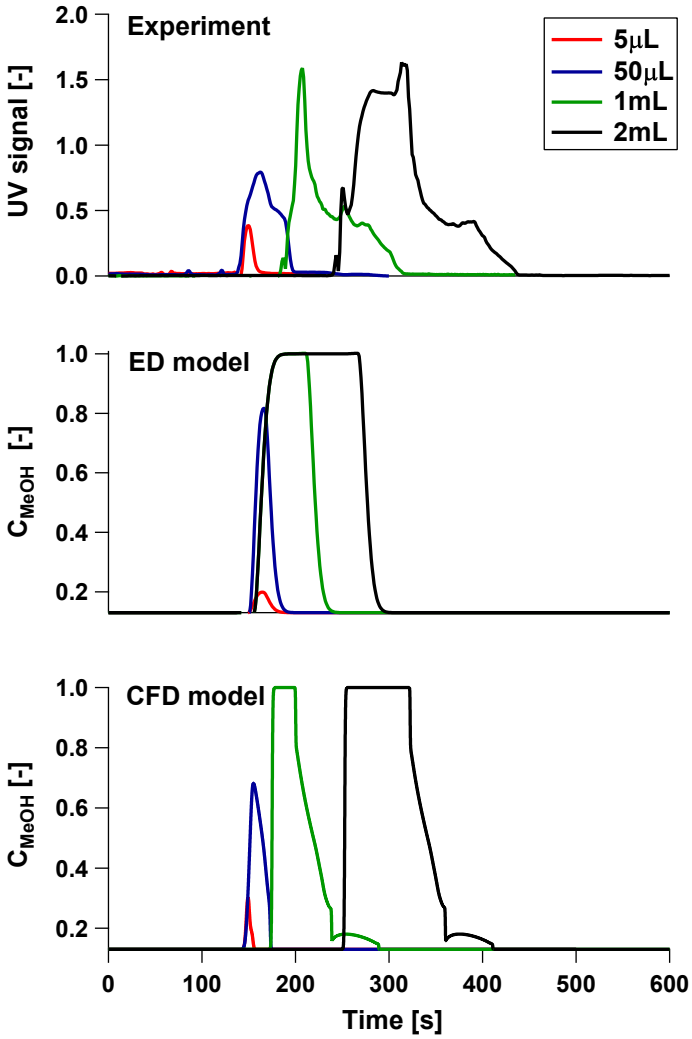

Figure 5.8: CFD simulated elution peaks of methanol in comparison to that of experiments. Note that the 5μL and 50 μL experimental peaks are magnified 10 times while the simulated peaks are magnified 5 times for visualization.

The simulations are performed for 4 different volume injections, i.e. 5 μL, 50 μL, 1 mL and 2 mL. The eluent concentration is represented in terms of a mass-weighted cross sectional average of methanol mass fraction c at the outlet. In Fig. 5.8, the elution profiles for these simulations and experimental elution peaks are compared. The elution profiles calculated from equilibrium-dispersive (ED) model in [65] are also compared with the CFD model. Due to difficulties in calibrating UV absorbance for these experiments, UV readings are not converted to concentration units and were used as-is from experimental measurements. A long tail is observed in elution peaks for 50 μL, 1 mL and 2 mL injections because of the dispersed pattern of the methanol plug propagating under the influence of viscous fingering. The CFD model clearly predicts the delay in elution that is observed in the experiments but absent in the ED calculations. The model also predicts, qualitatively, the peak distortions observed in the trailing edge of the elution profile arising due to viscous fingering.

5.3.2 Dynamics of a retained plug

In this section, adsorption effects are considered in addition to the hydrodynamic effect that was described in the previous section. The simulations represent experiments involving different volume injections of a racemic mixture of R-Flurbiprofen and S-Flurbiprofen in a mixed-stream mobile phase [65]. Dispersion coefficient for solute (D_s) was estimated by fitting the simulated elution peaks of the smallest volume injection (5 μL) to the experiments. The physical properties and simulation parameters used are given in Table 5.1.

For large-volume injections (1 mL and 2 mL), experiments showed a rise in pressure at the CO_2 pump head. As mentioned earlier, this is due to the injection of high viscosity plug into the column. The simulations also showed rise in pressure at the inlet. Increase in pressure caused delay in elution times, because of compressibility in the system. Since the simulation assumes fluid incompressibility, adjusted injection velocity is implemented, as described in modeling section, to indirectly account for the effect of fluid compressibility.

The simulated propagation of R-Flurbiprofen and S-Flurbiprofen enantiomers, inside the column is shown in Fig. 5.9 and 5.10, respectively. The leading edge of the solute will be in methanol while the trailing edge coincides with the interface of mobile phase. The trailing edge of the solute under the influence of mobile phase slowly disengages itself from the methanol plug, due to high retention in mobile phase when compared to methanol. This equilibrium effect causes distortion (creation of a long plateau) of solute band by dragging the rear portion of solute band into mobile phase. Many interesting phenomena can be observed. Firstly, for large-volume injections (as shown in Fig. 5.9(c), 5.9(d) and 5.10(d)), a part of the solute band elutes under the distorted methanol band. For these cases, it can be clearly seen that the solute band is also distorted. The distortion in the solute band occurs due to the influence of viscous fingering,

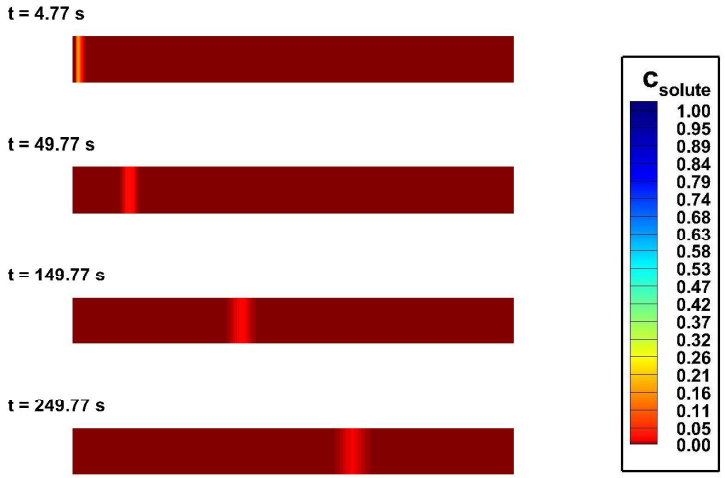

(a) 5 μL volume injection

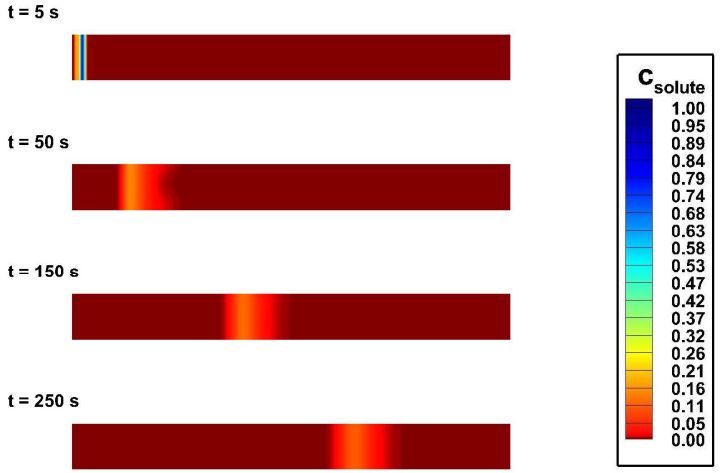

(b) 50 μL volume injection

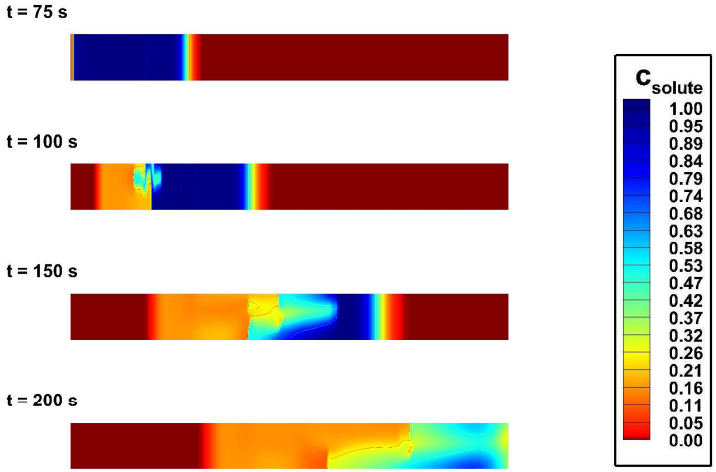

(c) 1 mL volume injection

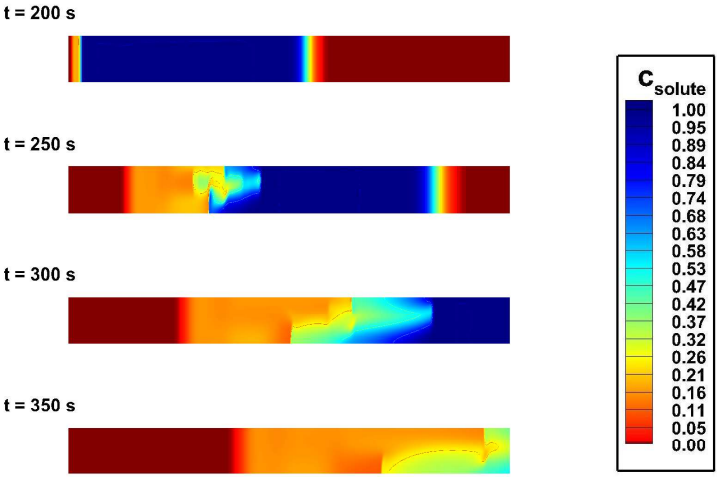

(d) 2 mL volume injection

Figure 5.9: Evolution of local R-Flurbiprofen concentration $c_s(x, y, t)$ at different times for cases (a) 5 μL injection (b) 50 μL injection (c) 1 mL injection (d) 2 mL injection. The propagation is from left to right.

(a) 5 μL volume injection

(b) 50 μL volume injection

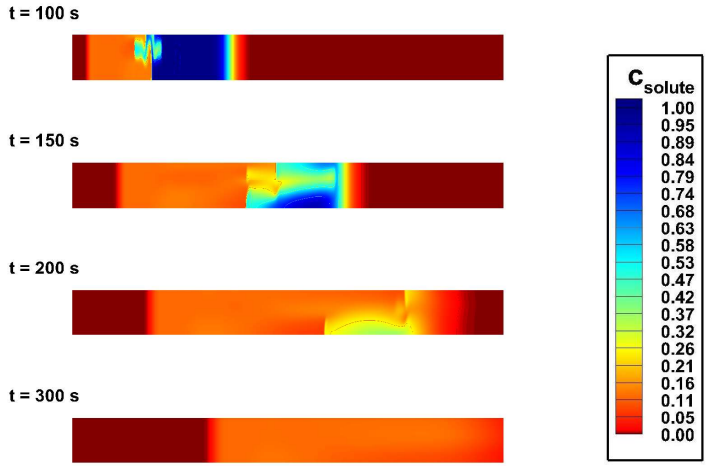

(c) 1 mL volume injection

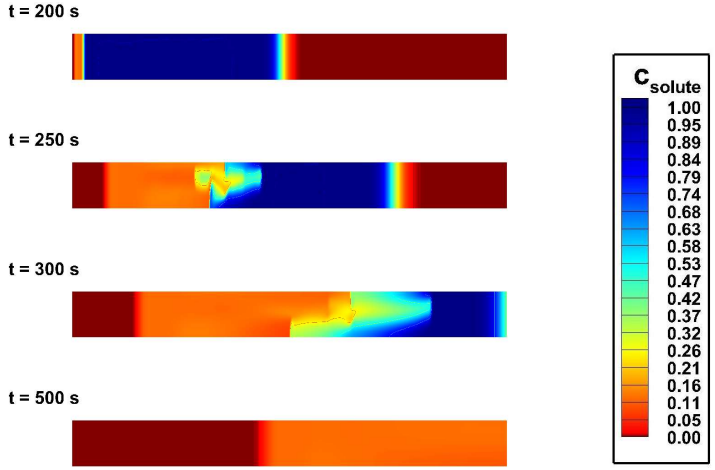

(d) 2 mL volume injection

Figure 5.10: Evolution of local S-Flurbiprofen concentration $c_s(x, y, t)$ at different times for cases (a) 5 μL injection (b) 50 μL injection (c) 1 mL injection (d) 2 mL injection. The propagation is from left to right.

while the equilibrium effect is responsible for dragging the rear portion of the solute band in the mixed-phase environment along the column. Second, there are also situations where the solute band is present within the modifier band when viscous fingering develops but owing to the stronger retention, the solute has disengaged from the modifier band. However, the remanants of the distortion continue to propagate along the column. This is clearly seen in Fig. 5.10(c). Finally compared to the case of ED simulations, in addition to capturing the distortion effects, the pressure-adjusted velocity boundary condition also captures the delayed elution of the profiles. Fig. 5.11 shows the qualitative comparison of experimental elution profiles of both enantiomers to that of calculated elution peaks from ED and CFD models. The eluent concentration from the CFD simulations is represented in terms of a mass-weighted cross sectional average of solute mass fraction c_s at the outlet. Due to difficulties in calibrating UV absorbance for these experiments, UV readings are not converted to concentration units and were used as they were obtained from experiments. R-Flurbiprofen, for large-volume injections, elutes in two different environments: methanol (c_m=1) and mobile phase (c_m=0.13). Hence, a sharp rise in the elution profile followed by a long plateau is noticed. 2 mL injection of S-Flurbiprofen also show the same behavior. The CFD simulations results make a good qualitative match with the experiments. It is worth considering that Dai et al. reported reproducibility issues for large-volume injections [65].

Another interesting phenomenon noticed in the experiments were the peak fronting effect for S-Flurbiprofen, particularly for the 1 mL injection. The simulation also predicts similar peak fronting behavior for the solute. The cause of this behavior is because the solute band spends more time disengaging itself from the methanol band, leading to band broadening [65]. The modifier composition will vary from c_m=0.13 to c_m=1, making the band to disperse. To elaborate this, the retention of solute, a modifier composition dependent, propagates with different characteristic velocities in this region, thereby causing the spreading [65]. The band broadening effect is more significant in case of 1 mL injections. While the influence of different retention behavior dominates the solute band propagation, viscous fingering also plays a significant role in affecting the propagation. The solute band interacts with methanol band in the region under the influence of viscous fingering. Because of this, the peak fronting is distorted in simulations, similar to that observed from the experiments. The evolution of S-Flurbiprofen 1 mL injection at different times inside the column is shown in Fig. 5.10(c). Fig. 5.12 shows the magnified portion of the plateau in S-Flurbiprofen elution profile. In theory, a flat long plateau is expected in the elution, but, due to the solute interactions with viscous fingers, it can be seen that the plateau is distorted and matches well (qualitatively) with the experiments. The peak fronting effect for R-Flurbiprofen is less significant than S-Flurbiprofen in case of 1mL because R-Flurbiprofen solute comes out of the methanol plug faster than S-Flurbiprofen. For small-volume injections, the solute band completely disengages itself from methanol band before viscous fingering phenomena influences methanol plug. Later, the solute band propagates in the mixed-phase.

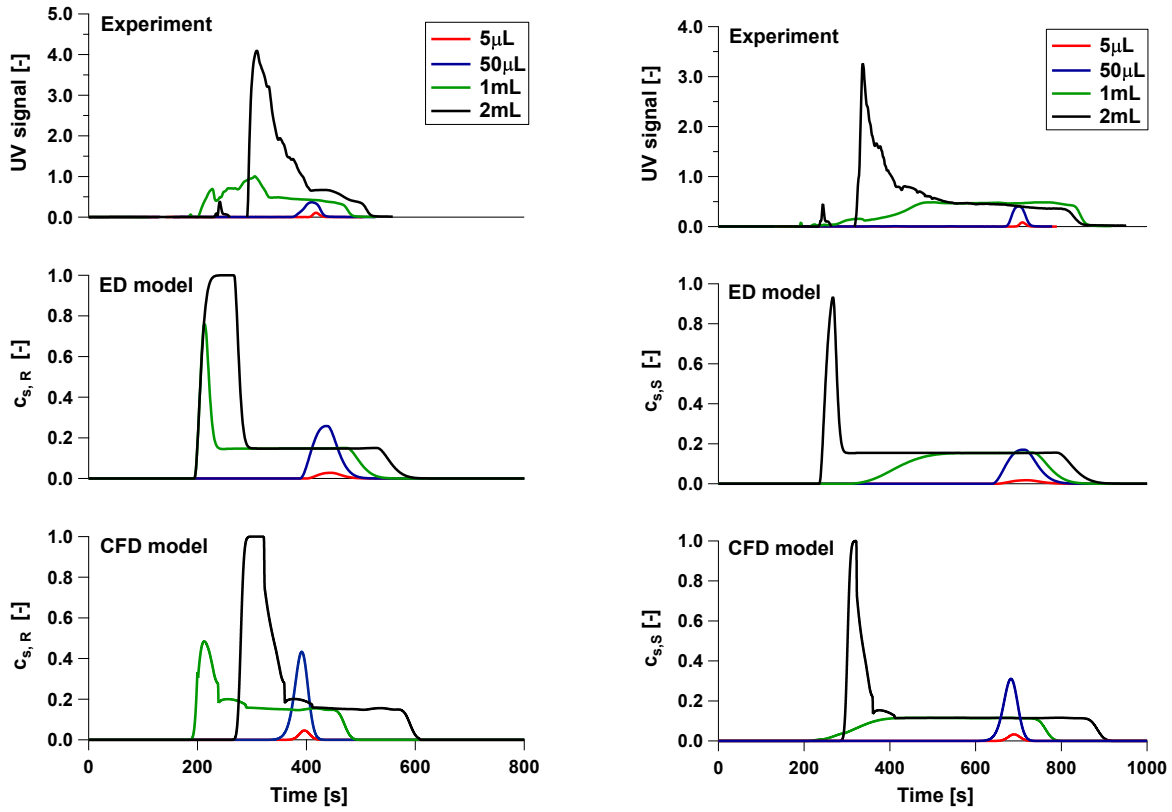

Figure 5.11: CFD simulated elution peaks in comparison to that of experiments and ED simulations for different volume mixed-stream injections corresponding to (a) R-Flurbiprofen (b) S-Flurbiprofen. Note that the 5μL and 50 μL experimental peaks are magnified 10 times while the simulated peaks are magnified 5 times for visualization.

5.3.3 Influence of viscous fingering on a small-volume injection

Both experiments and simulation showed peak broadening in case of small-volume injections. A case study is performed to analyze the influence of viscous fingering for a solute injected in small-volumes. Three cases are considered with R-Flurbiprofen as solute. In Case 1, a simulation is performed, similar to earlier section, where the propagation of R-Flurbiprofen is captured for a 50 μL injection. The simulation took into account of both viscous fingering and equilibrium effects. The elution peak of R-Flurbiprofen for this simulation is shown in Fig. 5.13 (blue line). In another simulation Case 2, viscous fingering effect is decoupled by making the viscosity of the mixture constant, instead of concentration dependent. The elution peak of R-Flurbiprofen in this case, coincides exactly on the elution peak of Case 1. It is worth noting that the solute band disengages from methanol band very early in the column, because of small-volume injection. In Case 2, the solute band will be under the influence of equilibrium effect, similar to Case 1,

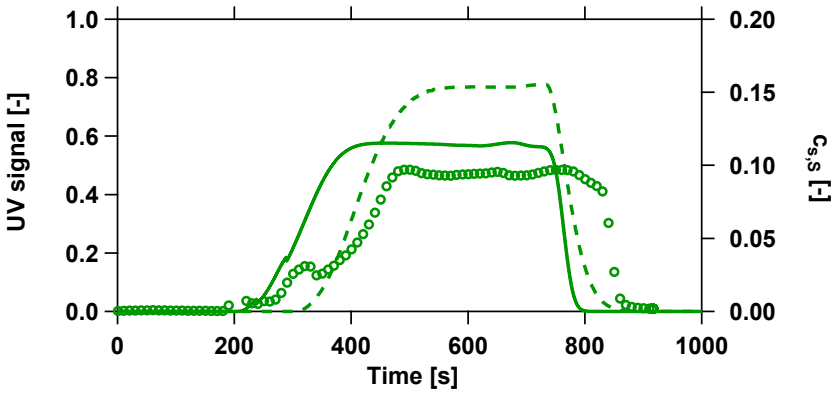

Figure 5.12: Elution profile of solute S-Flurbiprofen, for 1 mL injection. CFD simulated elution peak (solid line) compared to the experimental elution peak (circles). Dashed line represents the calculated elution peak from ED model.

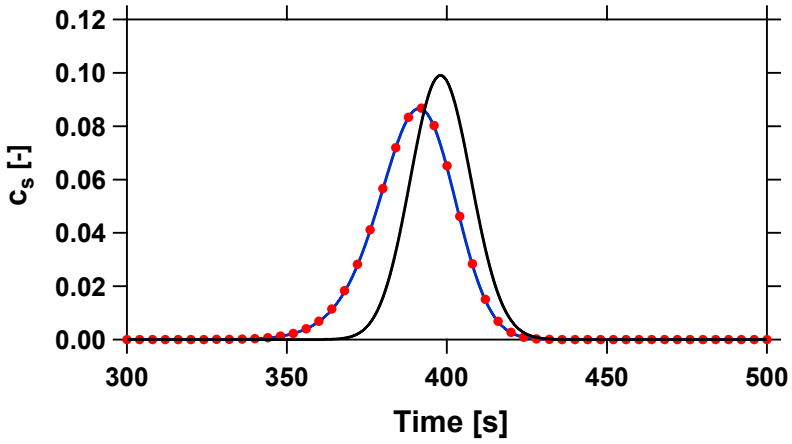

Figure 5.13: Solute (R-Flurbiprofen) elution peak for a small-volume injection (50μL). Case 1: With both viscous fingering and equilibrium effects (blue line). Case 2: With equilibrium effect and no viscous fingering (circles). Case 3: With no viscous fingering and no equilibrium effect (black line).

till the band disengages itself from methanol band, because of difference in retentions between solute and methanol. On the other hand, viscous fingering phenomenon affects only methanol band as it traverses along the column. A Case 3 is simulated where a pulse injection of solute R-Flurbiprofen is made in the mobile phase, instead of methanol plug. This case is similar to a modifier-stream injection where solute propagates in a single-phase environment with no viscosity contrasts and no equilibrium effects in the column. The elution peak for this case is shown in Fig. 5.13 as black line. It can be seen that the elution peaks from Cases 1 & 2 are more dispersed when to compared to Case 3. The reason for peak broadening in Cases 1 & 2 is primarily due to equilibrium effect, as the solute is injected in a mixed-stream mobile phase. This is consistent with observations reported recently [69].

5.4 Conclusions

A comprehensive axi-symmetric CFD model for a solute propagation in the supercritical fluid chromatographic (SFC) columns has been developed using commercial CFD solver ANSYS Fluent 16.2, where special source terms have been implemented using a user-defined functions. The model was able predict the dynamics of a solute in the supercritical fluid chromatographic (SFC) columns. Influence of viscous fingering and equilibrium effects on a pulse injection was studied. Experiments from the reports were compared to the simulation results. Key observations that could not be captured by classical Equilibrium-Dispersive models such as delay in elution times due to inlet pressure increase; peak fronting and peak distortions were predicted by the CFD model. The speculations of viscous fingering being the primary cause of peak distortions in large-volume injections, that were put forward in the previous publication was confirmed through the model. Modeling results provided a good description of experimental results. On one hand, while viscous fingering was the chief cause of peak distortions in large-volume injections, the effect of solvent strength on retention, commonly termed as the "plug-effect" was shown to be the primary reason for band broadening in small-volume (analytical scale) injections.

Chapter 6

Concluding remarks

6.1 Conclusions

This thesis dealt with the modeling and optimizations for adsorption and chromatographic based separation processes. In first part of the thesis, a rigorous process optimization was performed for four different PSA cycle configurations in order to evaluate their potential for pre-combustion CO_2 capture using TDA AMS-19. The second part of the thesis verified the hypothesis of viscous fingering for a mixed-stream injections in supercritical fluid chromatographic columns using an axi-symmetric CFD model.

In Chapter 3, a detailed PSA model and an optimization framework was introduced. Modeling the adsorption equilibria using the Sips isotherm model and also the estimation of competition of component species in a gaseous mixture was discussed. A one-dimensional model with mass, momentum and energy balances to describe the dynamics of an adsorption process was presented. A finite volume methodology using van Leer scheme was employed for spatial discretization and resulting ordinary differential equations in time were solved using an in-built ODE solver in MATLAB. A basic 4-step PSA cycle with adsorption, blowdown and pressurization steps was used to validate the model by satisfying the mass balance closure. The model was found to be accurate and computationally efficient requiring only 30 control volumes in order to accurately capture the dynamics of each state variable in a PSA process. A multi-objective optimization framework based on genetic algorithm was introduced, which was later coupled with the PSA model using genetic algorithm toolbox in MATLAB to obtain the results discussed in the subsequent chapter. The advantages and disadvantages of genetic algorithm along with the methodology were also presented.

Chapter 4 focused on evaluating different PSA cycle configurations using a multi-objective optimization. The adsorption equilibria for CO_2 on TDA AMS-19 was modeled using a Sips isotherm model based on the experiments performed by TDA Research Inc. and H_2 isotherm data on activated carbon was obtained from literature. An unconstrained multi-objective optimization was performed to maximize the CO_2 purity and recovery for four PSA cycles. The basic 4-step

PSA cycle was found to be infeasible while the configuration B with counter-current blowdown, pressure equalization, purge and light product pressurization was able to achieve the desired CO_2 recoveries but the CO_2 purities were limited to 92%. Configurations C and D were able to achieve CO_2 purities and recoveries greater than 95% and 90% respectively. A detailed parasitic energy model for PSA process was developed taking into account CO_2 compression, steam consumption and heat recovery units. A multi-staged compression with intercoolers was considered to estimate the electrical power consumption for CO_2 compression. The steam consumed in the PSA process was quantified in terms of an equivalent electricity that can be generated. The CO_2 compression energies were compared against two different cases to validate the methodology and a parametric study was performed to learn the effect of low pressure on the power consumption in the PSA process. Furthermore, a constrained multi-objective optimization problem was considered to minimize the total power consumption and maximize the productivity of the PSA process. For this, an 8-step PSA cycle configuration was optimized as it satisfied the CO_2 purity-recovery requirements.

In chapter 5, a comprehensive axi-symmetric CFD model is developed to verify the hypothesis of viscous fingering influencing the peak distortions in supercritical fluid chromatography. A commercial CFD solver ANSYS Fluent 16.2 was employed for solving mass, momentum and transport equations simultaneously. Special source terms have been implemented using a user-defined functions. The model confirmed the existence of viscous fingering which contributed to the chromatographic band distortions in SFC. The CFD model was also able to capture other phenomenon such as delay in elution times and peak distortions that could not be predicted by classical Equilibrium-Dispersive model. The simulated elution peaks showed a good comparison with the experimental results. It was also shown that the propagation of solute in small-volume injections is more influenced by plug-effect rather than viscous fingering.

6.2 Outlook

The first part of this work has provided a path towards designing and evaluating different pressure swing adsorption processes for pre-combustion CO_2 capture through modeling and optimization techniques. By coupling a rigorous multi-objective routine with the one-dimensional PSA model, it is now possible to determine the optimal operating conditions that could maximize the purity, recovery, productivity and minimize the energy consumption of a PSA process. Although, it was shown that some of the PSA cycle configurations have the potential to reach the requirements for sequestration, there are several aspects that requires further investigation.

A proper description of adsorption equilibria of H_2 and H_2O on TDA AMS-19 is necessary. A possible study on experimental measurements of multi-component adsorption equilibria would verify the accuracy of extended Sips isotherm model. While the energy model discussed in this

work provides the information on the power consumption for a PSA process, future studies should focus on integrating the steam consumption and heat recoveries into an IGCC power plant. Even though, the energy and productivity optimization provides a preliminary estimation of operating costs for the PSA process, considering a detailed economic analysis could be the possible extension of this work in order to understand the complete process performance. Finally, developing new and improving the existing PSA cycle configurations would also explore the potential of adsorptive pre-combustion CO_2 capture.

In the second part, development of a comprehensive axi-symmetric CFD model provided a proper description of propagation of solute bands along the chromatographic columns. The CFD model captured interesting phenomena such as viscous fingering, delay in elution times and peak distortions that were not predicted by classical Equilibrium-Dispersive model. Modeling the system in three dimensions was challenging due to the limited computational resources, but it is worth considering for a better understanding of asymmetric nature of viscous fingering phenomenon. The possible extension of this work would be the implementation of fluid compressibility into the model.

Bibliography

[1] International Energy Agency, *Energy and Climate Change*, 2015.

[2] International Energy Agency, *CO_2 Capture and Storage*, 2008.

[3] Working Group III of the Intergovernmental Panel on Climate Change, *IPCC Special Report on Carbon dioxide Capture and Storage.* Cambridge Press, 2005.

[4] Global CCS Institute, *The Global Status of CCS: 2016 Summary Report*, 2016.

[5] E. Dlugokencky and P. Tans, *Monthly CO_2 measurements from 1959 to 2017.* NOAA/ESRL, 2017.

[6] NASA's Goddard Institute for Space Studies (GISS), *Global Land-Ocean Temperature Index*, 2017.

[7] M. M. Hossain and H. I. de Lasa, "Chemical-looping combustion (CLC) for inherent CO_2 separations-a review," *Chemical Engineering Science*, vol. 63, no. 18, pp. 4433 – 4451, 2008.

[8] A. A. Olajire, "CO_2 capture and separation technologies for end-of-pipe applications A review," *Energy*, vol. 35, no. 6, pp. 2610 – 2628, 2010.

[9] C. Gouedard, D. Picq, F. Launay, and P.-L. Carrette, "Amine degradation in CO_2 capture. I. A review," *International Journal of Greenhouse Gas Control*, vol. 10, pp. 244 – 270, 2012.

[10] M. Wang, A. Lawal, P. Stephenson, J. Sidders, and C. Ramshaw, "Post-combustion CO_2 capture with chemical absorption: A state-of-the-art review," *Chemical Engineering Research and Design*, vol. 89, no. 9, pp. 1609 – 1624, 2011.

[11] A. B. Rao and E. S. Rubin, "A Technical, Economic, and Environmental Assessment of Amine-Based CO_2 Capture Technology for Power Plant Greenhouse Gas Control," *Environmental Science & Technology*, vol. 36, no. 20, pp. 4467–4475, 2002.

[12] H. W. Pennline, D. R. Luebke, K. L. Jones, C. R. Myers, B. I. Morsi, Y. J. Heintz, and J. B. Ilconich, "Progress in carbon dioxide capture and separation research for gasification-based power generation point sources," *Fuel Processing Technology*, vol. 89, no. 9, pp. 897 – 907, 2008.

[13] J. D. Figueroa, T. Fout, S. Plasynski, H. McIlvried, and R. D. Srivastava, "Advances in CO_2 capture technology-the U.S. Department of Energy's Carbon Sequestration Program," *International Journal of Greenhouse Gas Control*, vol. 2, no. 1, pp. 9 – 20, 2008.

[14] D. M. Ruthven, *Principles of Adsorption and Adsorption Processes.* New York: Wiley-Interscience, 1984.

[15] K. S. K. Douglas M. Ruthven, Shamsuzzaman Farooq, *Pressure Swing Adsorption.* Wiley, 1994.

[16] P. Bernardo, E. Drioli, and G. Golemme, "Membrane Gas Separation: A Review/State of the Art," *Industrial & Engineering Chemistry Research*, vol. 48, no. 10, pp. 4638–4663, 2009.

[17] Laboratory for energy and the environment, MIT, *An Overview of Coal based Integrated Gasification Combined Cycle (IGCC) Technology*, 2005.

[18] A. Samanta, A. Zhao, G. K. H. Shimizu, P. Sarkar, and R. Gupta, "Post-Combustion CO_2 Capture Using Solid Sorbents: A Review," *Industrial & Engineering Chemistry Research*, vol. 51, no. 4, pp. 1438–1463, 2012.

[19] Z. Yong, V. Mata, and A. E. Rodrigues, "Adsorption of carbon dioxide at high temperature - a review," *Separation and Purification Technology*, vol. 26, no. 2, pp. 195 – 205, 2002.

[20] A. Sayari, Y. Belmabkhout, and R. Serna-Guerrero, "Flue gas treatment via CO_2 adsorption," *Chemical Engineering Journal*, vol. 171, no. 3, pp. 760 – 774, 2011.

[21] D. D'Alessandro, B. Smit, and J. Long, "Carbon Dioxide Capture: Prospects for New Materials," *Angewandte Chemie International Edition*, vol. 49, no. 35, pp. 6058–6082, 2010.

[22] J. Zhang, R. Singh, and P. A. Webley, "Alkali and alkaline-earth cation exchanged chabazite zeolites for adsorption based CO_2 capture," *Microporous and Mesoporous Materials*, vol. 111, no. 1, pp. 478 – 487, 2008.

[23] T. Inui, Y. Okugawa, and M. Yasuda, "Relationship between properties of various zeolites and their carbon dioxide adsorption behaviors in pressure swing adsorption operation," *Industrial & Engineering Chemistry Research*, vol. 27, no. 7, pp. 1103–1109, 1988.

[24] S.-Y. Lee and S.-J. Park, "A review on solid adsorbents for carbon dioxide capture," *Journal of Industrial and Engineering Chemistry*, vol. 23, pp. 1 – 11, 2015.

[25] P. J. E. Harlick and A. Sayari, "Applications of Pore-Expanded Mesoporous Silicas. 3. Triamine Silane Grafting for Enhanced CO_2 Adsorption," *Industrial & Engineering Chemistry Research*, vol. 45, no. 9, pp. 3248–3255, 2006.

[26] H. Furukawa, N. Ko, Y. B. Go, N. Aratani, S. B. Choi, E. Choi, A. Ö. Yazaydin, R. Q. Snurr, M. O'Keeffe, J. Kim, and O. M. Yaghi, "Ultrahigh Porosity in Metal-Organic Frameworks," *Science*, vol. 329, no. 5990, pp. 424–428, 2010.

[27] B.-K. Na, K.-K. Koo, H.-M. Eum, H. Lee, and H. K. Song, "CO_2 recovery from flue gas by PSA process using activated carbon," *Korean Journal of Chemical Engineering*, vol. 18, no. 2, pp. 220–227, 2001.

[28] D. D. Do, *Adsorption analysis: equilibria and kinetics*, vol. 2 of *Chemical Engineering Series*. London: Imperial College Press, 1998.

[29] I. Langmuir, "The adsorption of gases on plane surfaces of glass, mica and platinum.," *Journal of the American Chemical Society*, vol. 40, no. 9, pp. 1361–1403, 1918.

[30] R. Sips, "On the Structure of a Catalyst Surface," *The Journal of Chemical Physics*, vol. 16, no. 5, pp. 490–495, 1948.

[31] A. L. Myers and J. M. Prausnitz, "Thermodynamics of mixed-gas adsorption," *AIChE Journal*, vol. 11, no. 1, pp. 121–127, 1965.

[32] J. Chen, L. S. Loo, and K. Wang, "An Ideal Absorbed Solution Theory (IAST) Study of Adsorption Equilibria of Binary Mixtures of Methane and Ethane on a Templated Carbon," *Journal of Chemical & Engineering Data*, vol. 56, no. 4, pp. 1209–1212, 2011.

[33] A. Tarafder and M. Mazzotti, "A Method for Deriving Explicit Binary Isotherms Obeying the Ideal Adsorbed Solution Theory," *Chemical Engineering & Technology*, vol. 35, no. 1, pp. 102–108, 2012.

[34] A. K. Rajagopalan, "Material selection and process design for adsorptive CO_2 capture," Master's thesis, University of Alberta, 2015.

[35] J. Carter and M. Wyszynski, "The pressure swing adsorption drying of compressed air," *Chemical Engineering Science*, vol. 38, no. 7, pp. 1093 – 1099, 1983.

[36] N. S. Raghavan and D. M. Ruthven, "Numerical simulation of a fixed-bed adsorption column by the method of orthogonal collocation," *AIChE Journal*, vol. 29, no. 6, pp. 922–925, 1983.

[37] E. S. Kikkinides and R. T. Yang, "Effects of bed pressure drop on isothermal and adiabatic adsorber dynamics," *Chemical Engineering Science*, vol. 48, no. 9, pp. 1545 – 1555, 1993.

[38] P. A. Webley and J. He, "Fast solution-adaptive finite volume method for PSA/VSA cycle simulation; 1 single step simulation," *Computers & Chemical Engineering*, vol. 23, no. 11, pp. 1701 – 1712, 2000.

[39] R. S. Todd, J. He, P. A. Webley, C. Beh, S. Wilson, and M. A. Lloyd, "Fast Finite-Volume method for PSA/VSA Cycle Simulation-Experimental Validation," *Industrial & Engineering Chemistry Research*, vol. 40, no. 14, pp. 3217–3224, 2001.

[40] P. Cruz, J. Santos, F. Magalhes, and A. Mendes, "Simulation of separation processes using finite volume method," *Computers & Chemical Engineering*, vol. 30, no. 1, pp. 83 – 98, 2005.

[41] S. Krishnamurthy, V. R. Rao, S. Guntuka, P. Sharratt, R. Haghpanah, A. Rajendran, M. Amanullah, I. A. Karimi, and S. Farooq, "CO_2 capture from dry flue gas by vacuum swing adsorption: A pilot plant study," *AIChE Journal*, vol. 60, no. 5, pp. 1830–1842, 2014.

[42] R. Haghpanah, A. Majumder, R. Nilam, A. Rajendran, S. Farooq, I. A. Karimi, and M. Amanullah, "Multiobjective Optimization of a Four-Step Adsorption Process for Post-combustion CO_2 Capture Via Finite Volume Simulation," *Industrial & Engineering Chemistry Research*, vol. 52, no. 11, pp. 4249–4265, 2013.

[43] S. V. Patankar, *Numerical heat transfer and fluid flow*. Computational methods in mechanics and thermal sciences, McGraw Hill, 1980.

[44] R. J. LeVeque, *Finite Volume Methods for Hyperbolic Problems*. Cambridge University Press, 2002.

[45] M. K. Verma, *Fundamentals of Carbon Dioxide-Enhanced Oil Recovery (CO_2-EOR)- A Supporting Document of the Assessment Methodology for Hydrocarbon Recovery Using CO_2-EOR Associated with Carbon Sequestration*. U.S. Department of the Interior and U.S. Geological Survey, 2015.

[46] K. Deb, A. Pratap, S. Agarwal, and T. Meyarivan, "A fast and elitist multiobjective genetic algorithm: NSGA-2," *IEEE Transactions on Evolutionary Computation*, vol. 6, no. 2, pp. 182–197, 2002.

[47] N. Casas, J. Schell, R. Pini, and M. Mazzotti, "Fixed bed adsorption of CO_2/H_2 mixtures on activated carbon: experiments and modeling," *Adsorption*, vol. 18, no. 2, pp. 143–161, 2012.

[48] G. D. Ulrich and P. T. Vasudevan, *Chemical Engineering Process Design and Economics: A Practical Guide*. Durham, New Hampshire: Process Publishing, 2004.

[49] European Commission, *European best practice guidelines for assessment of CO_2 capture technologies*, 2010.

[50] S. F. Chien, "Empirical Correlations of Saturated Steam Properties," *Society of Petroleum Engineers*, vol. 7, 1992.

[51] M. Affandi, N. Mamat, S. N. A. M. Kanafiah, and N. S. Khalid, "Simplified Equations for Saturated Steam Properties for Simulation Purpose," *Procedia Engineering*, vol. 53, pp. 722 – 726, 2013.

[52] K. E. Nelson, *A Practical Guide to Energy Accounting*. Chemical Engineering, 1994.

[53] NIST Refprop v9.1 database.

[54] National Energy Technology Laboratory, *Cost and Performance Baseline for Fossil Energy Plants*, 2007.

[55] L. Riboldi and O. Bolland, "Evaluating Pressure Swing Adsorption as a CO_2 separation technique in coal-fired power plants," *International Journal of Greenhouse Gas Control*, vol. 39, pp. 1 – 16, 2015.

[56] E. R. Francotte, "Enantioselective chromatography as a powerful alternative for the preparation of drug enantiomers," *Journal of Chromatography A*, vol. 906, no. 12, pp. 379 – 397, 2001.

[57] L. Miller, "Preparative enantioseparations using supercritical fluid chromatography," *Journal of Chromatography A*, vol. 1250, pp. 250 – 255, 2012.

[58] A. Rajendran, "Recent developments in preparative chromatographic processes," *Current Opinion in Chemical Engineering*, vol. 2, no. 2, pp. 263 – 270, 2013.

[59] C. Welch, W. Leonard Jr., J. DaSilva, M. Biba, J. Albaneze-Walker, D. Henderson, B. Laing, D. Mathre, and R. Majors, "Preparative chiral SFC as a green technology for rapid access to enantiopurity in pharmaceutical process research," *LC-GC North America*, vol. 23, no. 1, pp. 16–29, 2005.

[60] C. R. Yonker and R. D. Smith, "Sorption isotherms of mobile phase components in capillary supercritical fluid chromatography," *Journal of Chromatography A*, vol. 505, no. 1, pp. 139 – 146, 1990.

[61] P. Vajda and G. Guiochon, "Surface excess isotherms of organic solvent mixtures in a system made of liquid carbon dioxide and a silicagel surface," *Journal of Chromatography A*, vol. 1308, pp. 139 – 143, 2013.

[62] C. Wenda, R. Haghpanah, A. Rajendran, and M. Amanullah, "Optimization of isocratic supercritical fluid chromatography for enantiomer separation," *Journal of Chromatography A*, vol. 1218, no. 1, pp. 162 – 170, 2011.

[63] T. Berger and K. Fogelman, "Method of sample introduction for supercritical fluid chromatography systems," 2002.

[64] G. Cox, "Extraction-injection: an alternative sample introduction method for SFC," SPICA, 2014.

[65] Y. Dai, G. Li, and A. Rajendran, "Peak distortions arising from large-volume injections in supercritical fluid chromatography," *Journal of Chromatography A*, vol. 1392, pp. 91 – 99, 2015.

[66] A. Rajendran, "Design of preparative-supercritical fluid chromatography," *Journal of Chromatography A*, vol. 1250, pp. 227 – 249, 2012.

[67] F. Gritti, "Unexpected retention and efficiency behaviors in supercritical fluid chromatography: A thermodynamic interpretation," *Journal of Chromatography A*, vol. 1468, pp. 209 – 216, 2016.

[68] R. A. Shalliker, H. J. Catchpoole, G. R. Dennis, and G. Guiochon, "Visualising viscous fingering in chromatography columns: High viscosity solute plug," *Journal of Chromatography A*, vol. 1142, no. 1, pp. 48 – 55, 2007.

[69] M. Enmark, D. Åsberg, A. Shalliker, J. Samuelsson, and T. Fornstedt, "A closer study of peak distortions in supercritical fluid chromatography as generated by the injection," *Journal of Chromatography A*, vol. 1400, pp. 131 – 139, 2015.

[70] L. D. Plante, P. M. Romano, and E. J. Fernandez, "Viscous fingering in chromatography visualized via magnetic resonance imaging," *Chemical Engineering Science*, vol. 49, no. 14, pp. 2229 – 2241, 1994.

[71] C. Rana, A. De Wit, M. Martin, and M. Mishra, "Combined influences of viscous fingering and solvent effect on the distribution of adsorbed solutes in porous media," *RSC Adv.*, vol. 4, pp. 34369–34381, 2014.

[72] G. M. Homsy, "Viscous Fingering in Porous Media," *Annual Review of Fluid Mechanics*, vol. 19, no. 1, pp. 271–311, 1987.

[73] T. T. Norton and E. J. Fernandez, "Viscous Fingering in Size Exclusion Chromatography: Insights from Numerical Simulation," *Industrial & Engineering Chemistry Research*, vol. 35, no. 7, pp. 2460–2468, 1996.

[74] H. J. Catchpoole, R. A. Shalliker, G. R. Dennis, and G. Guiochon, "Visualising the onset of viscous fingering in chromatography columns," *Journal of Chromatography A*, vol. 1117, no. 2, pp. 137 – 145, 2006.

[75] G. Guiochon, A. Felinger, and D. Shirazi, *Fundamentals of Preparative and Nonlinear Chromatography*. Elsevier Science, 2006.

[76] *ANSYS Fluent Theory Guide, Release 16.2*. ANSYS Inc., 2015.

[77] C. Wenda and A. Rajendran, "Enantioseparation of flurbiprofen on amylose-derived chiral stationary phase by supercritical fluid chromatography," *Journal of Chromatography A*, vol. 1216, no. 50, pp. 8750 – 8758, 2009.

[78] *ANSYS Fluent User Guide, Release 16.2*. ANSYS Inc., 2015.

[79] D. A. Nield and A. Bejan, *Convection in Porous Media*. New York: Springer, third ed., 2006.

[80] A. Rajendran, M. Mazzotti, and M. Morbidelli, "Enantioseparation of 1-phenyl-1-propanol on chiralcel OD by supercritical fluid chromatography: I. Linear isotherm," *Journal of Chromatography A*, vol. 1076, no. 12, pp. 183 – 188, 2005.

Appendix A

Effect of solvent dispersion constant D

Viscous fingering is a transient phenomenon where dispersion and mixing influence the propagation of fingers along the column [71]. Hence, the choice of dispersion constant and grid size is critical while modeling fingers. A parametric study is performed to see the effect of dispersion constant on viscous fingering. For this, simulations are run for 4 different dispersion constants, (a) $D = 3 \times 10^{-9}$ m^2 s^{-1} (b) $D = 4 \times 10^{-9}$ m^2 s^{-1} and (c) $D = 4.5 \times 10^{-9}$ m^2 s^{-1} (d) $D = 5 \times 10^{-9}$ m^2 s^{-1}. A large volume of 2 mL pulse injection of methanol is considered. Fig. A.1 shows the propagation of methanol plug at different times for all cases. It can be seen that the fingering phenomena originates at same time for all cases. However, for case with $D = 3 \times 10^{-9}$ m^2 s^{-1} at time t=300 s, the plug distortion is different from other cases. As the dispersion constant is reduced, it is expected that the model captures propagation of more fingers along the column. However, since the grid size is kept constant, decreasing the dispersion reduces the resolution of the grid to capture fingers, leading to mixing. Fingers propagation for such cases can be shown by increasing the resolution of the grid. For other cases, it can be seen that the length of distorted region decreases with increase in dispersion constant, due to mixing of fingers. While modeling viscous fingering, therefore it is important to choose correct combination of grid size and dispersion constant. Fig. A.2 shows the elution profiles of methanol for all cases under this parametric study. An averaged value of $D = 4.5 \times 10^{-9}$ m^2 s^{-1} is chosen as the dispersion constant for the solvent.

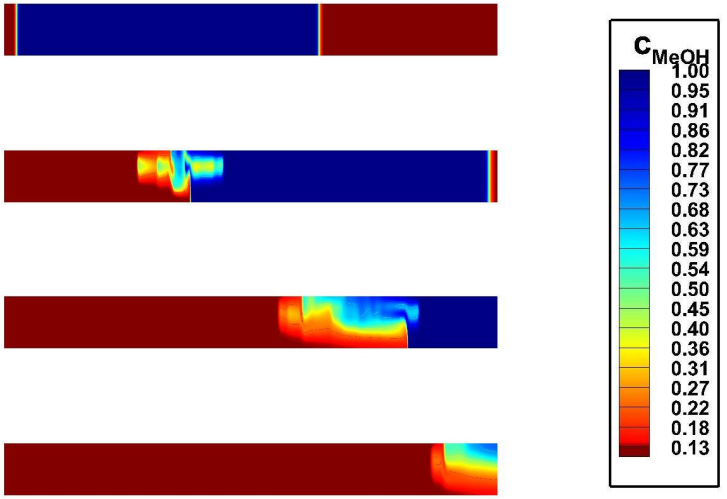

(a) D = 3×10^{-9} m^2 s^{-1}

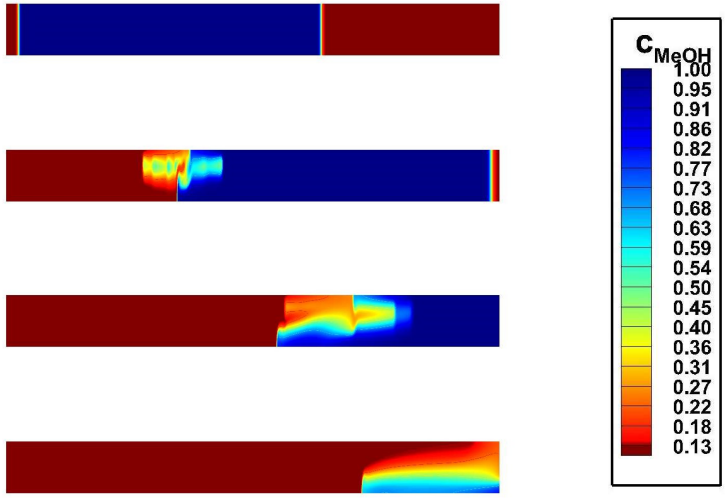

(b) D = 4×10^{-9} m^2 s^{-1}

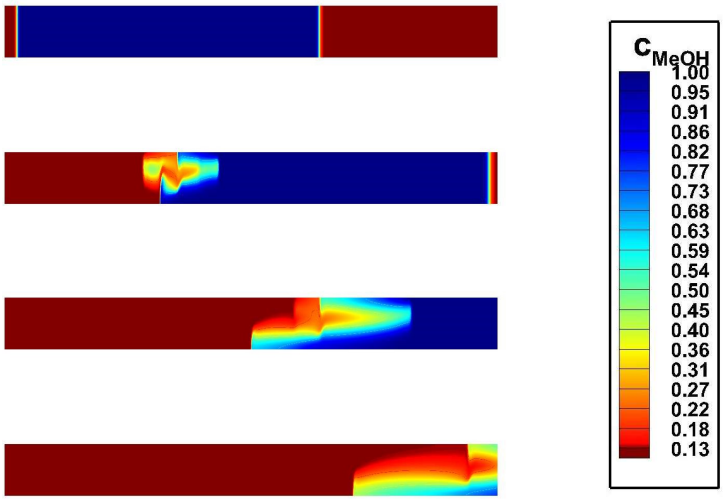

(c) D = 4.5×10^{-9} m^2 s^{-1}

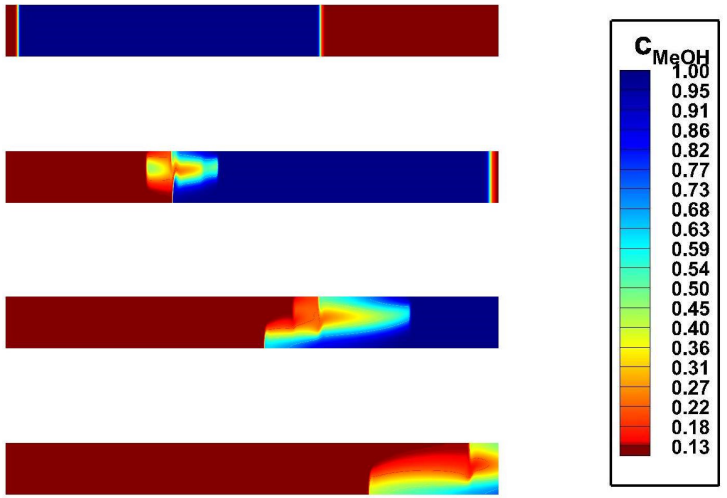

(d) D = 5×10^{-9} m^2 s^{-1}

Figure A.1: Evolution of local methanol concentration $c_i(x, y, t)$ at time t= 200, 250, 300 and 350 seconds for cases (a) D=3×10^{-9} m^2 s^{-1} (b) D=4×10^{-9} m^2 s^{-1} (c) D=4.5×10^{-9} m^2 s^{-1} (d) D=5×10^{-9} m^2 s^{-1}. The propagation is from left to right.

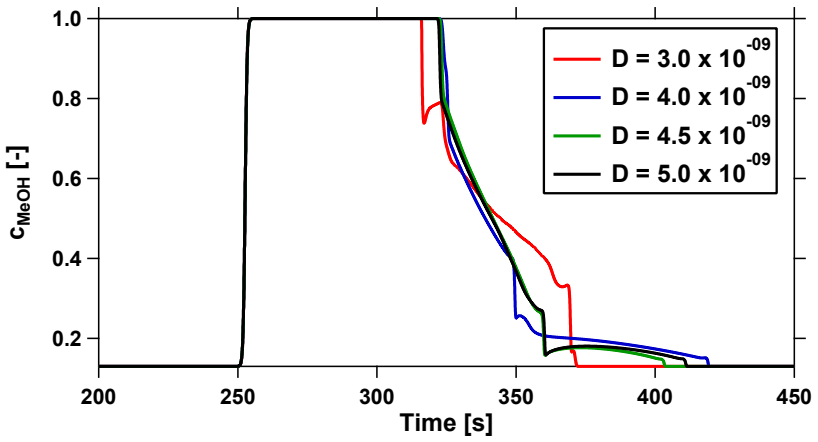

Figure A.2: Elution peaks of methanol for different dispersion constants [in $m^2\ s^{-1}$].